Dileptons as probes of strongly interacting matter

Dileptonen als Sonden für stark-wechselwirkende Materie
Masterarbeit von Maximilian Justus Wiest
Tag der Einreichung: 18. September 2020

1. Gutachten: Prof. Dr. Tetyana Galatyuk
(TU Darmstadt)
2. Gutachten: Prof. Dr. Joachim Stroth
(Goethe-Universität Frankfurt)
Darmstadt

TECHNISCHE
UNIVERSITÄT
DARMSTADT

Fachbereich Physik
Institut für Kernphysik
Arbeitsgruppe Galatyuk

Erklärung zur Abschlussarbeit gemäß §22 Abs. 7 und §23 Abs. 7 APB der TU Darmstadt

Hiermit versichere ich, Maximilian Justus Wiest, die vorliegende Masterarbeit ohne Hilfe Dritter und nur mit den angegebenen Quellen und Hilfsmitteln angefertigt zu haben. Alle Stellen, die Quellen entnommen wurden, sind als solche kenntlich gemacht worden. Diese Arbeit hat in gleicher oder ähnlicher Form noch keiner Prüfungsbehörde vorgelegen.

Mir ist bekannt, dass im Fall eines Plagiats (§38 Abs. 2 APB) ein Täuschungsversuch vorliegt, der dazu führt, dass die Arbeit mit 5,0 bewertet und damit ein Prüfungsversuch verbraucht wird. Abschlussarbeiten dürfen nur einmal wiederholt werden.

Bei der abgegebenen Thesis stimmen die schriftliche und die zur Archivierung eingereichte elektronische Fassung gemäß §23 Abs. 7 APB überein.

Bei einer Thesis des Fachbereichs Architektur entspricht die eingereichte elektronische Fassung dem vorgestellten Modell und den vorgelegten Plänen.

Darmstadt, 18. September 2020

M. Wiest

Abstract

In the early universe, only microseconds after the Big Bang, matter was found at extreme conditions. These conditions still exist in compact stellar objects. In the laboratory, these types of conditions are only accessible through heavy-ion collisions. The understanding of properties of matter at extreme conditions makes use of various observables - particle production, their flow and event-by-event correlations. Electromagnetic probes are special. Since hadrons produced in heavy-ion collisions are subject to the strongly interacting medium after their creation, they are only partially able to act as messengers for information about the conditions during their creation. Rare probes which have a bigger chance to escape the fireball undisturbed provide valuable insights on the medium and the spectral functions of hadrons in the medium. Among them are dileptons in the form of e^+e^-- and $\mu^+\mu^-$-pairs.

In this thesis, the coarse graining approach is used to compare four state-of-the-art microscopic transport models (UrQMD, SMASH, GiBUU and PHSD) regarding their produced baryon densities, temperature and dilepton yield. The possibility of an observation of medium effects, which are generally not included in the transport models would then require these effects to be larger than the effects induced by different transport models. Au+Au collisions at $1.23A$ GeV are used as a test case as experimental data obtained by the HADES collaboration exists in this case. In a second step, four different collision systems, two of them measured recently by the HADES collaboration, will be investigated to achieve insights on the dependence of the dilepton yield on the system size, collision centrality and energy. This is the first step to gain information about the excitation function of matter goverend by the strong interaction.

Chapter 1 will give a short historical overview over the field of heavy-ion and elementary particle physics. Chapter 2 discusses the physical background of the strong interaction, chiral symmetry and dileptons as probes of heavy-ion collisions. Chapter 3 will provide the absolute basics of transport theory and quickly introduce the models used in this thesis. Chapter 4 introduces the coarse graining approach, while Chapter 5 presents the results and insights obtained in this thesis. Chapter 6 summarizes the findings. Additional information is given in the Appendix.

Zusammenfassung

Im frühen Universum, nur Mikrosekunden nach dem Urknall, lag Materie unter extremen Bedingungen vor. Diese Bedingungen existieren noch heute in kompakten Sternen. Im Labor sind sie jedoch nur durch Schwerionenkollisionen zu untersuchen. Diese Untersuchungen bedienen sich verschiedenster Observablen, wie Teilchenproduktion, Teilchenfluss und Event-zu-Event-Korrelationen. Elektromagnetische Sonden sind besonders aufschlussreich. Da Hadronen, die in Schwerionen-Kollisionen produziert werden, nach ihrer Entstehung dem stark wechselwirkenden Medium ausgeliefert sind, sind sie nur teilweise in der Lage, als Informationsträger über das Medium zur Zeit ihrer Entstehung zu fungieren. Seltene Sonden, die eine größere Chance haben, das Medium ungestört zu verlassen, liefern wertvolle Einsichten über das Medium und die hadronischen Spektralfunktionen innerhalb des Mediums. Unter den seltenen Proben finden sich auch Dileptonen in Form von e^+e^-- und $\mu^+\mu^-$-Paaren.

In dieser Arbeit wird ein Grobkörnungsansatz benutzt, um vier dem Stand der Technik entsprechende mikroskopische Transportmodelle (UrQMD, SMASH, GiBUU und PHSD) bezüglich ihrer berechneten Baryonendichten, Temperaturen und Dileptonenraten zu vergleichen. Die Möglichkeit einer experimentellen Beobachtung von Mediumeffekten, die im Allgemeinen nicht in den Modellen enthalten sind, setzt voraus, dass diese Effekte größer sind als die Differenzen der einzelnen Transportmodelle. Au+Au-Kollisionen bei $1.23A$ GeV werden als Testfall für den Vergleich genutzt, da hier experimentelle Daten der HADES-Gruppe vorliegen. In einem zweiten Schritt werden vier Kollisionssysteme, zwei davon kürzlich von der HADES-Gruppe experimentell erforscht, untersucht, um Ergebnisse über die Abhängigkeiten der Dileptonobservablen von der Größe der Systeme, der Kollisionszentralität und der Energie zu erhalten. Dies ist ein erster Schritt, um Informationen über die Anregungsfunktionen von Materie zu erhalten, die der starken Wechselwirkung unterliegt.

Kapitel 1 wird einen kurzen historischen Überblick über das Feld der Schwerionen- und Elementarteilchenphysik präsentieren. In Kapitel 2 werden der physikalische Hintergrund der starken Wechselwirkung, ihrer chiralen Symmetrie und der Nutzung von Dileptonen als Sonden in Schwerionenkollisionen diskutiert. Kapitel 3 enthält eine kurze Einführung in die Transporttheorie und die in dieser Arbeit benutzten Modelle. Kapitel 4 stellt den Grobkörnungsansatz vor, während Kapitel 5 die in dieser Arbeit gewonnenen Resultate und Einsichten präsentiert. Kapitel 6 fasst die Ergebnisse zusammen. Zusätzliche Informationen finden sich im Anhang.

Contents

1 Introduction

Over the last two hundred years, the search for the primordial building blocks of matter has driven the research of many great chemists and physicists. The idea of the existence of such smallest building blocks can be traced back even further to ancient Greece, when Democritus of Abdera postulated that matter cannot be divided into arbitrarily small chunks, but instead consists of indivisible blocks he called by what they were: $\alpha\tau o\mu o\zeta$, or atoms. And while he was a great thinker, Democritus could never have imagined the feats that followed, journeying deeper and deeper into the microcosm to unravel increasingly smaller building blocks. Indeed, the pace of discoveries in the twentieth century is nothing but stunning.
Einstein used Brownian motion to prove the concept of atoms [1], which was already strongly implied by Dalton's observation that chemical reactions were taking place only for certain ratios of the reactants. While Thomson thought of the atom as a sphere with a homogeneous positive charge dotted with electrons [2], which were already known at the time due to experiments done by Thomson himself among others [3], Rutherford showed that atoms are mostly empty space in his legendary scattering experiment, with a heavy nucleus of concentrated positive charge and mass and a thin outer layer of electrons [4]. This posed the question of how the large number of protons concentrated in the nucleus were resisting the immense repulsive Coulomb force between them. Rutherford himself predicted the existence of the neutron which was first thought of as a tightly bound electromagnetic state like a collapsed hydrogen atom [5]. Instead, the neutron was observed to be a distinct particle by Chadwick in 1932 [6], which was attracted to the proton on nuclear scales via a force carrying particle postulated by Yukawa in 1936 [7]. However, soon after the discovery of Yukawa particles named pions ($\pi^{(+,0,-)}$) in 1947, a whole zoo of strange and exotic particles emerged and ultimately led to the formulation of the quark-hypothesis as proposed independently by Gell-Mann and Zweig in 1964 [8, 9]. The quark model has been extraordinarily successful in ordering the particle zoo. To this date, six flavours of quarks have been found, and observations at the Large Electron Positron Collider suggest that at least no further generations of matter with light neutrinos exist [10].
However, not only the nature of the elementary particles, but also their interactions and behaviour are of utmost importance to understand the world that we live in to the best possible degree. Of the fundamental interactions, gravity and electro-weak interaction are well described by General Relativity and the Glashow-Salam-Weinberg model, respectively [11]. Only the fundamental equations governing the strong interaction are known, giving rise to **q**uantum **c**hromo**d**ynamics (QCD). They are not solvable analytically, and numerical computations can only help in special cases. Another hurdle is that experiments in the laboratory can only access strongly interacting matter in heavy-ion collisions using large and expensive particle accelerators to create pure strongly interacting matter for tiny amounts of time. These hurdles make it difficult to study quark matter in the same way that everyday matter can be studied. The QCD-phase diagram for example has many unknown regions, where experimental data, in particular on rare probes, is missing completely and theoretical predictions are scarce due to the complex interactions. It is vital for a complete understanding of QCD to access these areas with experiments and better theoretical predictions.

2 Background

For the interpretation of any data or simulation, a detailed understanding of the underlying physical and computational mechanisms is mandatory. The following sections serve to explain the theoretical foundations of this work as well as their connection to the studies conducted for this work.

2.1 Standard Model

The Standard Model of particle physics is a quantum field theory. It combines the known fermionic constituents of matter, their antiparticles, the bosonic carriers of three of the four fundamental interactions as well as the Higgs boson giving the elementary particles their mass through the Higgs mechanism [12]. While the general theory of relativity so far has passed each and every test it has been subject to, gravity is not included in the Standard Model due to the lack of a quantum mechanical formulation. Every attempt at doing so has either resulted in an ultraviolet catastrophe or has, up until now, evaded testing apart from the sheer existence of gravity itself. However, gravity is very weak when compared against the weak, electromagnetic and the strong interactions and does not play a role in high energy physics (see Table 2.1).
As can be seen in Fig. 2.1, the fermions in the Standard Model split up into two groups, quarks and leptons. Each of these two groups consists of three generations, each generation contains two particles with electromagnetic charge differing by one elementary charge e. Leptons are not strongly interacting, but interact via the weak and the electromagnetic force. They carry an integer multiple of the elementary charge, with the electron, the muon and the tau-lepton carrying a charge of $-e$, their antiparticles a charge of $+e$ and the neutrinos carrying a charge of 0. Experimentally, the number of leptons is observed to be conserved. Neutrinos may be their own antiparticles (Majorana-fermions). Proof would for example be the occurrence of a neutrino-less double-beta-decay, but the half life for this has been estimated to be over 10^{26} years [15]. Lepton number conservation would be violated by this. In the Standard Model, the neutrino mass is taken as 0, however, the presence of neutrino oscillations mandates a non-vanishing neutrino mass, which could be explained by neutrinos being Majorana. Leptons, especially electrons, play an important role in the observation of strongly interacting matter, that will be discussed in Section 2.5.
Quarks carry multiples of $1/3\,e$ as their electromagnetic charge. In contrast to leptons, which can be observed as single particles in nature, a solitary quark has never been observed. All evidence for quarks is in a sense indirect, because they only appear in groups. This non-existence of free quarks is called confinement (see Section 2.5.2) and is related to an additional charge the quarks carry. In contrast to

Interaction	Strong	Electromagnetic	Weak	Gravity
Rel. strength	1	10^{-2}	10^{-15}	10^{-41}

Table 2.1: Relative strengths of the fundamental interactions as given in [13].

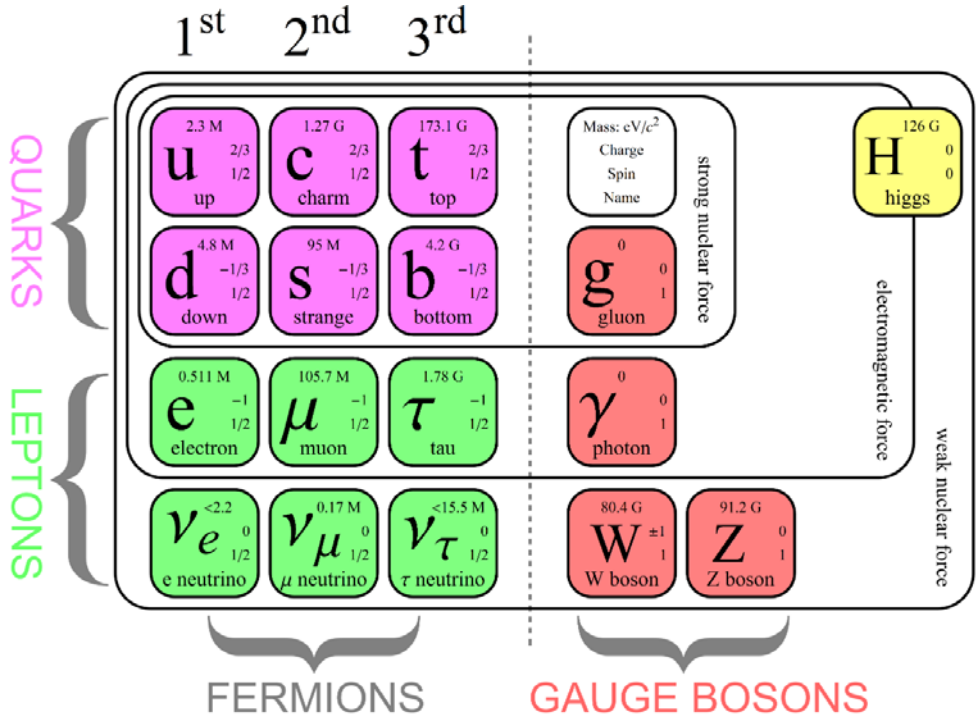

Figure 2.1: The particles of the Standard Model of particle physics. Quarks are shown in pink, leptons in green, the vector bosons in red and the Higgs particle in yellow color [14].

leptons, which only carry electroweak charges, the quarks additionally carry a so called color charge. After the invention of the quark model in 1964, the Δ^{++} baryon with a spin of 3/2, composed of three up quarks with parallel spin could only be explained by postulating an additional degree of freedom to prevent the state from violating the Pauli exclusion principle. The three degrees of freedom are called colors and are labelled red, blue and green. Antiquarks carry anticolors.
The bosons in the Standard Model are the mediators of forces. They consist of the photon as the carrier of the electromagnetic interaction, the gluons as the carriers of the strong interaction, the aforementioned Higgs boson and the W and Z bosons as carriers of the weak interaction. While Higgs , W and Z bosons are massive, photons and gluons are not. In contrast to the force carrying particles, which are all vector particles of spin 1, the Higgs boson is scalar.
Even though the Standard Model can explain many experimental results in detail, there are open questions and a search for physics beyond the Standard Model is ongoing. Examples for this are the non-vanishing mass of the neutrinos, which results in neutrino-oscillations as first observed at Super-KAMIOKANDE or the nature of dark matter, which has evaded detection to this date [16].

2.2 QCD and its properties

QCD is the theory of the strong interaction. It is a quantum field theory similar to Quantum Electrodynamics. However, the U(1)-symmetry on which QED is based, is abelian, while QCD's footing is the non-abelian SU(3)-symmetry [11]. Instead of one charge and its anticharge, QCD has three color charges, red, blue and green. The QCD force mediators, called gluons, each carry one of eight linear combinations of color and

anticolor. This means that the gluons can interact with each other, in contrast to the electrically neutral QED photons. The most general Lagrangian of QCD is given by

$$\mathcal{L}_{QCD} = \sum_{q=u,d,s,c,t,b} \overline{q}(i\gamma^{\mu}D_{\mu} - m_q)q - \frac{1}{4}G^a_{\mu\nu}G^{\mu\nu}_a, \tag{2.1}$$

where m_q is the respective mass of each quark, γ^{μ} are the Dirac-matrices and D_{μ} is the covariant derivative $\partial_{\mu} - igA^a_{\mu}$ [17]. q is a short-hand notation for a set of three Dirac-4-spinors resulting from the three colors each quark can carry. A^a_{μ} are the eight 4-vector potentials associated with the eight gluons. Analogously to the electromagnetic field strength tensor $F_{\mu\nu}$, the first part of the gluon field strength tensor $G^a_{\mu\nu}$ describes the propagation of massless gluons:

$$\begin{aligned} F_{\mu\nu} &= \partial_{\mu}A_{\nu} - \partial_{\nu}A_{\mu} \\ G^a_{\mu\nu} &= \partial_{\mu}A^a_{\nu} - \partial_{\nu}A^a_{\mu} + gf^{abc}A^b_{\mu}A^c_{\nu}. \end{aligned} \tag{2.2}$$

However, due to the non-abelian nature of the SU(3) group QCD is based on, the structure constants $f^{\{a,b,c\}}$ arise, while the constants are 0 for the abelian theory of electromagnetism. The second term in Eq. (2.2) therefore is the mathematical expression for the gluons' interaction with other gluons and them carrying color charge. In theory, this gives rise to particles made completely out of gluons, commonly called glueballs [18].

2.2.1 Running coupling constant

The QCD-coupling constant is denoted as α_s. It determines how strongly a quark couples to a gluon. In gauge theories, the vector bosons can split into quantum loops of particles and antiparticles subject to their corresponding interaction [11, 19]. This gives rise to a phenomenon called charge screening, where a bare particle is surrounded by virtual particle pairs (see left panel of Fig. 2.2). In electrodynamics, these pairs make the charge appear smaller than it would appear without screening. If the charge is probed, a higher momentum means deeper penetration into the virtual particle cloud and a higher measured charge. In the case of QCD, however, a color charge antiscreening takes place. The bare quark charge appears larger if probed with low momenta. Only at higher momenta, the interaction weakens, meaning α_s decreases. This is commonly parametrized by the formula

$$\alpha_s(Q^2) = \frac{12\pi}{(33 - 2n_f)\log(Q^2/\Lambda^2)}, \tag{2.3}$$

where Q is the momentum transfer, Λ the QCD energy scale of around 200 MeV and n_f the number of quark flavours [11]. A summary of measurements of α_S is given in the right panel of Fig. 2.2.
In the limit of energies Q far larger than Λ =200 MeV, the right hand side of Eq. (2.3) vanishes. This fact is called asymptotic freedom, since the quarks become deconfined at high momentum transfers and behave as if they were free particles. This was shown in 1973 by David Gross and Frank Wilzcek and independently David Politzer, who received the Nobel price in 2004 for their discoveries [20–22]. In this regime, perturbative methods can be applied for calculations (pQCD). In the low energy regime, this is not the case. The running coupling shows this behaviour for numbers of flavour below 17, which can be directly extracted from Eq. (2.3). If the number of flavours were at least 17, the behaviour of $\alpha_s(Q^2)$ would be inverted.

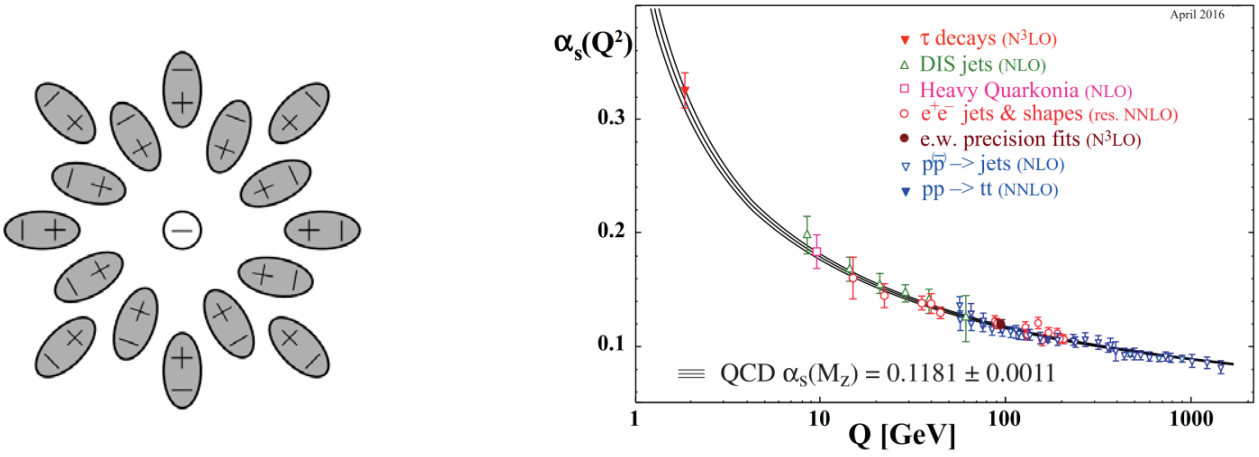

Figure 2.2: Left panel: Illustration of QED charge screening [19]. Right panel: World data on the behaviour of the QCD running coupling constant α_S in dependence of the momentum scale Q [23].

2.2.2 Numerical methods for QCD

QCD has no analytic solution. In high-energy regions, the decrease of the running coupling constant α_s allows the use of perturbative methods known from QED. However, the most interesting phenomena like the generation of the hadron masses or the binding of nuclei are intrinsically non-perturbative, becayse they take place at low energies Q of the order of the hadron masses ($\sim$ 1 GeV). For vanishing baryon chemical potential, i.e. when the number of baryons N_B is equal to the number of antibaryons $N_{\overline{B}}$ and high temperatures, QCD can be discretized with an imaginary time axis. This provides a solution on a lattice of points in spacetime, giving rise to lattice QCD (lQCD). lQCD attempts to solve the path integrals associated with QCD directly using Monte Carlo Methods [24]. The aim is to reach convergence as the grid size of the lattice becomes smaller and smaller. Research is currently conducted on the extension to finite baryon densities [25].
Another method are renormalization group methods, especially those using functional analytical methods. The renormalization group attempts to find transformations to different scales, which leave the physics of the system intact. In a sense, it is looking for a scale symmetry. This amounts to the integration of fluctuations in the system on larger and larger scales, until a fixed point of the system is reached and the system does not transform anymore under further scale changes. This provides then an effective description of the system [25, 26]. Many functional renormalization group methods use the Wetterich equation, which was derived by Wetterich et al. in 2002 and is a nonlinear, exact functional renormalization group equation [27, 28].

2.3 Spectral functions

Colliding electrons and positrons causes them to annihilate and create other charged particle-antiparticle pairs via a virtual photon. The lowest order diagrams for the creation of dimuons and diquarks are given in Fig. 2.3 a) and b) respectively. Because created quarks cannot be separated indefinitely, hadronization sets in and, in the simplest case, two mesons are created. Because the processes shown in Fig. 2.3 a)

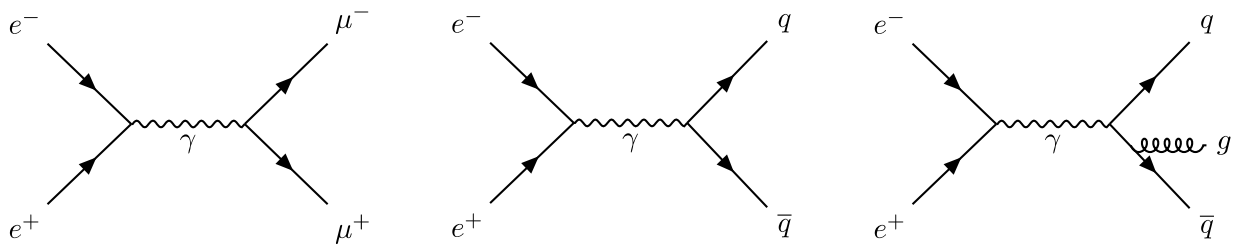

(a) (b) (c)

Figure 2.3: Feynman diagram for the annihilation of e^+e^- into muons (a), quarks (b), quarks radiating a gluon (c) [11, 29].

and b) are purely electromagnetic in nature, QED can be used to approximate the cross sections. For the e^+e^--annihilation into muons, the cross section fulfills

$$\sigma(e^+e^- \to \mu^+\mu^-) = \frac{4\pi\alpha_{\text{EM}}^2}{3Q^2}, \tag{2.4}$$

where Q is the center-of-mass energy. Since photons are color- and flavor-blind, from an electromagnetic point of view, the creation of a specific quark-antiquark pair $q\overline{q}$ of color c can be expressed as the creation of a dimuon of fractional quark charge e_q,

$$\sigma(e^+e^- \to q_c\overline{q_c}) = e_q^2\sigma(e^+e^- \to \mu^+\mu^-). \tag{2.5}$$

Since the creation of a quark of each of the three colors is equally likely and the dependence of flavor is only in the charge e_q associated with said flavor, the cross section for the creation of hadrons is enhanced by a factor of 3 due to color and a summation has to be performed over all different flavors accessible at the center-of-mass energy Q,

$$\sigma(e^+e^- \to \text{hadrons}) = 3\sum_{|2m_q|<Q} e_q^2\sigma(e^+e^- \to \mu^+\mu^-). \tag{2.6}$$

This gives rise to the R-ratio,

$$R = \frac{\sigma(e^+e^- \to \text{hadrons})}{\sigma(e^+e^- \to \mu^+\mu^-)} = 3\sum_{|2m_q|<Q} e_q^2, \tag{2.7}$$

providing a quantity probing the number of colors and flavours. Fig. 2.3 c) constitutes a first order correction,

$$R = 3\sum_{|2m_q|<Q} e_q^2\left(1 + \frac{\alpha_s(Q^2)}{\pi}\right). \tag{2.8}$$

The R-ratio is known very precisely in the vacuum from e^+e^--scattering experiments. The world data has been summarised by the Particle Data Group and can be seen in Fig. 2.4, along with comparisons to the naive predictions from Eq. (2.7) and Eq. (2.8). Clearly, the predictions are not applicable close to the pole masses of hadronic resonances. Multiplying R by the square of the invariant mass, M^2, the electromagnetic spectral function, $\text{Im}\Pi_{EM}$, is obtainable via

$$RM^2 \propto \text{Im}\Pi_{EM}. \tag{2.9}$$

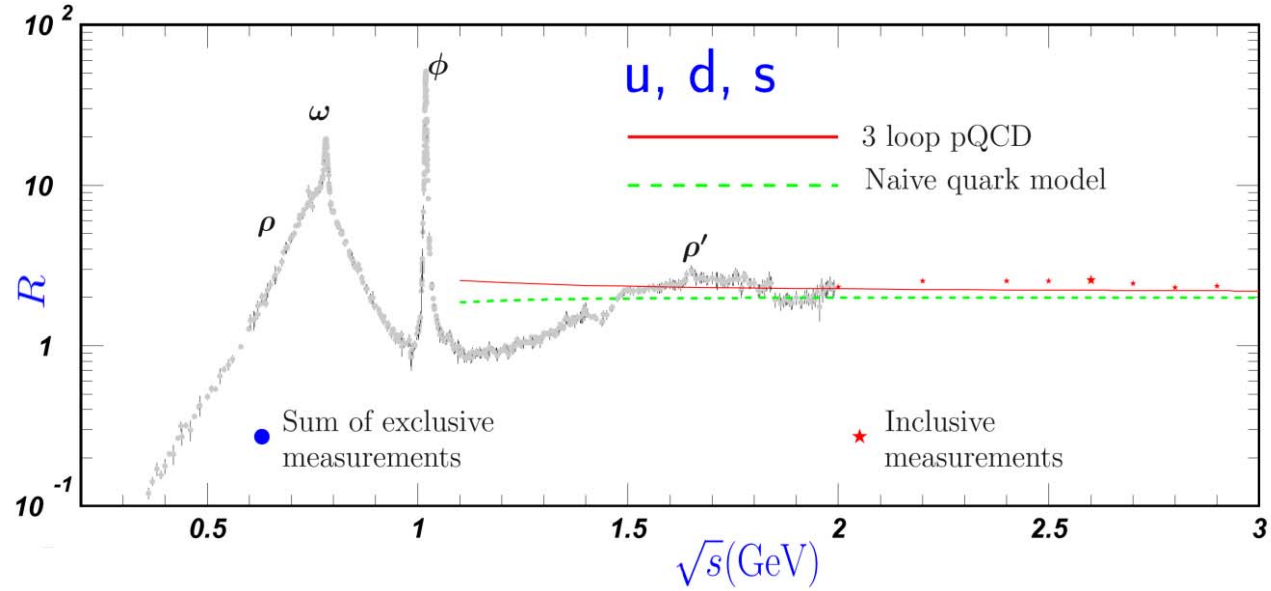

Figure 2.4: The R-ratio of the cross section of e^+e^- annihilation into hadrons to the cross section of annihilation into dimuons in the light quark regime. Also shown is the prediction from the naive quark model of Eq. (2.7) in green and a pQCD correction along the lines of Eq. (2.8) in red. [23].

The electromagnetic spectral function contains all information on the hadronic spectrum in the QCD vacuum and their electromagnetic interactions. It consists of the sum of the spectral functions of the hadrons and is equally well known as the R-ratio due to the simple relation between the two (Eq. (2.9)). Mathematically, it is the imaginary part of the electromagnetic current-current correlator,

$$\Pi^{\mu\nu}_{EM}(q_0, q) = -i \int d^4x e^{i\mathbf{q}\cdot\mathbf{x}} \Theta(x^0) \langle [j^\mu(x), j^\nu(0)] \rangle, \tag{2.10}$$

taking a mean $\langle ... \rangle$ over temperature and baryon chemical potential, where j^μ is the electromagnetic current in the examined region. Considering quarks up to the strange quark, carrying charges of $2/3$ or $1/3$,

$$j^\mu_{EM} = \sum_{q=u,d,s} \overline{q}\gamma^\mu q e_q, = \frac{2}{3}\overline{u}\gamma^\mu u - \frac{1}{3}\overline{d}\gamma^\mu d - \frac{1}{3}\overline{s}\gamma^\mu s. \tag{2.11}$$

The last equation can be rearranged using the quark compositions of the vector mesons. Further details can be found in [30]. However, when a QCD medium is present, the interactions with surrounding hadrons start to distort the spectral functions. This will be discussed further in Section 2.6.1.

2.4 The chiral symmetry of QCD

The quark Dirac spinors have four components, which can be ordered in a column vector. Two components, called right-handed and left-handed, can be projected out using the projection operators P_L and P_R, defined as

$$P_{R/L} = \frac{1}{2}(1 \pm \gamma^5). \tag{2.12}$$

While the chirality operator γ^5 does not commute with the Hamiltonian and, therefore, is not a good quantum number for massive fermions, it corresponds to the helicity operator for massless particles, meaning it describes the direction of the spin of a particle relative to its direction of motion. Helicity is conserved.
The masses of the u- and d-quarks are small compared to the QCD scale Λ. In this sense, it is rectified to introduce the chiral limit, in which the first quark generation is assumed as massless and the other generations as infinitely heavy. Neglecting the gluon interactions, this reduces the Lagrangian in Eq. (2.1) to

$$\mathcal{L}_{\chi QCD} = \overline{u}(i\gamma^\mu D_\mu)u + \overline{d}(i\gamma^\mu D_\mu)d. \tag{2.13}$$

This can be rephrased via the the introduction of a vector

$$q = \begin{pmatrix} u \\ d \end{pmatrix} \rightarrow \mathcal{L}_{\chi QCD} = \overline{q}(i\gamma^\mu D_\mu)q. \tag{2.14}$$

Projecting out the right- and left-handed components with the projectors of Eq. (2.12) gives

$$\mathcal{L}_{\chi QCD} = \overline{q}_R(i\gamma^\mu D_\mu)q_R + \overline{q}_L(i\gamma^\mu D_\mu)q_L. \tag{2.15}$$

This leads to the astonishing property that $\mathcal{L}_{\chi QCD}$ is invariant under independent unitary transformations of $q_{L/R} \rightarrow U_{L/R}q_{L/R}$. This is called the chiral symmetry of quantum chromodynamics. It has several implications. Tranformations where $U_L = U_R$ are called vector transformations. These correspond to the conservation of baryon number and isospin currents of the strong interaction. For the axial vector transformations $U_L = -U_R$, the matter is more complicated.

2.4.1 Spontaneous breaking of chiral symmetry

A symmetry is called spontaneously broken if the Hamiltonian obeys said symmetry but the ground state does not. Consider a ferromagnet. Below the Curie temperature T_C, the spins of the system align and the ferromagnet exhibits spontaneous magnetization in a random direction, breaking the rotation group by introducing a preferential axis. Due to the different magnetization states being degenerate, massless excitations called spin-waves or *magnons* arise. According to Goldstone's theorem, the emergence of massless bosonic excitations (Goldstone bosons) is a general property of spontaneously broken symmetries [31].
Another example is the global breaking of U(1) phase symmetry in a system exhibiting local electromagnetic U(1) gauge symmetry in the case of superconductivity. This is due to the small attractive interaction due to phonons giving rise to a condensate of electron pairs called Cooper pairs in the ground state of a metal [19, 32]. The situation for the QCD vacuum is similar. The energy cost of creating massless quark pairs is small and their interaction is strong at low energies. Because the quarks are created as quark-antiquark pairs and their spin and momentum need to cancel out due to the conservation laws, they carry a chiral charge. This leads to the expectation value of the operator $\overline{q}q$ being finite. Since

$$\langle\overline{q}q\rangle = \langle 0|\overline{q}q|0\rangle = \langle 0|\overline{q}_L q_R + \overline{q_R} q_L|0\rangle \neq 0, \tag{2.16}$$

this non-zero expectation value clearly breaks the chiral symmetry in its combination of right- and left-handed spinors. While the vector symmetries are still active, the axial vector symmetries are broken spontaneously. In principle, this should give rise to four Goldstone bosons (one for the breaking of the $U(1)_A$ and three for the breaking of $SU(2)_A$). However, $U(1)_A$ is already broken by a quantum anomaly. This leads to the emergence of three Goldstone bosons, the pions. It is immediately recognized that the

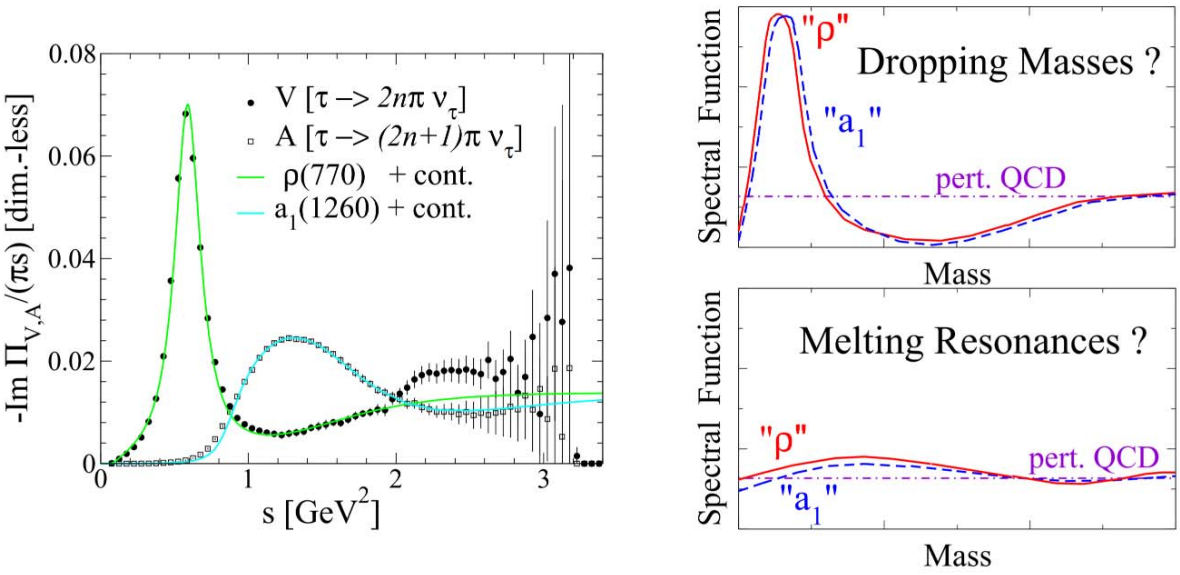

Figure 2.5: Left panel: ρ- and a_1 spectral data from the decay of τ-leptons and fits for the vacuum. Right panel: Illustration of the melting resonance and dropping mass scenarios for the restoration of chiral symmetry [34].

pions are not massless as they should be as Goldstone bosons. This is due to the finite quark masses, which were neglected in Eq. (2.13). It can be shown that

$$m_\pi^2 = (m_u + m_d)\frac{M^2}{f_\pi} \tag{2.17}$$

holds for the masses of the pions, where f_π is the pion decay constant of 93 MeV and M is a parameter of the order of 400 MeV. This shows that the breaking of chiral symmetry comes with a generation of the hadron masses in the limit of small quark masses. The pion mass can also be used as a measure of the chiral condensate, which cannot be measured directly. The **G**ell-Mann-**O**akes-**R**enner relation (GOR) [33] suggests a link between the chiral condensate and the pion mass,

$$m_\pi^2 f_\pi^2 = -2m_q\langle\bar{q}q\rangle. \tag{2.18}$$

This goes even further. If the chiral symmetry were realized in the vacuum, due to the conservation of axial vector currents, each hadron should come with a chiral partner of the same mass, transforming into each other under chiral transformations. However, this is not the case.

2.4.2 Chiral partners and restoration of chiral symmetry

Consider the ρ-meson. The ρ-meson is a vector meson with a mass of 770 MeV/c^2 [23]. Analogously to the pion, there are three isospin states of the ρ-meson, ρ^+, ρ^0 and ρ^-, meaning it consists of three states in an

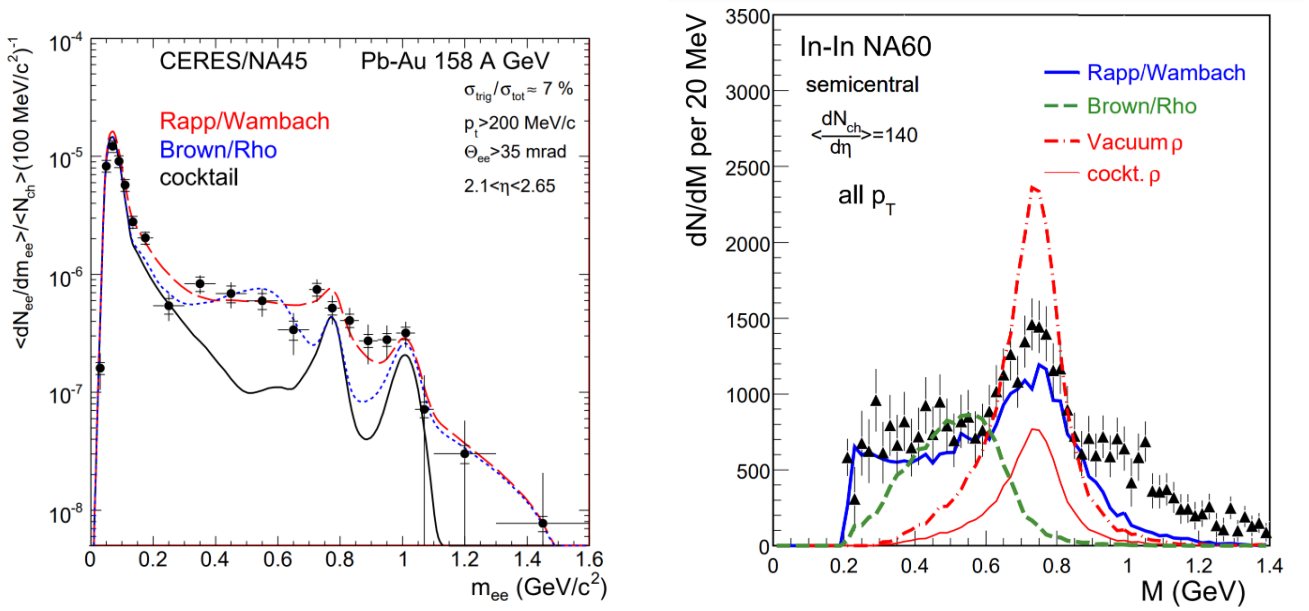

Figure 2.6: Left panel: CERES/NA45 results on the hadronic spectrum overlayed with differing spectral functions. The NA45 data do not allow a decisive conclusion. Right panel: The ρ-spectral function compared to the models. The Rapp-Wambach spectral function predicts a melting of the resonances and fits the data best [35].

isospin-triplet. The quark composition of the ρ-mesons is given as

$$|\rho^0\rangle = \frac{1}{\sqrt{2}}(|\bar{u}u\rangle - |\bar{d}d\rangle), \tag{2.19}$$

$$|\rho^-\rangle = |\bar{u}d\rangle, \tag{2.20}$$

$$|\rho^+\rangle = |\bar{d}u\rangle. \tag{2.21}$$

As a vector meson, it has spin and parity 1^-. The ρ-meson is almost exclusively created by the annihilation of two pions. This is also its most prominent decay. With a branching ratio of $(4.55\pm0.28)\times10^{-5}$, it can decay into a dielectron [23]. A candidate for its chiral partner is the a_1-axial vector meson with a mass of 1260 MeV/c^2 and a spin parity of 1^+ [23]. Clearly, the masses of both mesons are not degenerate. A parametrization of this is given by one of the Weinberg sum rules [36],

$$\int_0^\infty [\rho_V(\mu^2) - \rho_A(\mu^2)]\mu^{-2}d\mu^2 = f_\pi^2, \tag{2.22}$$

where $\rho_i(\mu^2)$ is the axial vector and vector spectral function respectively. The corresponding vacuum spectral functions can be seen in Fig. 2.5 as measured in τ. The Gell-Mann-Oakes-Renner relation links this to the chiral condensate. Using current algebra and postulating that only the ρ-meson is a significant factor in the sharply peaked vector-spectral function, Weinberg also showed that in the vacuum

$$\sqrt{2} = m_\rho/m_A = [1 - f_\pi^2 m_\rho^2/g_\rho]^{-\frac{1}{2}} \tag{2.23}$$

holds true. This can be clearly seen in the left panel of figure 2.5. Using the GOR, this splitting is directly linked to the chiral condensate.
How is chiral symmetry restored? Using statistical physics, a decrease of the chiral condensate at finite temperatures T and densities ρ can be predicted [37]:

$$\langle \bar{q}q \rangle_T = \langle 0|\bar{q}q|0\rangle \left(1 - \frac{T^2}{8f_\pi^2}\right), \tag{2.24}$$

$$\langle \bar{q}q \rangle_\rho = \langle 0|\bar{q}q|0\rangle \left(1 - \frac{\Sigma_{\pi N}}{m_\pi^2 f_\pi^2}\rho\right), \tag{2.25}$$

where $\Sigma_{\pi N}$ is the quark condensate in presence of nuclei multiplied with the quark mass. Using Eq. (2.23), the restoration of chiral symmetry is visibly accompanied an approximate degeneration of the vector and axial vector spectral functions at high temperatures and densities. Several scenarios have been discussed in the past, including a melting of the resonances, and a dropping of the masses [38, 39]. In the mass region below 0.6 GeV/c^2, both predictions match the results of the CERES/NA45 experiments within experimental uncertainties, as the left panel of Fig. 2.6 shows. However, the right panel shows that the NA60 dimuon experiment measured data demonstrating melting of the ρ-meson resonance while disfavouring a dropping-mass scenario [35].

2.4.3 Chiral vector-axial vector Mixing

While the ρ-meson's spectral function can be measured via the decay into a lepton pair $(e^+e^-, \mu^+\mu^-)$ via a virtual photon, which has the exact same quantum numbers as the ρ-meson, the case is different for the a_1-meson. It cannot decay via a virtual photon because this would violate parity conservation. It mostly decays into three pions. Pions are themselves strongly interacting and therefore their spectral function itself is distorted by the medium, providing an additional difficulties to measurement of the axial vector spectral function. In the medium, the ρ-spectral function produces an excess yield in the region above its

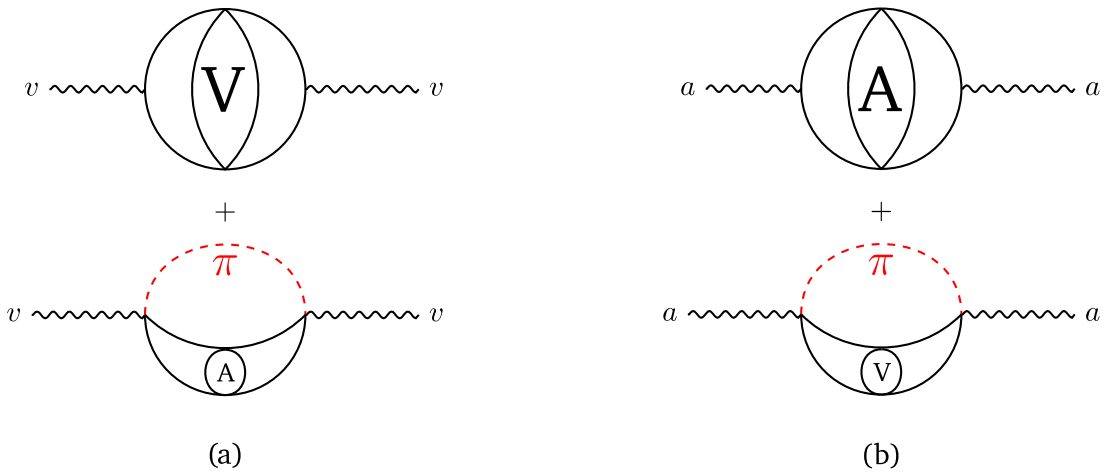

(a) (b)

Figure 2.7: Schematic diagram for the mixing of axial and vector meson correlators. Left panel: Mixing of axial vector meson and pion to contribute to the vector spectral function (a). Right panel: Mixing of vector meson and pion to contribute to the axial spectral function (b) [29, 40].

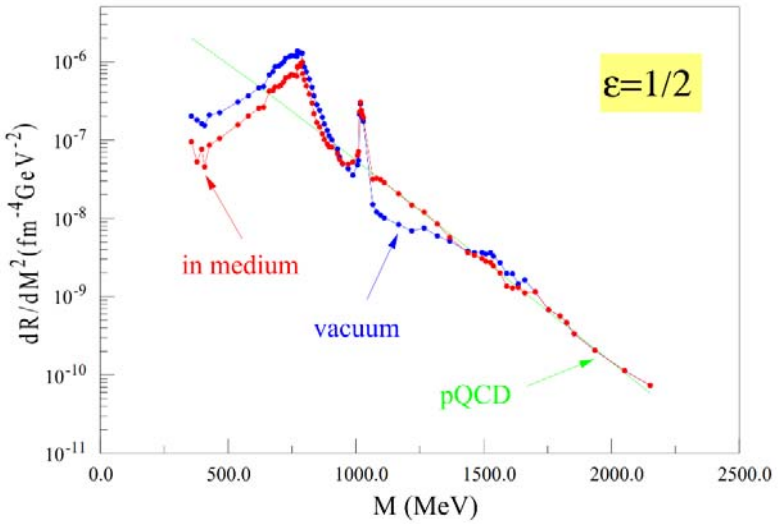

Figure 2.8: The spectral function in three different parametrizations. The green curve is the parametrization in the naive quark model, the blue curve is the vacuum spectral function and the red curve is the mixed in-medium prescription which produces an excess yield above the ρ-mass of about 30 % [38].

peak. This yield can be explained by chiral mixing. If a vector meson couples to a scalar pion from the medium having negative parity, they contribute to the axial vector channel, since the parities get multiplied ($-1^2 = 1$) and the spins can only couple to J=1. The same arguments hold for the interaction of an axial vector meson and a pion, which then contribute to the vector channel. The process is illustrated in Fig. 2.7. Introducing the mixing parameter $\epsilon = T^2/6f_\pi^2$, chiral mixing can be expressed in terms of the spectral functions as

$$\Pi_{V,A} = (1-\epsilon)\Pi_{V,A}^{(T=0)} + \epsilon\Pi_{V,A}^{(T=0)}, \tag{2.26}$$

leading to the conclusion that at low temperatures, the dilepton excess yield can be explained by a large contribution of chiral mixing, while other effects, e.g. the formation of a quark gluon plasma (see Section. 2.5.3), are negligible, which can also be seen in the parametrization in Fig. 2.8 [41].

2.5 QCD phase diagram

Like any known substance, strongly interacting matter undergoes phase transitions at certain temperatures and pressures. While matter governed by electromagnetism, e.g. water molecules, shows different phases in the form of ice (solid), water (liquid) and steam (gaseous), strongly interacting matter also displays various phases. They can also be summarized in a phase diagram of matter governed by QCD. It needs to be made clear that the exact structure of the QCD phase diagram is unknown, which especially concerns the phase transitions. In Fig. 2.9, two possible scenarios are shown. Nonetheless, it is certain that in the region between zero and nuclear ground state density, the QCD-phase diagram has two regions that immediately meet the eye. The first at low temperatures is the hadron gas phase, in which quark matter basically behaves as is known from light nuclei. This is called confinement. The second distinct region is the quark-gluon-plasma (QGP) existing at high temperatures or densities. Heavy-ion collisions in the few

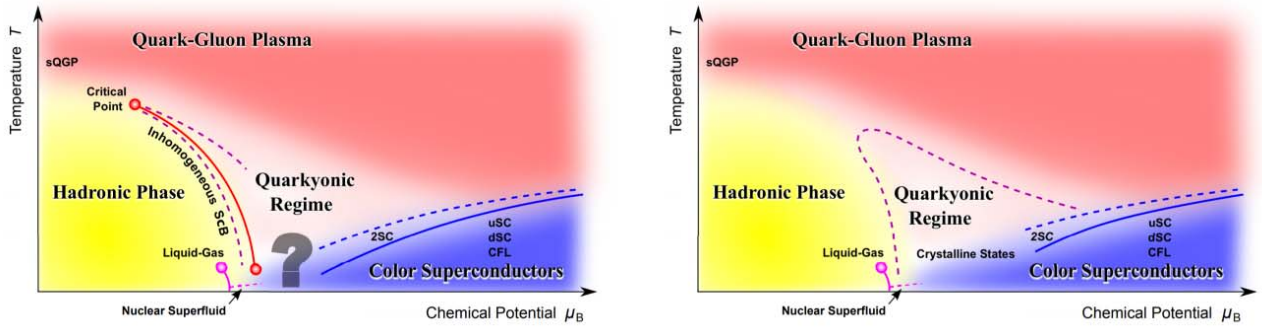

Figure 2.9: Two possible phase diagrams of QCD matter, differing primarily in the inclusion of the critical point(s) and the phase transition line [42].

GeV range will probe the higher densities together with astronomical observables like gravitational waves from neutron star mergers [43, 44].

2.5.1 Phase Transitions

Phase transitions are lines in a phase diagram where discontinuities in the thermodynamic potentials or their derivatives are observed. If the discontinuity is found in the n^{th} derivative, one speaks of a phase transition of n^{th} order according to the Ehrenfest classification [45]. This means that the macroscopic state of a system can have drastically different properties after crossing a phase boundary. The end of some transition lines is marked by a critical point. Beyond the critical point, the differences between different phases of matter vanishes, critical phenomena like opalescence (rapid shifting between different phases) arise. Critical points are interesting as system-independent behaviour arises around these points. This means that information extracted from one system can be transferred to a certain degree to other systems - an example is the behaviour of magnetization m, where around the critical Curie temperature T_C

$$m \propto (T_C - T)^{\beta} \tag{2.27}$$

holds. Similar behaviour is observed for example in liquid-gas transitions of many materials, where the magnetization m in Eq. (2.27) is replaced by the difference of the density and the critical density, $\rho - \rho_C$ [26].

2.5.2 Confinement and the hadronic phase

Free quarks have never been observed, even though their fractional electric charges would let them stand out above non-colored, integer-e particles. Instead, quarks form groups of three quarks (called baryons) or pairs of one quark and an anti quark (called mesons). This is due to the fact that the force between color charges is constant and independent of their distance. In reminiscence of the three primary colors of light, which give white when mixed together, generally only "white" or "colorless" free objects may exist. In baryons, this is given by mixing all three primary colors, while in mesons, a linear combination of color and corresponding anticolor serves this requirement, as shown schematically in Fig. 2.10.
Other, more exotic combinations like two pairs of $q\overline{q}$ or $qqqq\overline{q}$ have been observed at CERN, but the analysis of the exact binding is ongoing [47, 48]. Trying to remove a quark from the hadron results in the creation

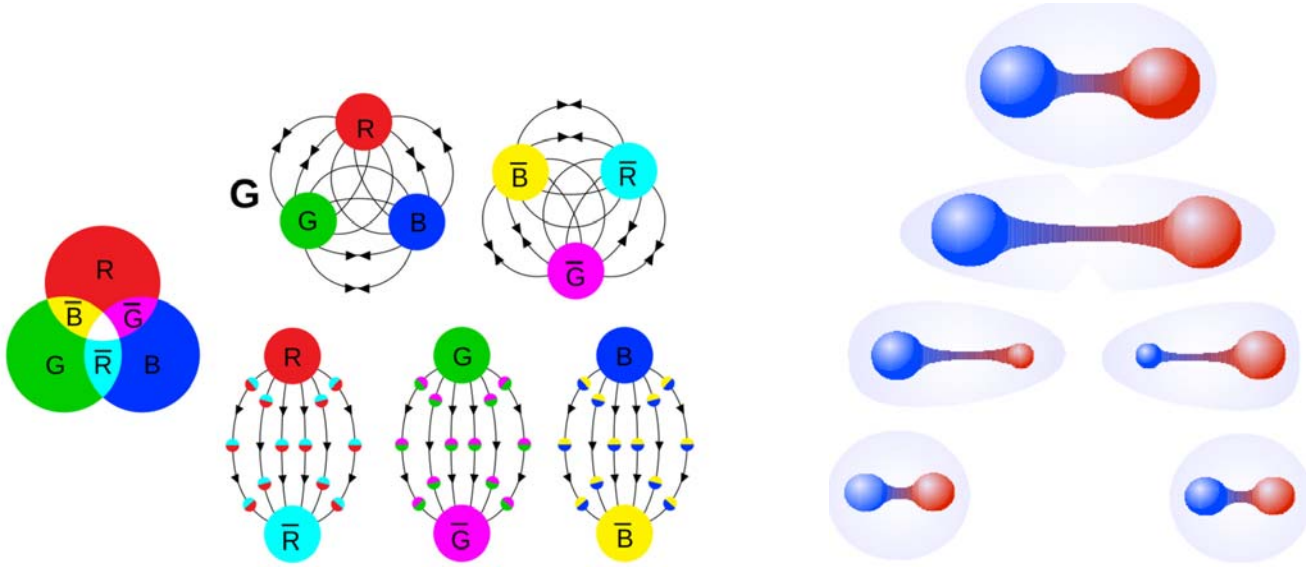

Figure 2.10: Left panel: Artistic impression of the grouping of quarks in color neutral hadrons. Right panel: Artistic impression of confinement and the creation of a quark-antiquark pair if the energy density is sufficiently high [46].

of gluonic color flux tubes with an energy density high enough to create a quark-antiquark pair to balance out the separated color charges and reduce the energy density. The result is the creation of one or more mesons (see Fig. 2.10). In the QCD phase diagram, the prominent region with confinement is the hadronic phase (yellow in Fig. 2.9). The hadronic phase itself is split into two regions by the nuclear liquid-gas phase transition at small temperatures. Towards lower net-baryon densities, hadrons are unbound and behave nearly as an ideal gas. At higher densities, nuclear matter forms, hadrons are bound in nuclei and behave more like a liquid, which is supported by several observables, most prominently by the liquid-drop model and its application to the binding energy in nuclei and the nearly constant nuclear density [49]. This type of matter is also found in the mantle of neutron stars [50].

2.5.3 Quark-Gluon-Plasma

Toward higher temperatures, the coupling gets weaker and the confinement is gradually weakened. At vanishing baryon chemical potential, lattice QCD predicts a cross over from the hadronic phase to a deconfined phase, in which the elementary degrees of freedom in QCD, quarks and gluons, act as independent particles in a gas. This is called a quark-gluon-plasma (QGP, red in Fig. 2.9). It is suspected that this kind of matter was present around 10 μs after the Big Bang. A QGP has first been observed at the **S**uper **P**roton **S**ynchrotron (SPS) accelerator at CERN during the lead heavy ion program started in 1994. In 2000, CERN announced compelling evidence for the formation of a QGP [51]. The quark gluon plasma seems to be described well by employing the notion of an almost perfect fluid with the highest vorticity ever measured [52]. At finite net-baryon density, coming with the cross over into the quark-gluon plasma or at slightly smaller temperatures, the restoration of chiral symmetry might be marked by a first order phase transition with a critical point at the end [42]. An intermediate state is assumed to exist between the hadronic and QGP phases in form of the quarkyonic regime, where a mixture of almost deconfined baryons with strong hadronic interactions and quasi-free quarks exists (white areas in Fig. 2.9)

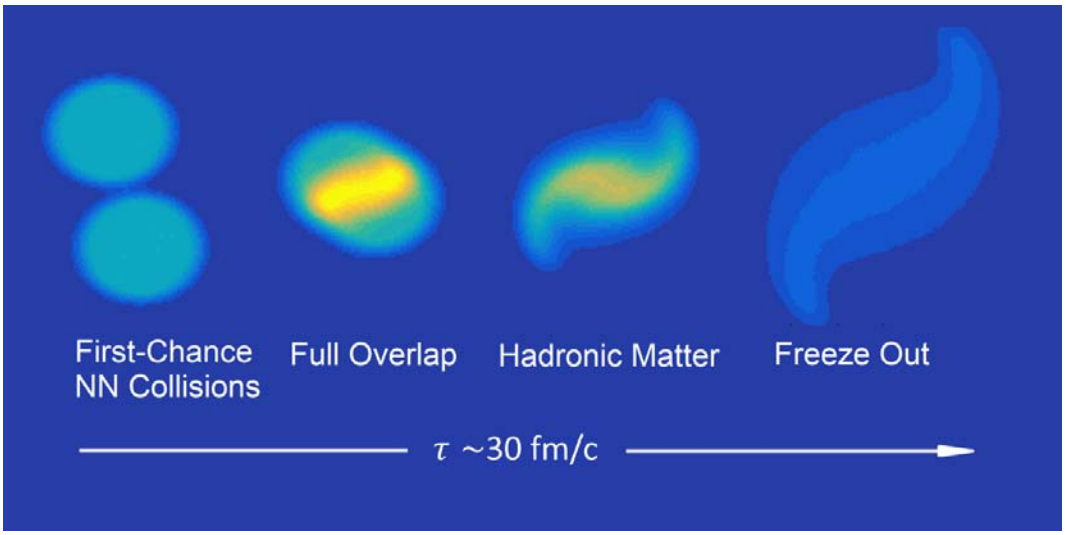

Figure 2.11: Visualization of the history of a heavy-ion collision. The highest baryon densities and temperatures are reached in the full overlap stage in the fireball after a short amount of time, while expansion of the fireball matter mandates cooling. Interactions do not occur after the freeze out [53, 54].

2.5.4 Color Superconductors

Just as in superconductors at low temperatures and high electron densities, at low temperatures and very high densities, the formation of quark pairs might take place in a similar way to the cooper pairs in electromagnetic super conductors. This is due to the similarity of the QCD field strength tensor to the QED field strength tensor. This leads to the formation of a medium through which a color current can flow without any resistance or dissipation (blue region in Fig. 2.9). This phase might be subdivided into several subphases with differing specifics [42].

2.6 Heavy-Ion collisions

Due to the phenomenon of confinement discussed in Section 2.5.2, quark matter can only be accessed for short amounts of time of the order of 10 fm/c in heavy ion collisions at (ultra-)relativistic energies provided by particle accelerators. Heavy-ion experiments generally come in two different setups, colliding-beam setups, and fixed-target setups. While colliders like LHC can reach higher center-of-mass energies $\sqrt{s_{NN}}$, the luminosity and thus the number of events recorded is higher in fixed-target setups.
The collision of nuclei and the creation of the reaction products are among the most transient phenomena known to science, on time scales of the order of $1\text{fm}/c \sim 3 \times 10^{-24}$ s. These time scales make any direct measurements impossible. Instead, experiments measure properties of matter created in heavy-ion collisions via particle detection, such as their charge, mass and momentum, to identify them and their exact origin. Fig. 2.11 shows the typical evolution of a heavy-ion collision. The incoming nuclei experience a Lorentz contraction, making them look more like disks than three dimensional structures depending on the collision energy. In the moment of the collision, some nucleons do not interact and continue on their path after being torn out of their mother nuclei. They are known as spectators, their number depends on the impact

parameter (the distance of the nuclei's centers). The interacting nucleons form the fireball. Depending on the collision energy, the fireball consists either of a dense hadronic medium or a QGP. In the former case, high baryon net-densities emerge, as the incoming nuclei are stopped immediately and form the major part of the fireball matter. In the latter case, the QGP is made up of free quarks, antiquarks and gluons hadronizing into baryon-antibaryon pairs due to the enormous energy densities upwards of 1 GeV/fm^3 [55]. This leads to low net-baryon densities, since the original nucleons continue on their path and leave the interaction zone. After the formation of the QGP, a hadronization sets in with the expansion and cooling of the fireball, giving rise to a hadronic medium. After the following chemical freeze-out, inelastic collisions are no longer happening, meaning the composition of the system is fixed afterwards. After the kinetic freeze-out, all interactions stop and the expanding medium cools and diffuses.

2.6.1 Dileptons as probes of heavy-ion collisions at (ultra-)relativistic energies

While any form of hadrons originating in the fireball is an important probe for the dynamics inside of the hot and dense medium, hadrons, as strongly interacting particles, carry predominantly information on the late stages of a collision, as they are subject to violent strong interactions after their formation.
In contrast, electromagnetic probes (l, γ) do not carry color charge. This means that they retain properties from the time of their creation, making them an excellent probe for in-medium spectral functions, as they leave the fireball undisturbed after they have been formed. Additionally, virtual photons (materializing in lepton pairs) are formed during all phases of a heavy-ion collision and can therefore be used to study properties of QCD matter during the full evolution of the fireball. Moreover, the longer the fireball exists, the more dileptons are produced, so the number of dileptons produced can give an indication of the lifetime of the fireball [56].
The dilepton emission rate is given by the McLerran-Toimela-formula [57],

$$\frac{dN_{ll}}{d^4x d^4q} = -\frac{\alpha_{EM}^2}{\pi^3 M^2} L(M^2) f^{BE}(q_0, T) \mathrm{Im}\Pi_{EM}(M, q, \mu_B, T). \tag{2.28}$$

In the McLerran-Toimela-Formula, $f^{BE}(q_0, T)$ is the Bose-Einstein-factor at temperature T and energy q_0, M is the invariant mass with $M^2 = q_0^2 - q^2$, L is a phase space factor suppressing lepton-production below the threshold of $2m_e$ and $\mathrm{Im}\Pi_{EM}$ is the electromagnetic spectral function as established in 2.3.
An often employed tool is the vector meson dominance model, where the dilepton production is mainly powered by the three vector mesons ρ, ω and ϕ, saturating any hadronic currents and reducing the spectral function to the sum of the vector meson propagators,

$$\sum_{v=\rho,\omega,\phi} \left(\frac{m_v^2}{g_v}\right)^2 \mathrm{Im}D_v^{\mathrm{vac}}(M, q; T = 0, \mu_B = 0) D_v^{\mathrm{vac}}(M, q; T = 0, \mu_B = 0) = \frac{1}{M^2 - m_V^2}. \tag{2.29}$$

The ρ-meson decays within the lifetime of the fireball ($\tau = 1.5\,\mathrm{fm/c}$) and outshines the ω-meson by one order of magnitude in the dilepton yield. This dominant role in the formation of dileptons makes it especially interesting.
However, as the restoration of chiral symmetry begins to manifest in a medium, the spectral functions begin to change - mainly expressed by a melting of the resonances. Simulations of this can be seen in Fig. 2.12, done via the spectral function developed from a Many-Body-ansatz bei Rapp and Wambach [38]. The Rapp-Wambach spectral function has successfully reproduced dilepton data from SIS18 to LHC energies (see e.g. Fig. 2.6, 4.1). In this approach, the meson propagator picks up terms from the medium, such

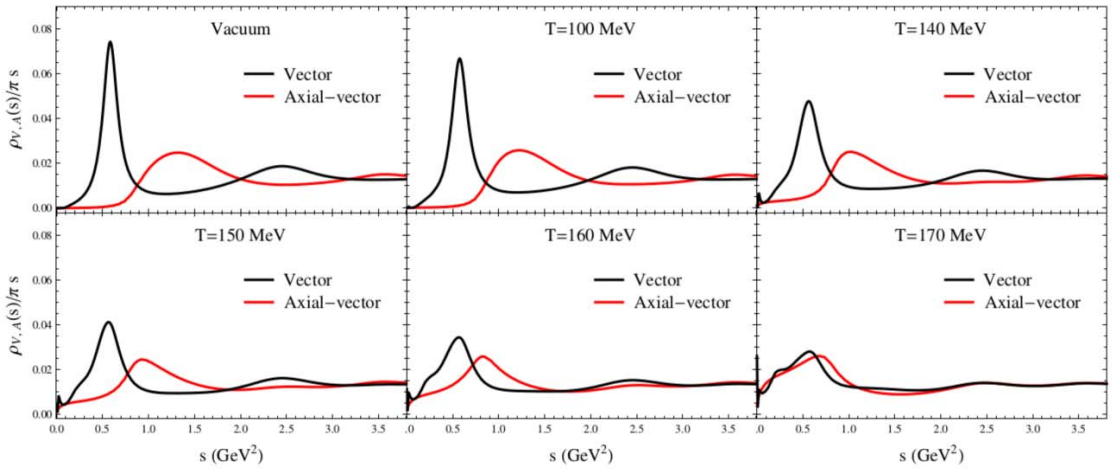

Figure 2.12: Simulation of the vector and axial vector spectral function at different Temperatures T [58].

as an interaction of the virtual pion cloud ($\pi\pi$) of the ρ-meson or direct scattering with baryons (B) and mesons (M) (see Fig. 2.13) [30]. Thus, the propagator is given in a medium in thermal equilibrium by

$$D_\rho(M, q; T, \mu_B) = \frac{1}{M^2 - m_\rho^2 - \Sigma_{\rho\pi\pi} - \Sigma_{\rho B} - \Sigma_{\rho M}}. \tag{2.30}$$

In thermal equilibrium, the abundances of mesons and baryons are related to the intensive variables like temperature, baryon density or chemical potential. If for example by the decay of resonances, pions are more abundant than expected due to equilibrium properties, more ρ-mesons are produced by pion interactions. One makes use of a fugacity factor to account for this fact. The chemical potential for a particle species of mass m, spin-degeneracy g in equilibrium at temperature T and density n is given as

$$\mu = T \ln\left(\frac{2\pi^2 n(\hbar c)^3}{gTm^2 K_2\left(\frac{m}{T}\right)}\right), \tag{2.31}$$

where K_2 is the modified Bessel function of second kind and second order as shown in Section 6.8 of [54]. The fugacity factor follows as

$$z = \exp\left(k\frac{\mu_\pi}{T}\right) = \left(\frac{2\pi^2 n(\hbar c)^3}{gTm^2 K_2\left(\frac{m}{T}\right)}\right)^k, \tag{2.32}$$

where k is the number of pions involved in the formation of a ρ-meson. Analysis of the collision history of UrQMD particles gives $k = 1.12$ at SIS18 energies [54].

2.7 HADES

The **H**igh-**A**cceptance-**Di**-**e**lectron-**S**pectrometer (HADES) is a particle detector located at the GSI Helmholtzzentrum für Schwerionenforschung in Darmstadt. It was built by a collaboration of scientists from 24 universities

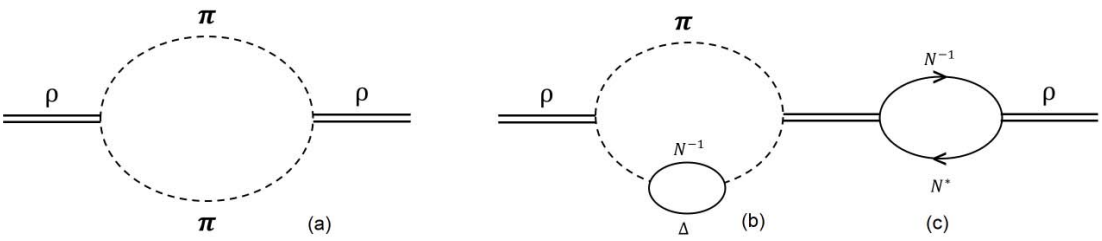

Figure 2.13: Left panel: In the vacuum, only the virtual pion cloud contributes to the the ρ-spectral function (a). Right panel: In the medium, additional interactions as higher order coupling of the pion cloud (b) or coupling to baryons (c) can take place [54].

in 11 countries. HADES studies properties of QCD matter at highest net-baryon densities using rare and penetrating probes, with dileptons receiving special attention due to their properties discussed in Section 2.6.1.
HADES has a six-fold symmetry, meaning it consists of sectors with identical construction. This setup gives HADES a large acceptance in the ϕ direction of almost 360° and between $18°$ and $85°$ in the θ direction [59]. The symmetry can be seen in the right panel of Fig. 2.14. The left panel of Fig. 2.14 shows a schematic cross section of the detector. It is build from a variety of sub-detectors serving different aims. The target of a thin solid foil or a liquid is placed in between the START and VETO detector starting the time of flight (TOF) measurement. The ring-imaging Cerenkov detector (RICH) uses the Cerenkov effect to determine whether a particle is an (anti)electron or a hadron, since electrons are two orders of magnitude lighter than any hadron. Multiwire drift chambers (MDC) measure the particles trajectory before it enters a toroidal magnetic field produced by a super conducting magnet. In this field, particles are bent according to their charge and momentum onto a new trajectory which is determined by a second set of MDCs. The TOF measurement is finished by resistive plate chambers and the TOF-wall, after which the energy of electromagnetically interacting particles is determined by the electromagnetic calorimeter ECAL, consisting of over 1000 lead-glass based modules with the corresponding read-out electronics. The forward wall characterizes centralities and reaction planes.
Thanks to high interaction rates of the order of 16 kHz for heavy-ion collisions, HADES is able to collect sufficient statistics to reconstruct rare (1 decay of $\rho \to e^+e^-$ per one million collisions) signals.

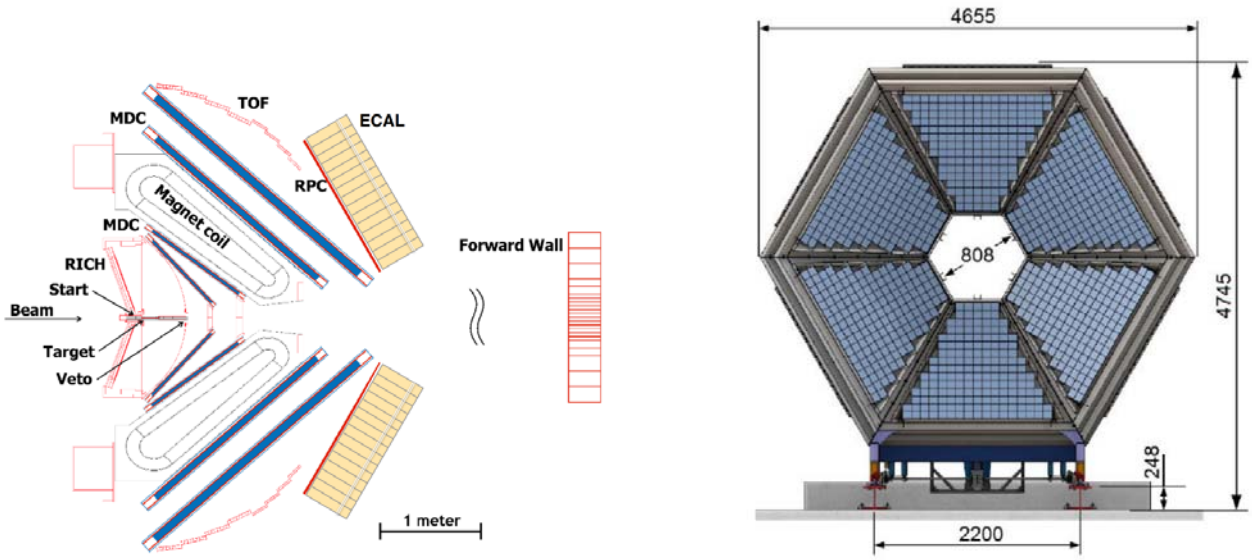

Figure 2.14: Left panel: Schematic cut through the HADES detector to show the different components. Right panel: Six-fold symmetry of the HADES-detector with measures in mm [60].

3 Modelling of heavy-ion collisions

The interpretation of any experimental data obtained from heavy-ion collisions needs a comparison to theoretical simulations to obtain physical information and check for consistency of a used model. This can be done in several ways. The two main approaches are macroscopic models, including thermal fireball and hydrodynamic models, and microscopic models. In macroscopic models, the whole fireball is considered and evolved as an entity, while microscopic models aim to describe the fireball and its evolution by the interactions of individual elementary particles or hadrons. There are also hybrid models which use hydrodynamics for the high energy transport and microscopic models if the temperature is reaches below a freeze-out temperature.

3.1 Hydrodynamical approaches

Hydrodynamical approaches can be considered macroscopic in the sense that they do not consider individual particles. The collision system and its variables are taken to evolve as behaving as a fluid would. This means that they obey the continuity equations for particle density as well as the conservation of energy and momentum, written as

$$\partial_\mu J^\mu = 0, \tag{3.1}$$

$$\partial_\mu T^{\mu\nu} = 0. \tag{3.2}$$

In Eq. (3.1), $J^\mu = nu^\mu$ is the baryon density current with the baryon density n and the components of the relativistic four-velocity $u = \gamma(1, \vec{\beta})$, while in Eq. (3.2), $T^{\mu\nu}$ is the energy momentum tensor defined as $T^{\mu\nu} = [(\epsilon + P)u^\mu u^\nu - P\eta^{\mu\nu} + \Pi^{\mu\nu}]$, where ϵ is the energy density, P is the pressure of the system and $\Pi^{\mu\nu}$ is a term correcting for viscosity [61]. However, it appears that the viscosity is extremely low for matter created in heavy-ion collisions [52]. To predict particle spectra, a hadronization algorithm is employed. An additional input is an equation of state, meaning a relation of pressure and energy density. Without this equation of state, the solution of the Eq. (3.1) and Eq. (3.2) becomes much harder or even impossible. This equation needs to be computed separately, e.g. by using lattice QCD or employing hadron resonance gas models.
Hydrodynamics is only applicable if the system is fully thermalized. In hydrodynamic simulations, rapid thermalization is assumed after a short time. For example, the **M**onotonic **U**pstreamcentered **S**chemes for Conservation Laws in heavy-**I**on **C**ollisions (MUSIC) uses thermalization after only 0.4 fm/c to accurately describe the anisotropy coefficients of heavy-ion collisions at LHC and RHIC [62, 63].
It can be seen in Fig. 3.1, that the flow coefficients for collisions of large nuclei are well described by hydrodynamic simulations, however, for large centralities and small systems, this description is less accurate. Since there is a considerably penetration time of the nuclei at small $\sqrt{s_{NN}}$, other models might be better applicable there.

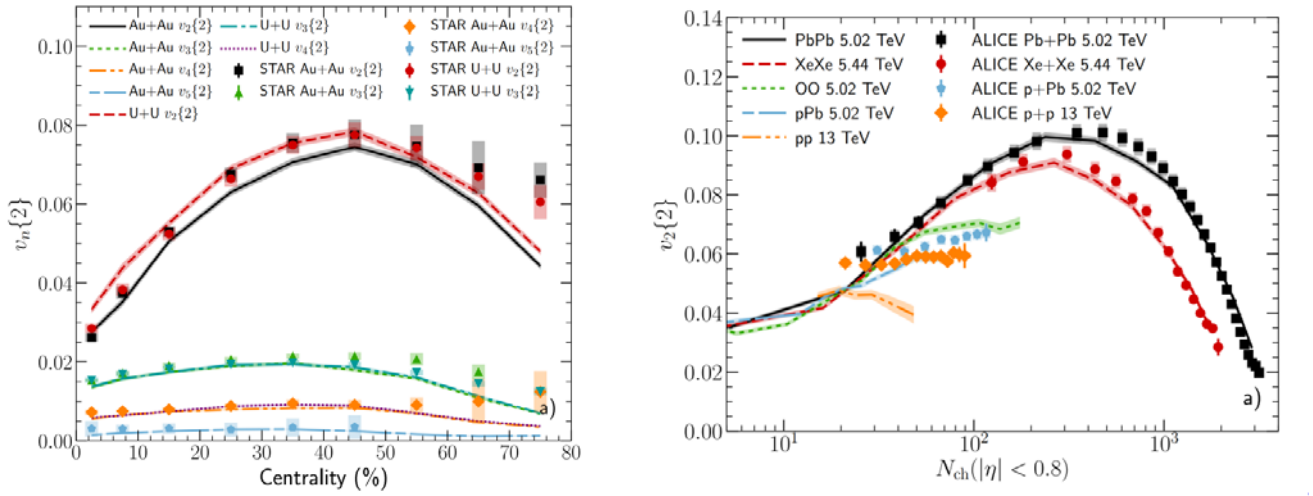

Figure 3.1: Left panel: $v_2\{2\}$ vs. multiplicity of charged hadrons at rapidities $\eta < 0.8$ compared to MUSIC predictions. Right panel: Flow coefficients $v_n\{2\}$ plotted against the centrality as measured by STAR at RHIC compared to the MUSIC predictions.[63].

3.2 Microscopic transport calculations

Microscopic transport models attempt to describe the full evolution of a heavy ion collision by following each particle over its path through spacetime while modelling interactions with other particles in the form of elastic and inelastic collisions by Monte Carlo simulations. In this work, UrQMD, GiBUU, SMASH and PHSD will be compared. In general, the models are all based on transport theory, namely the Boltzmann- or the **B**oltzmann-**U**ehling-**U**hlenbeck-equation (BUU).
The BUU equation is an integro-differential equation describing the evolution of the phase space density of a gas [61],

$$p^\mu \frac{\partial f}{\partial x^\mu} + m \frac{\partial (K^\mu f)}{\partial p^\mu} = \frac{1}{2} \frac{g}{(2\pi\hbar)^3} \int_{\mathbb{R}^3} \frac{d^3p_2}{E_2} \int_{\mathbb{R}^3} \frac{d^3p_1'}{E_1'} \int_{\mathbb{R}^3} \frac{d^3p_2'}{E_2'} W(p1', p2' \leftarrow p_1 p_2)(f_1' f_2' \overline{f} \overline{f}_2 - f f_1 \overline{f}_1' \overline{f}_2') \quad (3.3)$$

The first term on the left hand side describes the propagation and would form a continuity equation if set to 0, the second term describes the movement in a force field (external or mean-field), while the right hand side is called the collision term. It consists of a positive gain- and a negative loss-term and describes the probability $W(p1', p2' \leftarrow p_1 p_2)$ of a particle of momentum p being scattered in or out of the phase space cell [64]. The models mostly assume detailed balance, meaning that W has the same value for the inverse reaction. $\overline{f}$ denotes $(1 \pm f)$ for bosons and fermions, respectively, and takes into account the Pauli principle for fermions. This is realized by so-called Pauli Blocking, where the phase space cell is checked for other particles carrying the same momentum, which effectively decreases the cross sections for fermions. Bose-enhancement, which is the inverse effect for bosons, has not been implemented in most models [65]. Neglecting these factors gives the classical Boltzmann equation [61]. Further, it is important to note that the BUU-equation itself is just a first order semi-classical expansion of the Kadanoff-Baym equations, which describe the transport of the Green's functions in a quantum field theoretical way [66, 67].
Most of the models use an ansatz, where particles are propagated in the potentials according to classical dynamics. This yields a solution to the transport equation if done correctly, however, the implementation varies widely.

To determine whether a collision of any kind has happened, the geometric collision criterion is normally employed:

$$\sqrt{\frac{\sigma_{tot}}{\pi}} < d. \tag{3.4}$$

In words, the distance d between two particles needs to be smaller than the radius of a circle with an area equal to their total interaction cross section σ_{tot}. Note that this constitutes a causality violation as the distance d is bridged instantaneously. However, a covariant approach is numerically taxing as transformations of four-vectors are necessary [65]. For some of the models, other collision criteria are also implemented, for example a stochastic criterion developed by Cassing et al. [68]. They are generally not fully tested and are used for specific setups only.

3.3 Potentials in nuclear collisions

In nuclear collisions, several different interactions are taking place. In UrQMD and GiBUU, a combination of Skyrme, Coulomb and Yukawa potentials can be used, while SMASH incorporates Skyrme and Symmetry potentials. PHSD employs a Skyrme potential up to energies of 2 GeV.

3.3.1 Skyrme potential

The Skyrme potentials are a class of effective potentials describing the interaction of nuclei in the nucleus introduced by Tony Skyrme in 1959 [69]. They describe contact interactions between free nucleons and generally depend on the momenta of the incoming particles. If only two body interactions are to be considered for the forces between nucleons, a density dependence arises from the contact interactions. For the transport models UrQMD, GiBUU and SMASH, a momentum independent Skyrme potential of the form

$$V_{Sk} = \alpha \left(\frac{\rho}{\rho_0}\right) + \beta \left(\frac{\rho}{\rho_0}\right)^{\tau} \tag{3.5}$$

is implemented. The second term stems from three- and four-body interactions alone, while the first term combines these with the two-body interactions. While the parameters of this momentum independent Skyrme potential can be chosen freely for the GiBUU and SMASH models, they are fixed to the values α=-124 MeV, β=70 MeV and γ=2 for UrQMD [70]. These values will be used for GiBUU and SMASH as well. They constitute a so called hard, momentum independent density dependent equation of state with a nuclear incompressibility of 380 MeV [71, 72]. For PHSD, only an incompressibility of 300 MeV is given. This makes the PHSD equation of state slightly softer than the UrQMD EoS.
Data collected with HADES strongly suggests that the Skyrme potential is needed to explain observables such as higher order flow harmonics in gold-gold collisions, as can be seen in the left panel of Fig. 3.2. [73, 74]. Additionally, transverse mass spectra of Kaons suggests that transport models with a potential describe the transverse mass spectra best, as shown in of Fig. 3.2 (right panel).

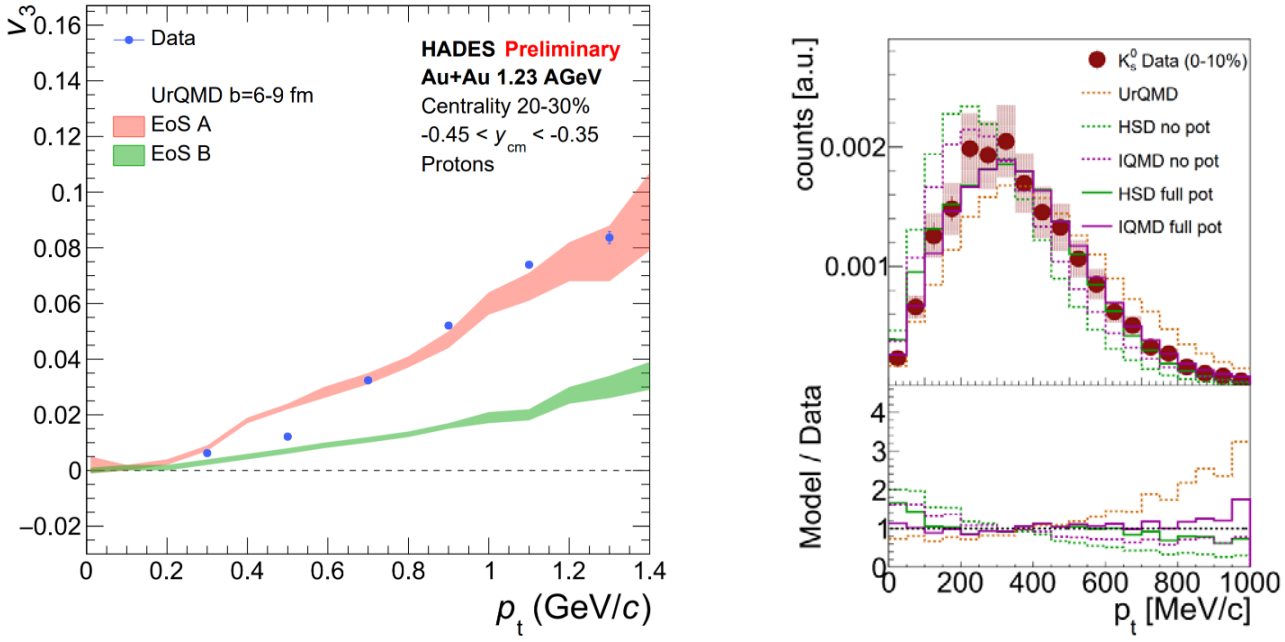

Figure 3.2: Left panel: Hades Data on the triangular flow of protons at 20 to 30% centrality compared to two Equations of State. The red one is the classical UrQMD equation of state [73].Right panel: The transverse momentum spectra of Kaons and Λ-baryons compared to different models and potentials. [75]

3.3.2 Coulomb potential

The Coulomb potential is the potential between two electrical charges. Coulomb's law was discovered by French physicist Charles de Coulomb in 1785 [76]. It states that the potential of two point charges is

$$V_C = \frac{1}{4\pi\epsilon_0}\frac{q_1 q_2}{r}. \tag{3.6}$$

Since a typical heavy nucleus has a high positive electric charge, the influence of the Coulomb force when colliding nuclei is considerable, especially regarding the range difference between the nuclear force (<3 fm) and the infinite range of the Coulomb force.

3.3.3 Yukawa potential

The Yukawa potential was introduced by Japanese theorist Hideki Yukawa in 1934 [7]. It is recognized to describe the interaction between light non-strange baryons via the exchange of a pion and can also be seen as a remnant interaction of the strongly interacting quarks within the baryons. In this sense, it can be likened to electromagnetic Van-der-Waals-forces between molecules. The Yukawa-potential is given by the formula

$$V_{Yu} = \pm g^2 \frac{e^{-\lambda r}}{r}, \tag{3.7}$$

which is a generalization of the Coulomb potential for a finite range $1/\lambda$. λ should be of the order of $1.4\,\text{fm}$, as this corresponds to the pion mass via

$$\frac{\hbar c}{1.4\,\text{fm}} \approx 140\,\text{MeV}. \tag{3.8}$$

3.4 Microscopic Transport Models

As has been mentioned before, microscopic transport models aim to give a full description of the spacetime evolution of a heavy-ion collision. Several transport models will be compared in this work. These models will be compared in the following sections. The input files can be found in the appendix for comparison.

3.4.1 The transport model UrQMD

Ultra-**r**elativistic **Q**uantum **M**olecular **D**ynamics (UrQMD) is a transport model first published in 1998 [77]. UrQMD extends the Quantum Molecular Dynamics(QMD) framework which can be used for heavy-ion reactions between 0.1 and $2A$ GeV to relativistic energies by using covariant dynamics and increases the number of available resonances and mesons drastically [77].
UrQMD uses the Hamiltonian equations of motion to propagate particles along their classical trajectories using the geometric collision criterion. If done correctly, this provides a solution to the Boltzmann equation. The most important difference to the other models compared in this work is the fact that UrQMD calculates particle densities by assuming Gaussian wave packets, which means single events can be processed if a potential is active. This is not the case for GiBUU, PHSD and SMASH. Moreover, no elementary particles are included in UrQMD, meaning it cannot produce dilepton spectra directly. Instead, the UrQMD shining approach has been developed, implementing dileptons into UrQMD by a time integration method. This method assumes a resonance will emit dileptons over its whole lifetime and integrates this yield [78]. The potential used for the UrQMD Hamiltonian consists of Coulomb, Yukawa and Skyrme potentials. For this work, UrQMD v3.4 has been used [77, 79].

3.4.2 The transport model GiBUU

GiBUU is an acronym for the "**Gi**eßen-**B**oltzman-**U**ehling-**U**hlenbeck" project. It aims to solve the Boltzmann-Uehling-Uhlenbeck equation numerically, providing a framework to simulate reactions from leptonic scattering up to heavy-ion reactions. Of the models presented here, this makes it one of the more versatile. There are several different equations of state implemented, Coulomb and Yukawa potentials can be additionally switched on or of. In GiBUU, several collisions are computed simultaneously with the same impact parameter. While the density is taken as the mean over all simultaneous collisions, the particles of each collision cannot interact with each other. This is known as the parallel ensemble scheme, in contrast to e.g. the full ensemble scheme, where particles from different ensembles can interact with each other. GiBUU is able to generate dilepton spectra [67, 80].
In this work, GiBUU was used in the version of 2017. GiBUU uses Pythia to compute particle interactions above 2 GeV for meson-baryon scattering and 2.6 GeV for baryon-baryon scattering [81].

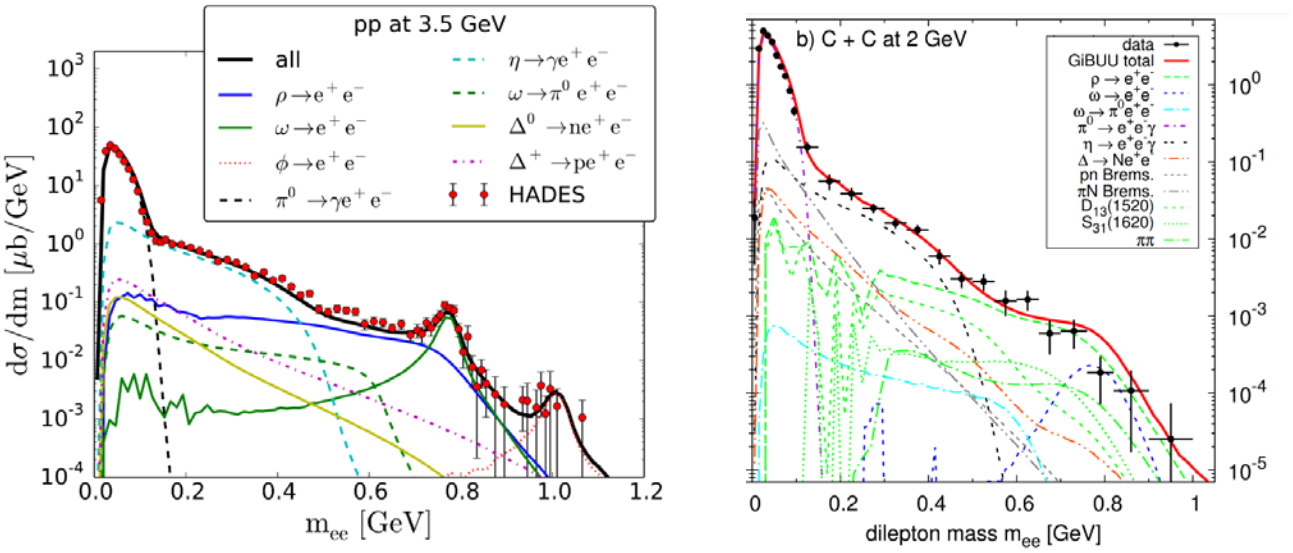

Figure 3.3: Left panel: Comparison of SMASH invariant mass spectra to HADES p+p data [84]. Right panel: Comparison of GiBUU invariant mass spectra to HADES C+C data [80].

3.4.3 The transport model SMASH

Simulating **M**any **A**ccelerated **S**trongly-interacting **H**adrons (SMASH) is a BUU-Code designed under the leadership of Prof. Hannah Elfner at FIAS [65]. In this work, SMASH v1.5.1 was used as it was preinstalled on the GSI systems. SMASH differs formally from the other models as it uses C++, while the other models are written in FORTRAN. SMASH uses a test particle ansatz to sample potentials and ensure locality. SMASH scales up the number of particles while also decreasing the interaction cross sections by the same factor [65]. This constitutes a full ensemble scheme, as compared to the parallel scheme used by GiBUU and PHSD. The particles of different ensembles can collide with each other. SMASH uses Pythia to compute the particle interactions [81].

3.4.4 The transport model PHSD

Parton-**H**adron-**S**tring-**D**ynamics (PHSD) is a successor of Hadron-String-Dynamics and extends it to higher energies, where partonic degress of freedom start to play a role. In principle, PHSD aims to solve the Kadanoff-Baym-equations. These are generalized transport equations for the greens functions. PHSD also includes gluonic and partonic interactions at high energies. PHSD incorporates only one medium soft equation of state with the typical Skyrme potential in Version 4.0 with a compressibility of $K = 300\,\text{MeV}$. In this sense, it lies between the super-soft equation of state of the cascade modes ($K = 0\,\text{MeV}$) and the hard Skyrme potential with $K = 380\,\text{MeV}$ and can be used as a cross check as the spectra are expected to lie between the two extremes. In this work, PHSD v4.0 was used in a patched form to produce coarse graining output [82, 83].

3.5 Comparison of model calculations to data

The models described in Sec. 3.4 have been used extensively for comparisons to experimental data from e.g. HADES for proton-proton, carbon-carbon, argon-potassium chloride and gold-gold collisions.
Because medium effects do not play a large role in very collision systems, most of the models reproduce the yield for elementary reactions and small nuclei well [80, 84, 85]. Fig. 3.3 shows agreement of SMASH (left panel) and GiBUU (right panel) data to elementary and small collision systems as measured by the HADES collaboration. Similar studies exist for the UrQMD and IQMD Shining approach. PHSD as well as its predecessor HSD also describes dilepton spectra from elementary collisions well [85].
Fig. 3.5 shows similar comparisons to data from ArKCl for SMASH, GiBUU and UrQMD. The models with vacuum spectral function seems to miss the yield in the low-mass region. This is due to medium effects. Their inclusion into the transport models has been attempted via collisional broadening [66], which can be seen in the right panel of Fig. 3.5. This seems to take care of some effects but it will be seen in Fig. 4.1, that collisional broadening overestimates the dilepton yield in the ρ-mass range for gold-gold collisions as well.
Another important point is the reproduction of hadron data, which will only be swiftly discussed. The right panel of Fig. 3.6 shows data from HADES compared to GiBUU, SMASH, PHSD and other models showing that the models systematically overestimate the pion yield. However, many other hadronic observables can be reproduced by the transport model. As an example, the left panel of Fig. 3.6 shows the transverse mass spectra of protons in gold-gold collisions measured by HADES, which are perfectly reproduced by UrQMD. Other examples are the flow observables as discussed in Section 3.3.1. However, a consistent model needs to reproduce all observables correctly, from dilepton yields, over hadron multiplicities to flow observables. It is clear now that a method needs to be used to take care of the medium modifications of the spectral function.

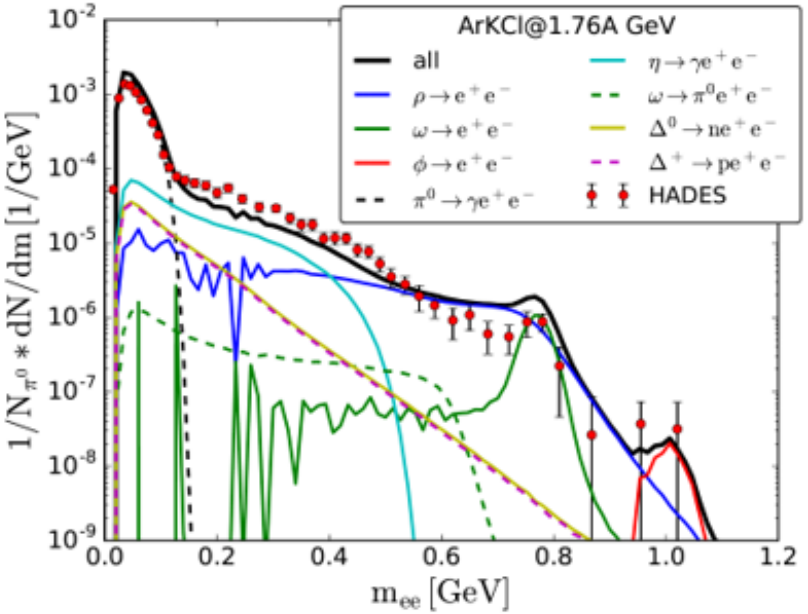

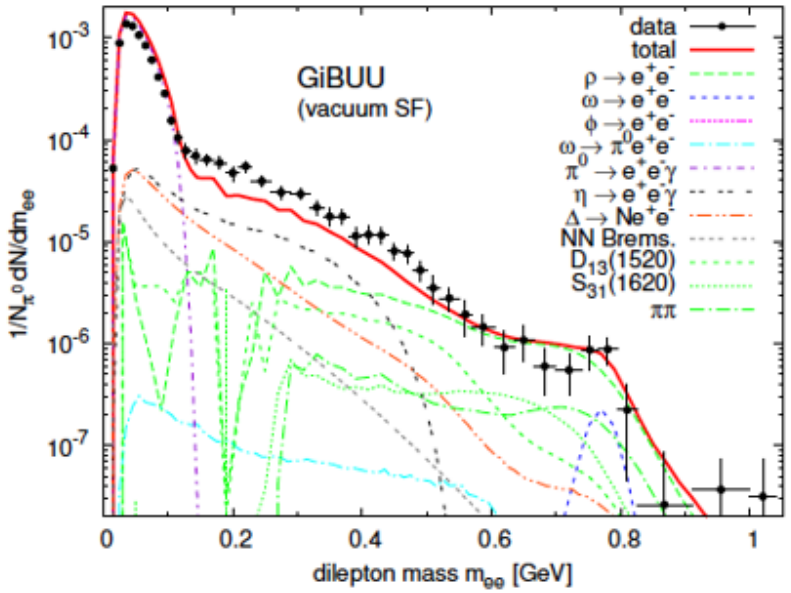

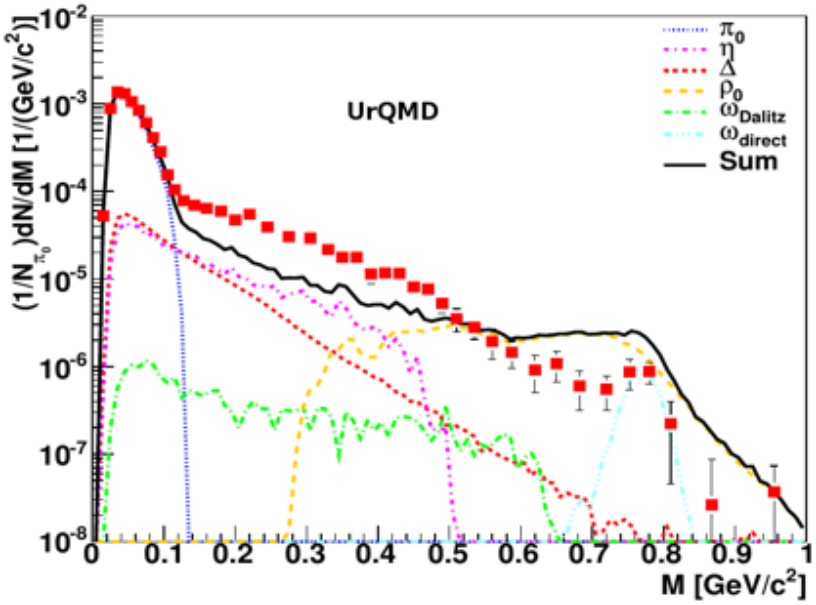

Figure 3.4: Left panel: ArKCl spectra compared to dilepton spectra calculated with SMASH (top left), GiBUU (top right) and the UrQMD shining approach (bottom) compared to HADES data. The dilepton yield is underestimated due to medium effects [84, 86, 87].

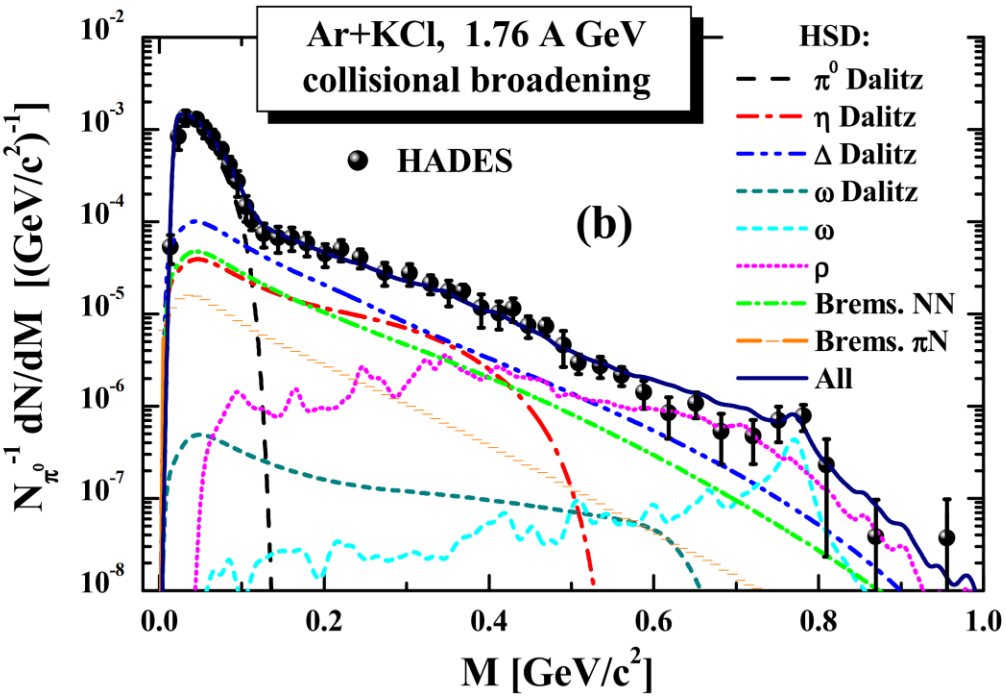

Figure 3.5: ArKCl spectrum in PHSD with collisional broadening compared to HADES data [85].

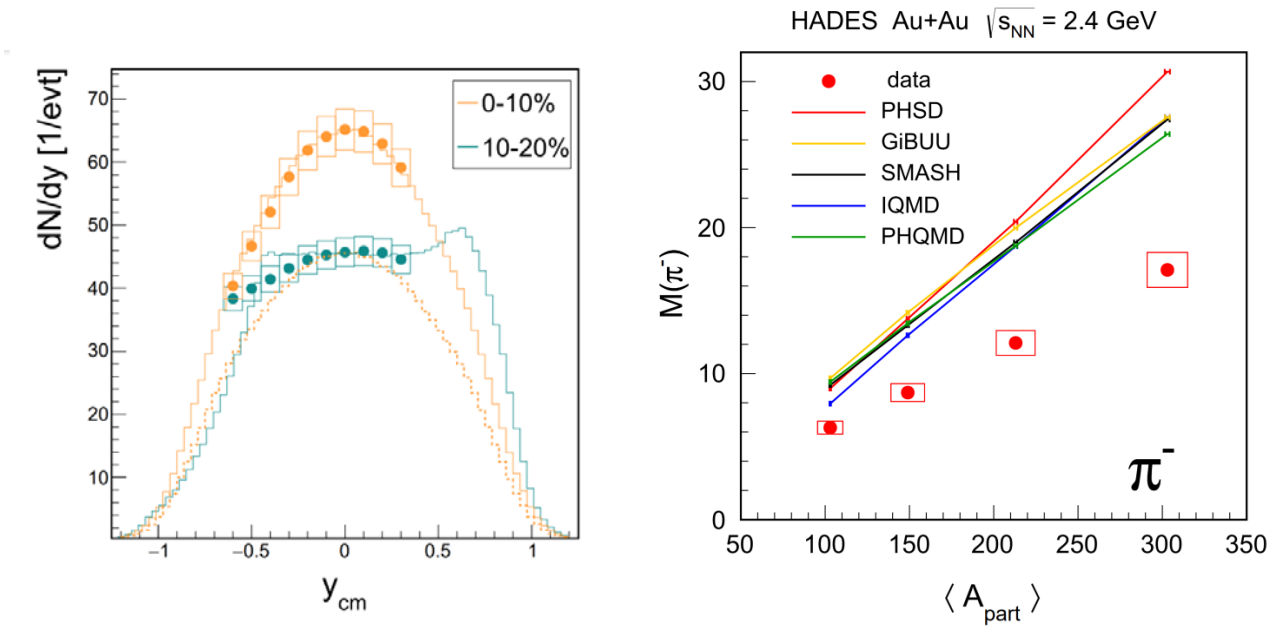

Figure 3.6: Left panel: The transverse mass spectra of protons are well described by UrQMD [88]. Right panel: Most models overestimate the pion yield as produced by the HADES collaboration in Au+Au collisions at 1.23A GeV [89].

4 Coarse graining approach

The coarse graining (CG) approach has proven itself successful in the analysis of dilepton spectra produced by HADES. In several instances it fits the models better than invariant mass spectra produced by transport calculations. Coarse graining has first been developed by Kapusta and Huovinen in 2002 [90]. The left panel of Fig. 4.1 shows coarse graining calculations compared to data from gold-gold collisions at 1.23A GeV taken by the HADES collaboration and spectra obtained by PHSD and SMASH. While PHSD and SMASH overestimate the ρ-peak drastically, the coarse grained models can describe it well. However, for very low masses, the coarse graining overestimates the dilepton yield, while HSD comes closer to data. An important point is the fact that coarse graining can be employed over a wide range of energies and collision systems. The smaller system of indium-indium collisions has been measured by the NA60 collaboration at CERN for energies of 158A GeV and is perfectly described by coarse graining calculations using the Rapp-Wambach spectral function, which can be seen in the right panel of Fig. 4.1.

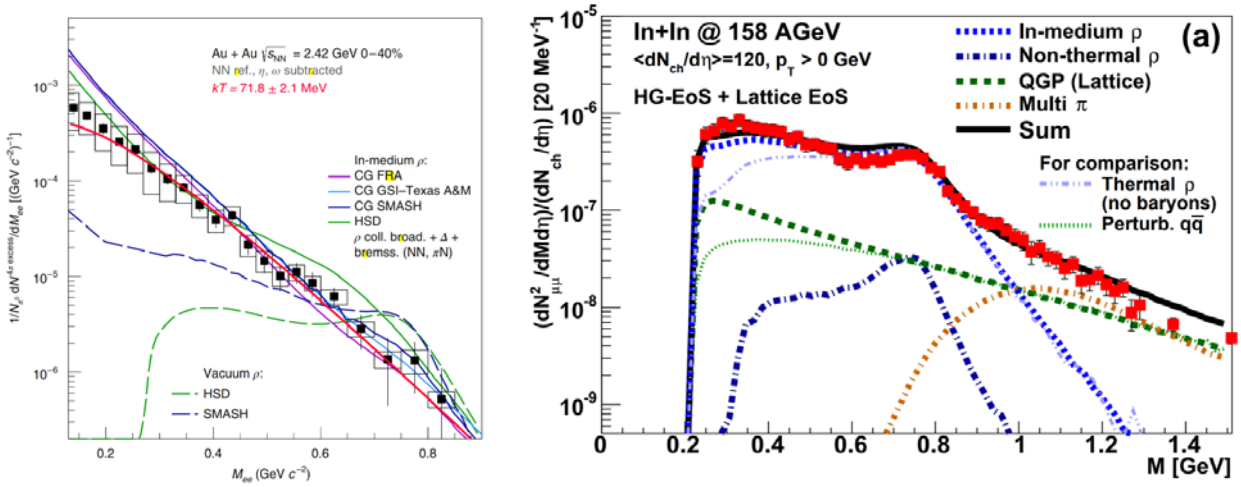

Figure 4.1: Left panel: Coarse graining calculations from different models compared to the dilepton invariant mass spectrum measured by HADES in Au+Au collisions at 1.23A GeV and transport calculations done using (P)HSD with collisional broadening. The dashed curves show the contribution from HSD and SMASH if the free spectral function is used [59]. Right panel: coarse graining calculation with the different contributions compared to NA60 data of Indium collisions at 158A GeV [91].

For the analysis, the C++ based software CERN ROOT has been used [92].
Coarse graining divides the 4-volume of a heavy-ion collision into small cells. The cell size is dependent on the collision energy, because higher collision energies generally probe higher resolutions. In this work, the duration of one cell is 0.5 fm/c, while the cells extend over 1 fm^3 in space. It has been checked that for

collision energies of a few GeV/u the choice of spacetime binning does not influence the resulting spectra (see Fig. 5.1).

4.1 Determination of effective baryon density

Coarse graining aims to extract bulk properties of matter from the output of transport calculations. A transport calculation's output consists of a defined position and momentum for each particle. However, in reality, the particles should rather be approximated by Gaussian wave packets than by point particles (see Fig. 4.2). Therefore the coordinates of a particle are seen as the maximum of a 3-dimensional Gaussian wave function of the form

$$P(\vec{x},\vec{x}_0) = \frac{1}{\sqrt{2\pi}^3 \sigma_x \sigma_y \sigma_z} e^{-\left(\frac{(x-x_0)^2}{2\sigma_x^2}+\frac{(y-y_0)^2}{2\sigma_y^2}+\frac{(z-z_0)^2}{2\sigma_z^2}\right)}, \tag{4.1}$$

where σ_i is 0.8 fm, which is the radius of a proton. It is easily seen that $P(x,x')d^3x$ is not a Lorentz invariant. Other parametrizations have been proposed, however, it has been found that they are rather inefficient as the variables x, y and z are not independent anymore, making a sampling of this function numerically straining [93]. Instead, the function $P(x,x')$ is contracted in the direction of the largest $\vec{\beta}$-component β_i by setting $\sigma_i \to \sigma_i \gamma(\beta_i)$.
This distribution is sampled with test particles 500 times to determine the fraction of a particle located in a specific spacetime cell. This automatically allows the determination of other quantities X like energy or momentum density for a cell at position (x,y,z) in a similar fashion as the sum of the fraction of each particle i multiplied by the according quantity X_i,

$$X(x,y,z) = \sum_i X_i \int_{V(x,y,z)} d^3r P_i(\vec{x},\vec{x}_0). \tag{4.2}$$

This is especially important to determine the net velocity of each cell. Since the dilepton rates are computed in the **l**ocal **r**est **f**rame (LRF), all observables need to be boosted to the LRF. For example, any density transforms as the cell volume is larger by a factor of γ in the LRF than for an observer at rest with respect to the laboratory frame.
In this thesis, the effective baryon density

$$\varrho_{eff} = \varrho_{nucl} + \varrho_{\overline{nucl}} + \frac{1}{2}(\varrho_{bar} + \varrho_{\overline{bar}}), \tag{4.3}$$

is used in the density determination, due to the fact that the ρ-meson couples as strongly to nucleons as to antinucleons, the coupling is symmetric for matter and antimatter and the effect of resonances is suppressed [38, 54].

4.2 Temperature determination

In this thesis, temperatures have been calculated with protons and pions employing two methods. A third method can be employed to check whether an obtained temperature reproduces transverse mass observables correctly. This can be expanded to other thermal observables, e.g. mean momenta or the mass spectra of hadron resonances.

4.2.1 System thermalization criteria

Before any temperatures can be extracted, the issue of thermalization needs to be addressed. In an earlier work, Seck and collaborators proposed to use the number of collisions each baryon has undergone to get information about thermalization [94]. They showed that the momentum spectra of particles with a collision number greater than 3 assume a Gaussian form as expected from thermal equilibrium (see Fig. 4.3.), in addition the widths of the momentum distributions σ_{p_i} have been compared for the condition

$$\sigma_{p_x} = \sigma_{p_y} = \sigma_{p_z}. \tag{4.4}$$

While this method works well for UrQMD, other models cannot define the number of thermalized cells in the same way. In GiBUU, the number of collisions is instead saved in a variable called generation g. For two scattering particles, the generation of the daughter particles g_d is given by

$$g_d = \max(g_{P_1}, g_{P_2}). \tag{4.5}$$

The maximum taken in Eq. (4.5) drives the number of collisions up faster and higher than for UrQMD. On the other hand, SMASH and PHSD produce comparably fewer collisions. For SMASH, this is due to the test particle ansatz used, for PHSD this is linked to the less stiff equation of state. In the first line of Tab. 4.1 the mean collision number of the particles is given for the last time step, respectively. Instead, a more empirical ansatz is employed in this work. A cell is only considered thermalized, if the pion density in it is bigger than a time dependent value,

$$\rho_\pi > \rho_\Pi \exp(-t/20), \tag{4.6}$$

where t is the time step, ρ_Π is a model dependent value, and 20 has been empirically determined as a normalization to reproduce the UrQMD thermalization. Moreover, the total number N_π of all pions from all simulated events with a fraction in the cell has to fulfill the similar property

$$N_\pi > N_0 \exp(-t/20), \tag{4.7}$$

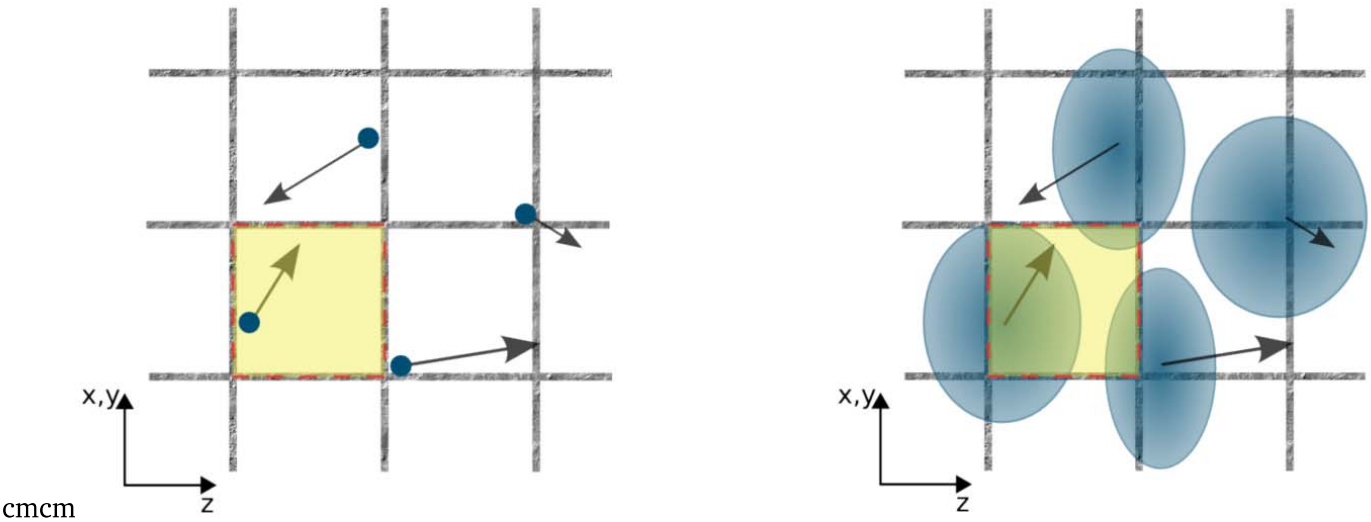

cmcm

Figure 4.2: Schematic illustration of the coarse graining process. The point particles are replaced by Gaussian wave packets, afterwards, an integration over each cell is performed.

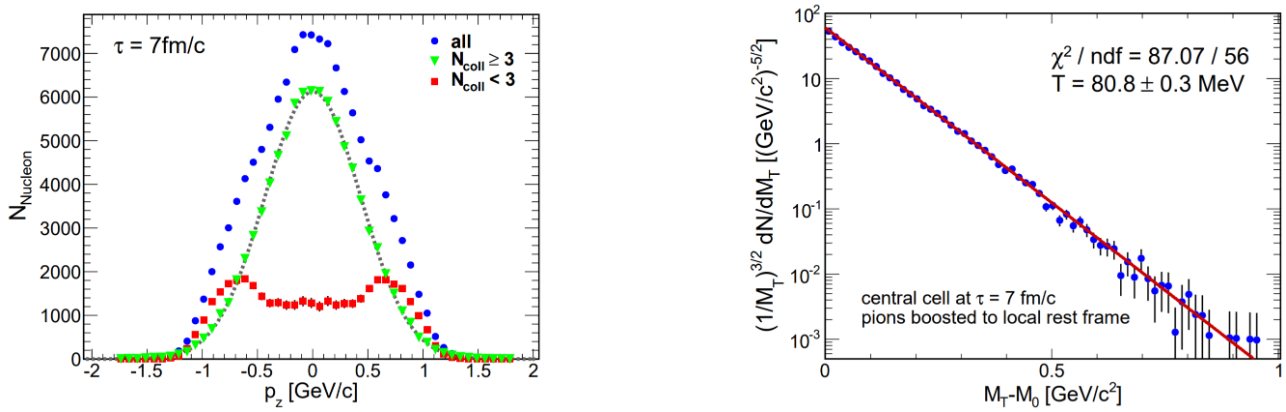

Figure 4.3: Left panel: The longitudinal momentum spectra of particles with more than three collisions assume a Gaussian form (grey dashed) in a cell [94]. Right panel: The m_t-spectra can be used to extract temperatures (the red line is an exponential fit) [94].

where N_0 is another model dependent parameter in the range of $N_\pi \approx 1.5 N_E$, where N_E is the total number of simulated events. The values for UrQMD have been chosen so that a large number of cells is thermalized while the mean temperatures gained with different determination methods stay similar. For the other models, the values have been chosen to approximate the total number of thermalized cells given by UrQMD. Values can be found in Tab. 4.1. The left panel of Fig. 5.7 shows the time dependence of the ratio of thermalized volume to the total grid volume. Summing all thermalized cells gives the total number N_{cells} in Tab. 4.1. More possibilities exist, for example comparisons between simulated observables and their analytic counterparts or the comparison of transverse and longitudinal momenta by employing the relaxation function as discussed in [91, 95]. The relaxation function $r(x)$ is defined as

$$\frac{3 g_0 x^{-\frac{1}{3}}}{2\pi^2}\left[1 + \frac{x \arctan\left(\sqrt{x-1}\right)}{\sqrt{x-1}}\right], \tag{4.8}$$

where g_0 is a degeneracy factor and $x = (\lambda_\perp/\lambda_\parallel)^2 \approx (p_\perp/p_\parallel)^{\frac{4}{3}}$ in the case of a momentum distribution of the form $f(p_\perp, p_\parallel) = g_0 \exp\left(-\sqrt{\frac{p_\perp}{\lambda_\perp} + \frac{p_\parallel}{\lambda_\parallel}}\right)$ [95, 96].

	UrQMD	GiBUU	SMASH	PHSD
n_{coll}	7	37	2	2
ρ_Π	0.001	0.04	0.03	0.0275
N_0	12000	18900	20000	13000
N_{cells}	108790	107992	105440	107532

Table 4.1: In the first line, the mean number of collisions (generations for GiBUU) is given per baryon. Values for the coefficients in Eq. (4.6) and 4.7 are found in the second and third line. In the last line, the number N_{cells} of all thermalized cells is given.

4.2.2 Fit to transverse mass spectra

Transverse mass spectra can be used to determine temperatures, due to the fact that the transverse mass

$$m_t = \sqrt{m^2 + p_t^2} \tag{4.9}$$

of a particle is invariant under boosts in the longitudinal direction due to its independence from the longitudinal momentum p_z. This provides an excellent framework for heavy-ion collisions, because large fractions of particles carry z-momenta from the initial colliding nuclei, which can distort temperature measurements.
The Boltzmann-approximation with temperature T

$$\frac{d^3N}{d\vec{p}} = \frac{d^3N}{dp_z p_t dp_t d\theta} \propto \exp(-E/T) \tag{4.10}$$

relates the momentum distribution of a particle to the temperature. By employing a change of variables from p_z to rapidity y and from $p_t dpt$ to $m_t dm_t$, integration over rapidity and azimuthal angle can be performed. This leads to the spectra having the form

$$\frac{dN}{dm_t} \propto 2\pi m_t^2 \cdot 2K_1\left(\frac{m_t}{T}\right). \tag{4.11}$$

A detailed derivation is given in the appendix of [54].
In the original thesis, an approximation has been made for large arguments of the Bessel function:

$$K_1(x) \xrightarrow[x \to \infty]{\sim} \sqrt{\frac{\pi}{2x}} e^{-x}. \tag{4.12}$$

This approximation will not be used in the following analysis, a detailed comparison can be found in the appendix. The advantage of this method is that it can be used with low numbers of events, since the fitting needs less statistics than other methods. However, due to the necessity of one one-dimensional histogram for each cell, the memory necessary increases with a decreasing cell size by a factor of 8. If high-energy collisions are analysed, smaller cell sizes are necessary to produce meaningful results as the dynamics are taking place on smaller scales. While this can be compensated by larger calculation times, this is unpractical.

4.2.3 Mean of the kinetic energy

According to Boltzmann statistics, the expectation value of the kinetic energy of an ensemble of particles is related to the temperature via

$$< E_{kin} >= \frac{\int_0^{\pi}\int_0^{2\pi}\sin(\theta)\int_0^{\infty} dpp^2(\sqrt{p^2+m^2}-m)e^{-\frac{-\sqrt{p^2+m^2}}{T}}}{\int_0^{\pi}\int_0^{2\pi}\sin(\theta)\int_0^{\infty} dpp^2 e^{-\frac{-\sqrt{p^2+m^2}}{T}}}. \tag{4.13}$$

The integration can be performed and an explicit result can be given using Bessel functions. Section 2.2.1 in [97] provides the full derivation, yielding

$$< E_{kin} >= \frac{m\left(K_4\left(\frac{m}{T}\right) - K_0\left(\frac{m}{T}\right)\right)}{2\left(K_3\left(\frac{m}{T}\right) - K_1\left(\frac{m}{T}\right)\right)} - m. \tag{4.14}$$

This value reproduces the classical and ultra-relativistic limits of the mean kinetic energy of an ideal gas,

$$< E_{kin} >= \frac{3}{2}T \quad \text{for the classical limit,} \tag{4.15}$$

$$< E_{kin} >= 3T \quad \text{for the limit } m \to 0. \tag{4.16}$$

While in the proposal, a polynomial has been used to retrieve the inverse function, due to the fact that analytical inversion is not possible, a numerical inversion is used now [97].
This method's main advantage is also its biggest disadvantage. It relies on high statistics to obtain the temperature from a single value. However, since only one value is needed for every cell, this method does not strain computational resources as much in contrast to the fit method, taking around 150 values per cell. This makes this method better suited for very small cell sizes (<0.5 fm) in the case high-energy collisions or small systems.

4.2.4 Mean transverse mass

Just like the mean kinetic energy, the transverse mass can be calculated according to Boltzmann statistics if quantum mechanical effects are neglected. A derivation can be found in Section 7.1. The transverse mass can be used to calculate the temperature. However, the comparison of thermal expectation values with their simulated counterparts might prove useful in developing a more matured thermalization model.
The mean transverse mass in thermal equilibrium is given as

$$\langle m_t \rangle_T = \frac{T}{\mathcal{N}(m,T)} \left[-\pi m \boldsymbol{L}_1 \left(\frac{m}{T}\right) \Phi(m,T) + \pi m T \boldsymbol{L}_0 \left(\frac{m}{T}\right) \Omega(m,T) + \Sigma(m,T)) \right] + \frac{m}{2}, \tag{4.17}$$

where: (4.18)

$$\mathcal{N}(m,T) = m^3 \left[K_1\left(\frac{m}{T}\right) - K_3\left(\frac{m}{T}\right) \right], \tag{4.19}$$

$$\Phi(m,T) = \left(m^2 + 6T^2\right) K_0\left(\frac{m}{T}\right) + m \left[2T K_1\left(\frac{m}{T}\right) - m K_2\left(\frac{m}{T}\right) \right], \tag{4.20}$$

$$\Omega(m,T) = m K_0\left(\frac{m}{T}\right) - 4T K_1\left(\frac{m}{T}\right) - m K_2\left(\frac{m}{T}\right), \tag{4.21}$$

$$\Sigma(m,T) = 2m^3 K_2\left(\frac{m}{T}\right) + 4m^2 T K_1\left(\frac{m}{T}\right) + 6\pi T^3. \tag{4.22}$$

Therefore, it is possible to compare the simulated transverse mass to a value obtained analytically by calculating the temperature of the system. Just like in the case of the mean kinetic energy, this can show the road to a thermalization criterion completely independent of all model-dependent parameters.

4.2.5 Temperature determination using nucleons

The methods discussed above for pions can be expanded to any particle species. At SIS energies, nucleons are the obvious candidates. The main advantage is their abundance. A large sample is needed in the case of temperature determination with pions as the pion density is rather low ($\sim$ 16 π/collision). If temperature determination with protons were possible, a lower number of events could be used to calculate the temperature, in turn decreasing the number of events needed for coarse graining. However, protons have the large disadvantage of being heavy particles with a high flow sensitivity, heavily influencing their momentum spectra. Moreover, protons also have an additional disadvantage when compared to pions -

they carry significant momentum in beam-direction, which drives up the temperatures in the initial phases of the collisions. In this work, the approach was to account for this by removing protons with a velocity higher than 0.65 c from the spectra.

4.3 Specifics of Simulations

In this work, UrQMD, GiBUU, SMASH and PHSD are compared. The chosen input parameters are seen in Tab. 4.2. The impact parameters have been calculated by using the Glauber model [98–100].

Model	Nuclei	N_{event}	Energy [A GeV]	Centrality	b [fm]	Potential
UrQMD v3.4	^{197}Au	10×1,000	1.23	0-10 %	0-4.7	cascade
UrQMD v3.4	^{197}Au	10×1,000	1.23	0-10 %	0-4.7	Skyrme
SMASH v1.5.1	^{197}Au	500×20	1.23	0-10 %	0-4.7	Skyrme
GiBUU v2017	^{197}Au	100×100	1.23	0-10 %	0-4.7	Skyrme
PHSD v4.0	^{197}Au	67×150	1.23	0-10 %	0-4.7	Skyrme
UrQMD v3.4	^{109}Ag	10×1,000	1.23	0-10 %	0-3.9	Skyrme
UrQMD v3.4	^{109}Ag	10×1,000	1.58	0-10 %	0-3.9	Skyrme
UrQMD v3.4	^{197}Au	10×1,000	1.58	0-50 %	0-10.4	Skyrme

Table 4.2: Dilepton yields, pion multiplicities, lifetimes and temperatures obtained from the dilepton spectra of the corresponding systems.

5 Results

It has been already shown in an earlier work that the cell sizes for coarse graining do not influence the result in any meaningful way, confirmed by the dilepton spectra in Fig. 5.1.
This is of course only true within reasonable boundaries (not so small as to lose a significant amount

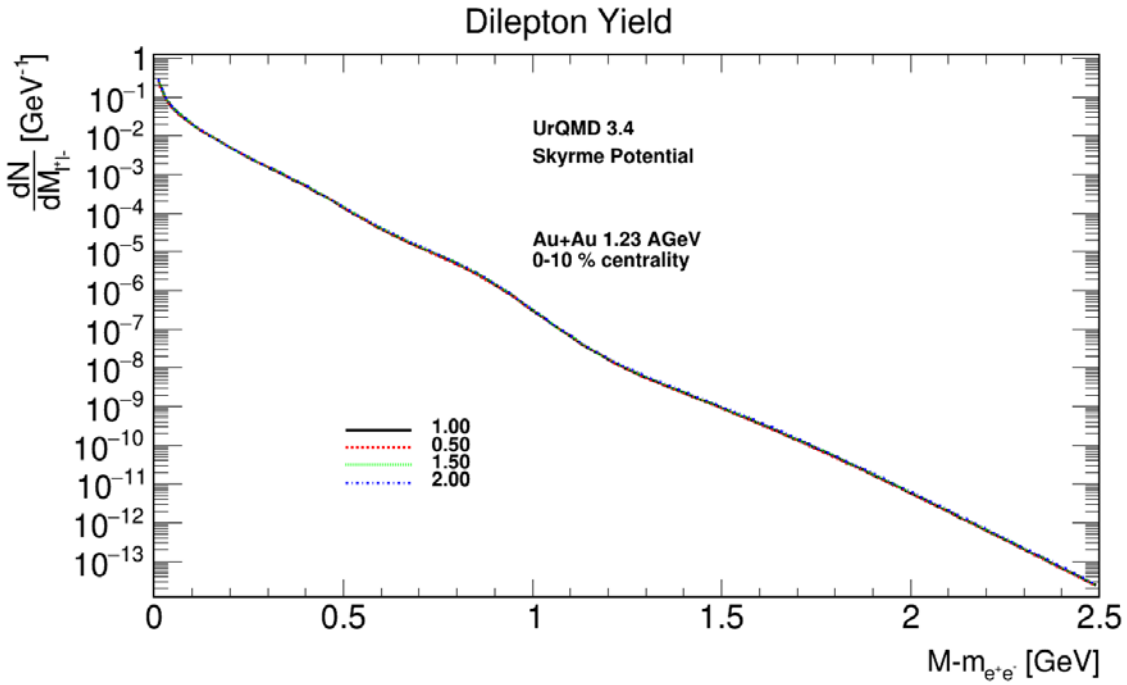

Figure 5.1: The invariant mass spectra calculated in [97] compared for different cell sizes. These are equal, showing independence of the arbitrarily chosen cellsize.

of statistics and not so large that the same cells include large contributions of both thermalized and unthermalized matter). The coarse graining procedure will now be applied to compare different methods of temperature determination, different models, as well as the Skyrme and cascade potentials of UrQMD. Moreover different collision systems will be examined regarding their dilepton and pion yield to produce predictions for the Ag+Ag beamtime of HADES at 1.23A GeV and 1.58A GeV.

5.1 Reproduction of earlier works

In an earlier work, Seck et al. produced spectra for the UrQMD cascade mode (no potential) at 1.23A GeV for 0-10 % centrality [94]. This work successfully reproduced these spectra for the low mass range, which can be seen in Fig. 5.2. For the intermediate mass range, there are deviations of the order of 20 %, however, these can be explained by a slight temperature difference in a small number of cells due to the exponential scaling.

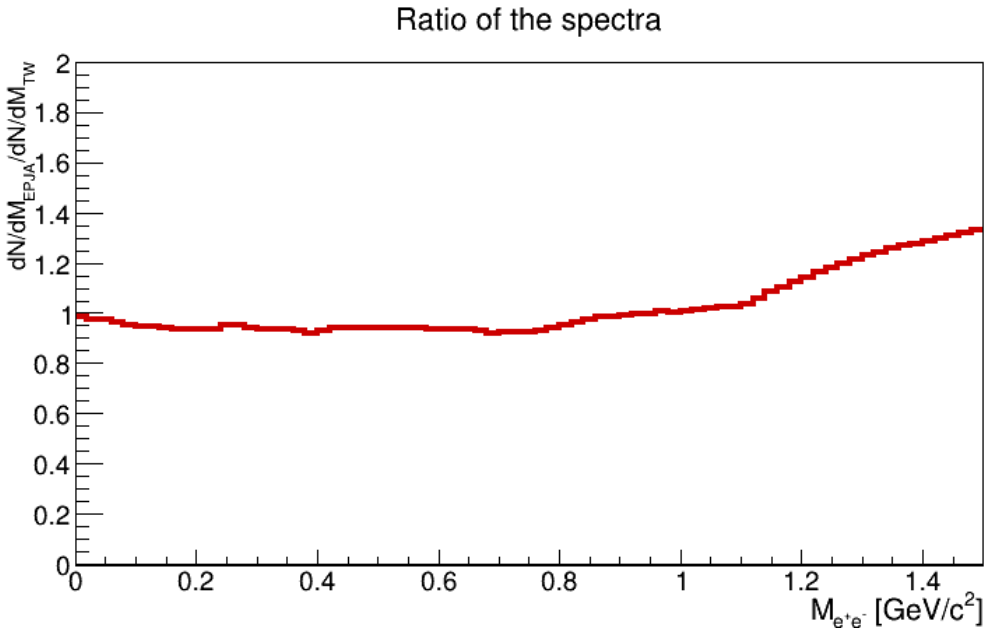

Figure 5.2: The ratio of the spectra calculated in [94] (EPJA) and this work (TW) in the mass range from 0 to 1.5 GeV/c^2.

5.2 Comparison of temperature determination methods

It is important to note that the method of thermalization employed in this work is not motivated by physical principles and needs to be improved in the future. However, for the temperature determination with pions as well as the fit to the transverse mass with nucleons yield very similar results for UrQMD (see left panel of Fig. 5.3), which can also be seen in the ratios of the invariant mass spectra in the right panel (black solid curve versus red dotted-dashed and green dashed). Fig. 5.4 shows results obtained for all transport models. In the top row results from GiBUU are shown, in the middle row, results for SMASH and in the bottom row, results for PHSD are displayed. The similarities are consistent with thermal equilibrium, as a system in local thermal equilibrium should yield the same temperature for different methods of obtaining a temperature. For all models, the kinetic energy of protons (in particular) does not provide temperatures comparable to the ones extracted using pions. In the future, a more distinguished algorithm might be needed to reject protons with a significant fraction of the initial beam momentum.
For all models, the different methods of temperature determination yield diverging results, however, the temperatures of the protons in the late stages of the collision are consistently lower than the temperatures

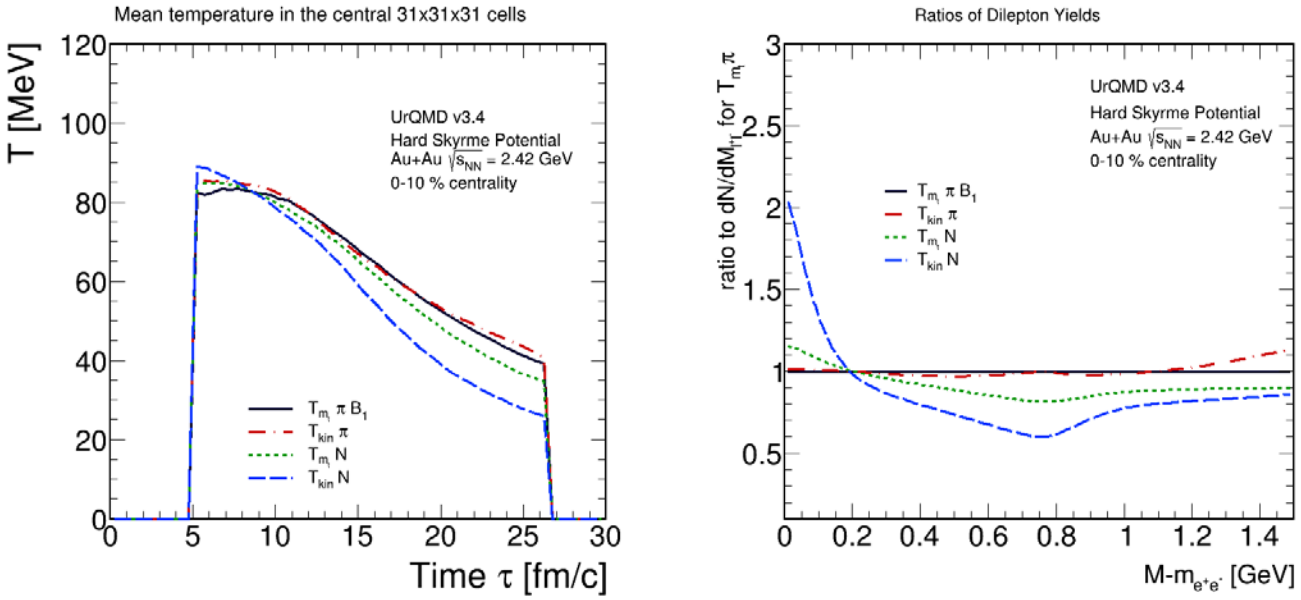

Figure 5.3: Left panel: Comparison of the temperature determination methods for UrQMD. For transverse mass fits to protons and pions, as well as the kinetic energy of the pions, the temperatures yield a similar result. Right panel: The similar results for the temperatures can also be seen in the deviations of the invariant mass spectra which are below 20 %. The kinetic energy of protons is too high.

of the pions, which in turn are consistent with each other. All models generate a 'kink' structure in the invariant mass spectrum of the T_{kin}^{N} around 0.8 GeV, most prominently for PHSD. Further investigations are needed as to whether this is a physical effect or a problem of the proton rejection criterion. However, for the rest of this work, the temperature of the fit to transverse mass spectra of pions with a modified Bessel function of second kind will be used.

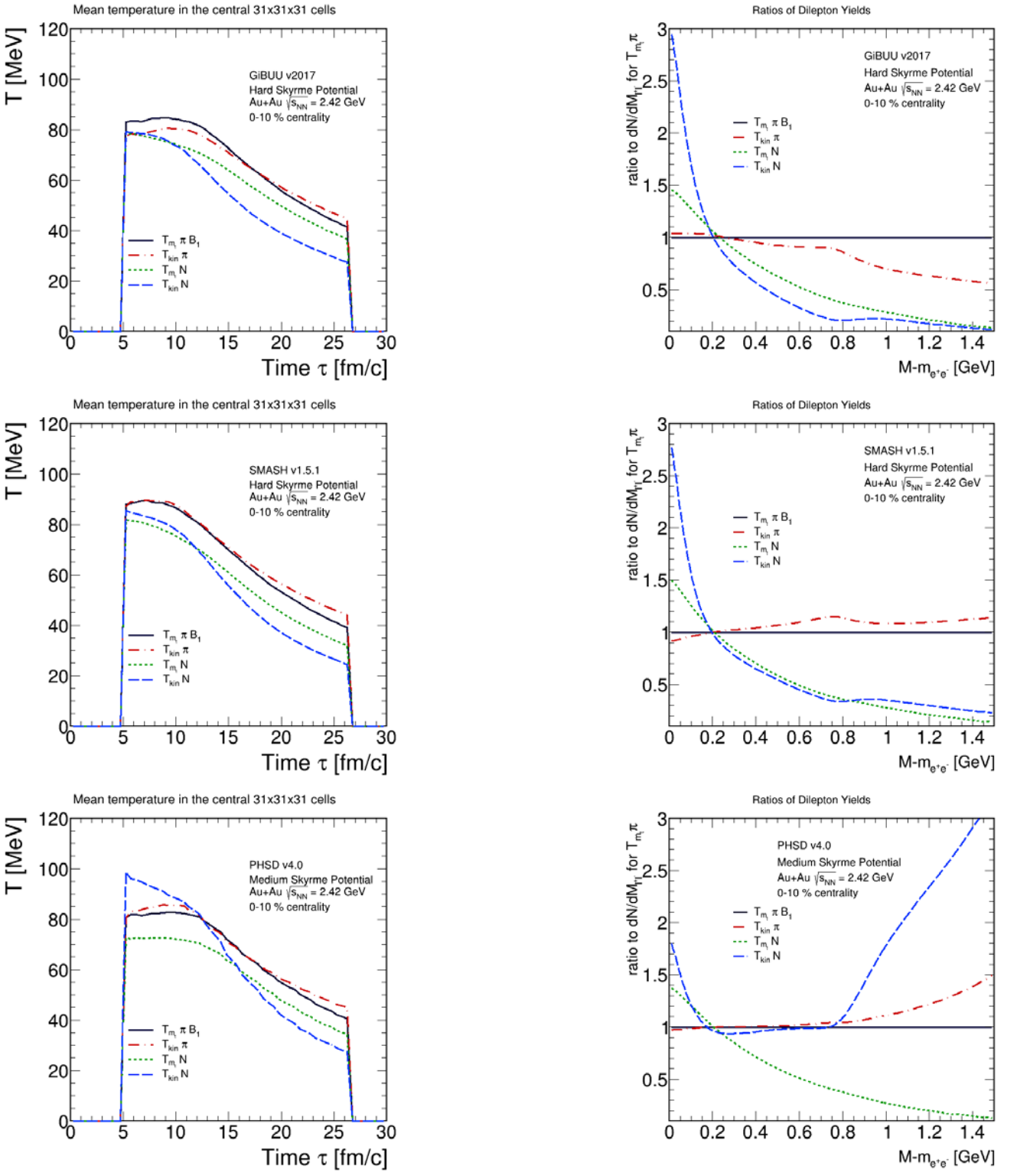

Figure 5.4: Left Line: Comparison of the different ways of temperature determination for the different models. Right Line: Ratio of the spectra produced with each model and temperature. Baseline is the temperature with a fit to transverse mass spectra. Top row: GiBUU, middle row: SMASH, bottom row: PHSD.

5.3 Comparison of the four models

Analysing the output of the four model calculations UrQMD, SMASH, GiBUU and PHSD, the first thing that meets the eye is the different number of particles produced in similar collisions. While in UrQMD, 38 mesons are produced in each collision, SMASH produces 48, GiBUU produces 61 and PHSD 64. This suggests different parametrizations of cross sections are used in each model, however, it has to be noted that UrQMD does not include elementary particles, meaning the lower particle numbers of this model can be partly explained by the absence of leptons and photons. Moreover, the number of collisions differs vastly as discussed in Section 4.2.1 (see left panel of Fig. 5.5). The transverse momenta are seen in the right panel of Fig. 5.5. They behave similarly for the three models with the hard Skyrme potential. The softer PHSD potential translates to lower transverse momenta. The left panel of Fig.5.6 shows the longitudinal momenta. While PHSD produces very high longitudinal momenta, SMASH and UrQMD mostly agree. The longitudinal momenta of GiBUU are very low, even in the same order of magnitude as the transverse momenta. With these momenta, the relaxation function $r(x)$ as defined in Eq. (4.8) can be computed. It is a measure for the percentage of the non-thermalized contribution to the energy density for all models. The comparison seen in the right panel of Fig. 5.6 indicates a thermalization after approximately 7 fm/c. GiBUU thermalizes earlier in this framework, as expected from the comparison of the momenta. PHSD takes the longest to thermalize, due to the lower transverse and higher longitudinal momenta. Expected from the similarity of the momentum evolutions for SMASH and UrQMD, they thermalize at the same time. Consider Fig. 5.7, showing the thermalized volume for the thermalization criterion using collisions in the left panel and the thermalization criterion for pion densities in the right panel. As can be clearly seen, the number of collisions does not yield satisfying thermalization results. Comparing the four models would need a similar number of thermalized cells to exclude effects purely from the differing volume of the fireball. While the number of thermalized cells with the empirical approach discussed in Section 4.2.1 yields very similar results even with the vastly differing pion production in each model, the number of collisions does not seem to be an adequate tool for now.
Fig. 5.8 shows the baryon and pion density in the central cells. The baryon density (left panel) is similar for the three models with the same equation of state, GiBUU, UrQMD and SMASH. When the nuclei fully overlap, the densities reach a maximum of $\sim 2.2\varrho_0$ and stay at this value until approximately 10 fm/c. Afterwards, they drop smoothly to $1\varrho_0$ at 20 fm/c, before the nuclear medium dissolves in the later stages of the collision. Because the PHSD equation of state is softer than the UrQMD equation of state, the densities PHSD reaches are larger than for the other models.
Comparing the pion densities (right panel of Fig. 5.8) in the central cells, PHSD produces a yield twice as large as the other models.

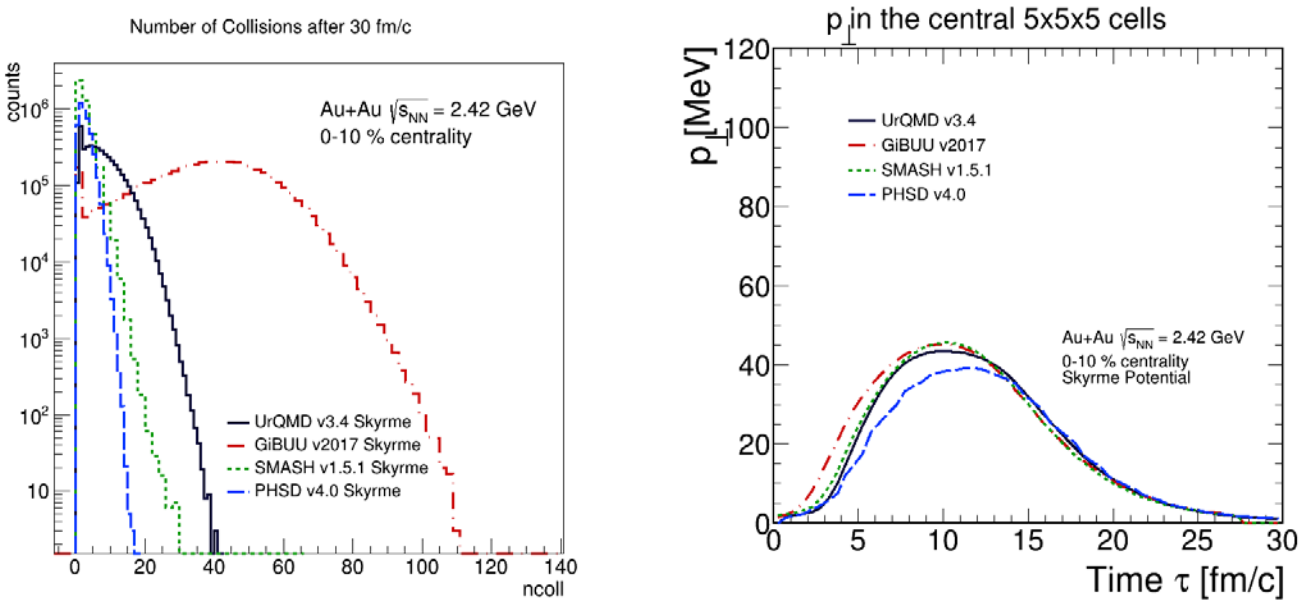

Figure 5.5: Left panel: Comparison of collision numbers (in case of GiBUU generation) of the different models. Right panel: Comparison of the transverse momenta in the central 5x5x5 cells.

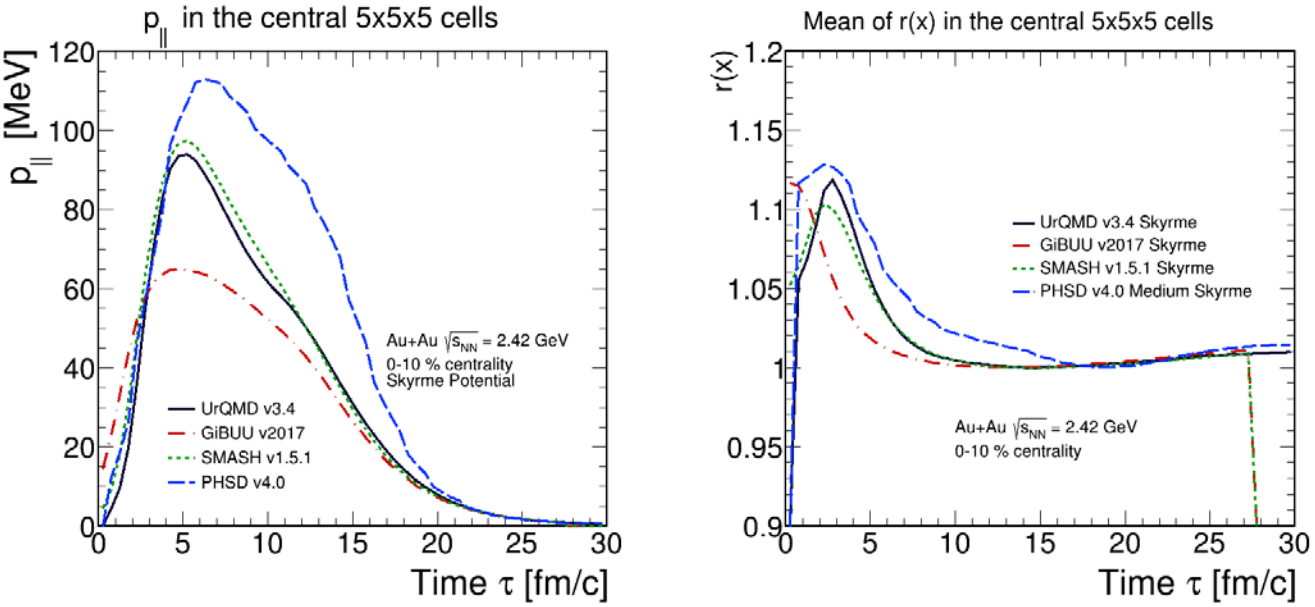

Figure 5.6: Left panel: Comparison of longitudinal momenta in the central 5x5x5 cells. Right panel: Comparison of the relaxation function in the central 5x5x5 cells.

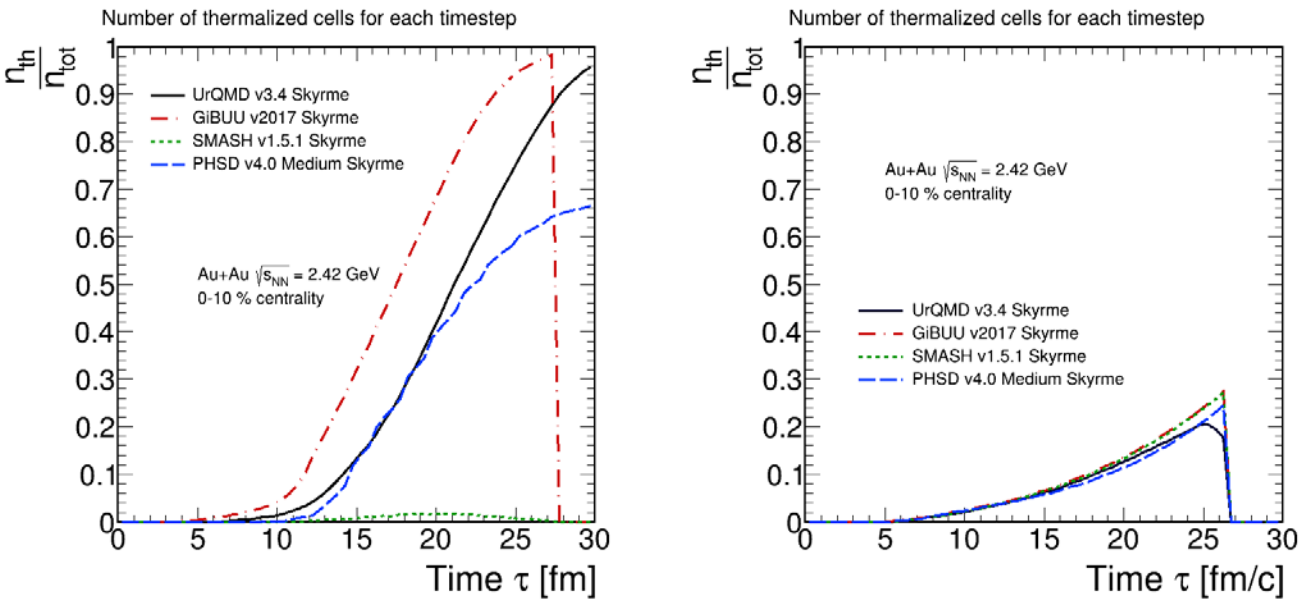

Figure 5.7: Left panel: Comparison of the percentage of thermalized cells for the different models. Thermalization is achieved if more than half of the baryons in a cell have experienced three or more scatterings. Right panel: thermalization according to the criterion discussed in Section 4.2.1.

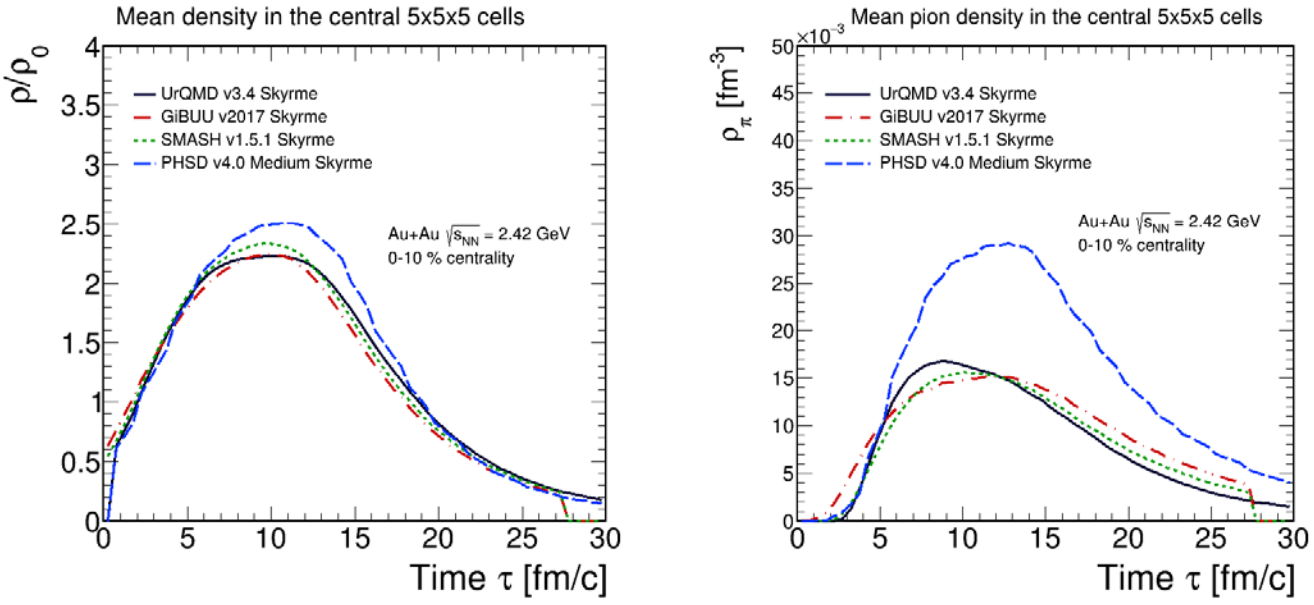

Figure 5.8: Left panel: Comparison of the effective baryon density for the four models in the central 5x5x5 cells, normalized to nuclear ground state density. Right panel: Comparison of the pion densities for the four models in the central 5x5x5 cells.

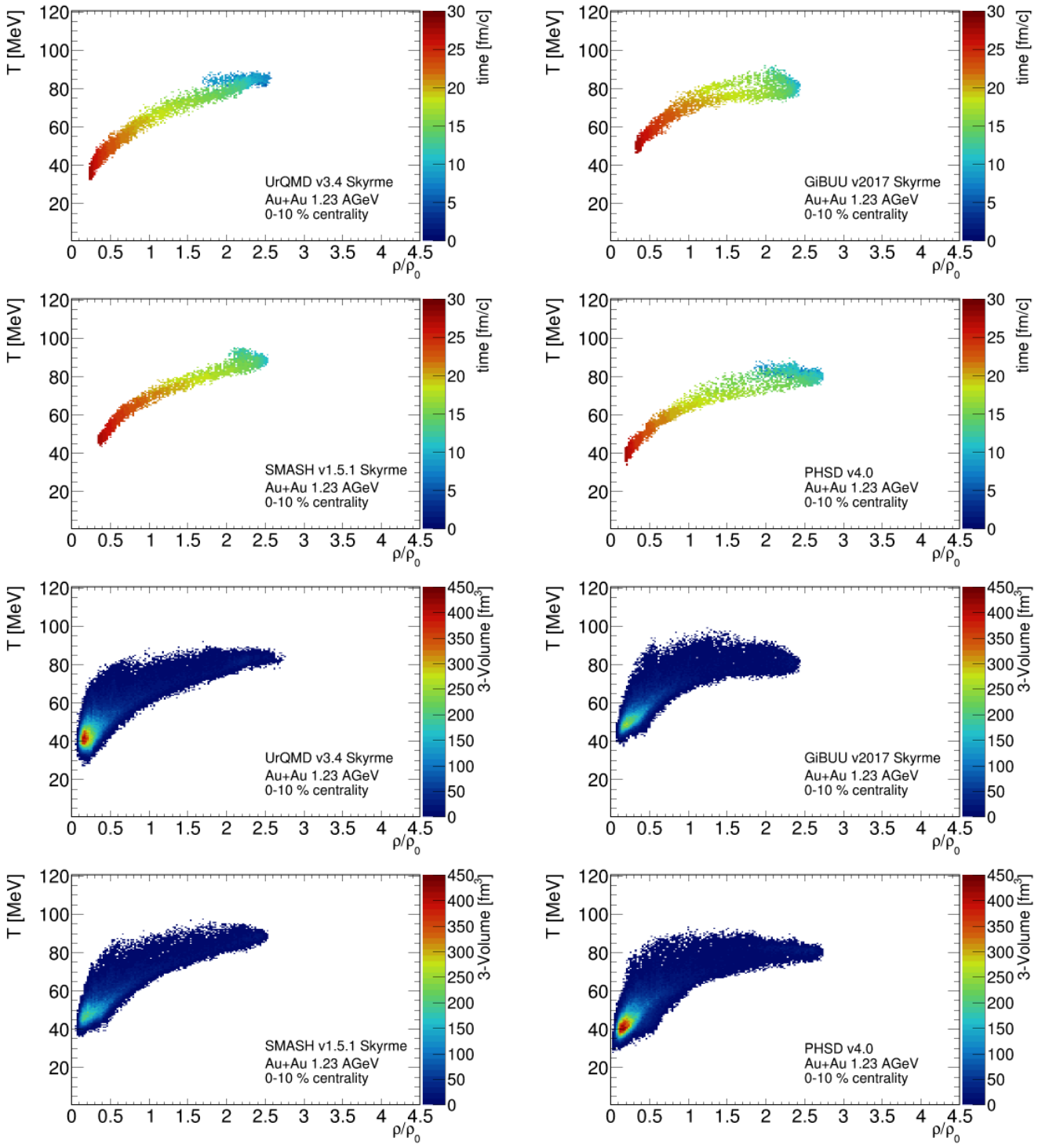

Figure 5.9: Phase space distribution of the thermalized cells in the collision volume. In the upper four figures, the central 5x5x5 cells are followed on their trajectory through the ρ-T-plane, where color indicates time. In the lower four figures, the total number of cells of a certain ρ and T contributing to the spectrum is shown.

model	HADES	UrQMD	GiBUU	SMASH	PHSD
M(π)	40±2.8	39.5	58.1	48.5	64.8
$N^{\pm}_{\|y\|<0.5}$	14.9±0.8	13.9	21.5	16.9	22.5

Table 5.1: Pion yields for different models and the HADES experiment for Au+Au at $\sqrt{s_{NN}} = 2.42$ GeV at 0-10 % centrality. M(π) is the total multiplicity of pions, $N^{\pm}_{|y|<0.5}$ is the number of charged pions in the $|y| < 0.5$ rapidity range.

As shown in Sec. 2.6.1, this influences the dilepton spectra significantly via the inclusion of the fugacity factor. At $\tau \sim 7$ fm, the pion density in UrQMD reaches a maximum which is by $\sim 20\,\%$ higher than in SMASH and GiBUU, which in turn produce similar densities, however, the pion density decreases slower for the latter. This is important as the fugacity factor of the pion chemical potential will enhance the dilepton yield of cells with high pion densities. Comparing the baryon and pion densities directly, this is expected to yield a more defined ρ-meson peak for GiBUU and SMASH as compared to UrQMD, as cooler and less dens cells contribute a higher amount to the spectra.
The pion yields after 30 fm/c differ drastically for the models, which can be seen in Tab. 5.1. Additionally included are results obtained by the HADES collaboration on pion production [89]. The HADES collaboration has measured a factor of up to ~ 2 fewer pions than predicted by five different transport model calculations, however, UrQMD is not included in their comparison. As a matter of fact, UrQMD reproduces the HADES pion yield with a factor of $1/2$ missing in the Δ-nucleon absorption cross section (see Fig. 3.6). The UrQMD authors are currently investigating this behaviour.The temperatures produced by each model as seen in the left panel of Fig. 5.10 differ on a wider range than the baryon densities. SMASH, PHSD and UrQMD yield similar temperatures of the transverse mass fit in the initial phases of the collision, however, the GiBUU and PHSD temperature take a slightly longer time to cool down. The SMASH temperature is initially 10 MeV higher than the other temperatures, but decreases faster and coincides with the GiBUU temperature after 13 fm/c. The right panel of Fig. 5.10 shows the simulated transverse masses. They do not show the same qualitative behaviour and differences as the temperature profiles. Further investigations would be needed to explain this behaviour.

In Fig. 5.9, the phase space evolution of the four models is summarized. In the first four figures, the position of the central cells 5x5x5 is seen, where color indicates time of the evolution (τ). In the latter four figures, the whole volume of the collision is seen, where color indicates the 3-volume at this temperature and density integrated over the duration of the collision.
In all models, a large part of the cells can be found at a temperature of around 40 MeV and a density between 0.1 and 0.2 ρ_0. While there is a rather clean cut for the UrQMD temperatures at around 80 MeV, cells of the other models can reach up to 100 MeV, however, this is limited to the corona of the collision area and points to the need for a better thermalization criterion than the one employed here.
In conjunction, this leads to the invariant mass spectra and ratios shown in Fig. 5.11. Taking the center regions, the spectra produced by UrQMD and GiBUU show similarities and lie within 20 % of one another, which is the current experimental precision HADES can reach [89]. The SMASH invariant mass spectrum shows only small deviations from GiBUU and UrQMD in the low mass range of $\sim 20\,\%$, but due to the higher temperatures it reaches (compare Fig. 5.10 or the upper four panels in 5.9), there is a divergence from the other two models in the intermediate mass range at the point of the ρ-peak. This is natural as the temperature enters the spectra exponentially, making the region above 1 GeV very sensitive to temperature differences [94].
The PHSD spectrum, which suffers from its overwhelming pion production, is larger than the spectra of the other models by a factor of two. The yields of UrQMD, SMASH and GiBUU are similar, the PHSD

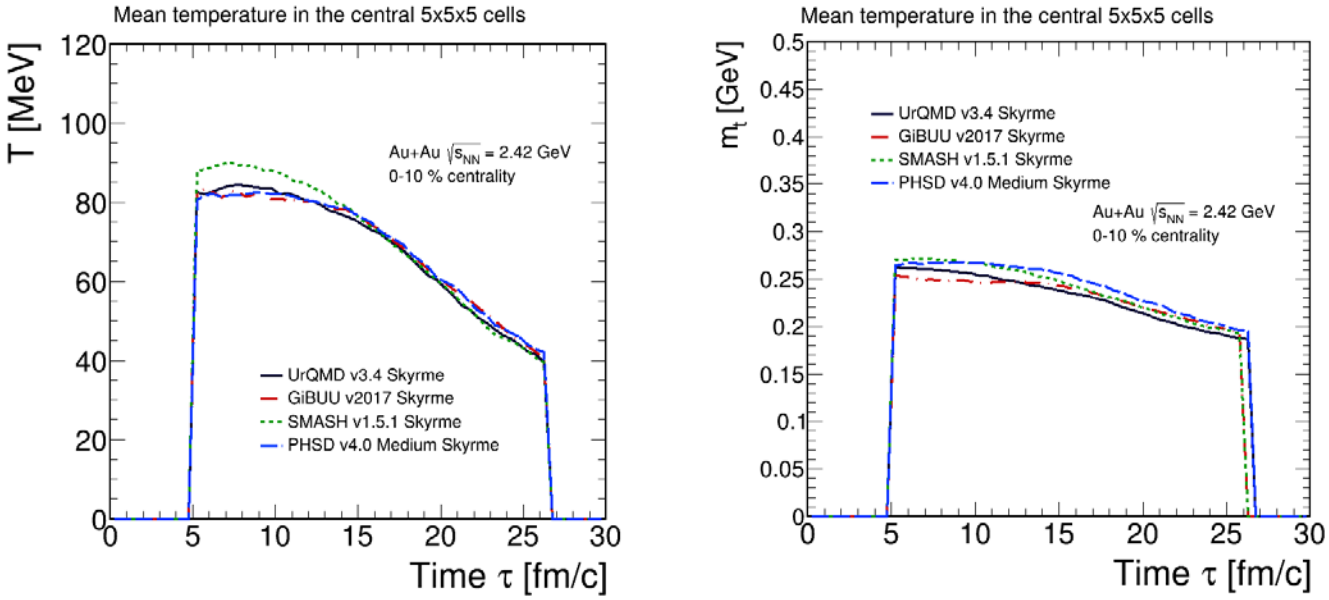

Figure 5.10: Left panel: The temperatures produced by the different models in the central 5x5x5 cells. Right panel: Transverse pion masses in the central 5x5x5 cells for different models.

yield is twice as high, as can be seen in Tab. 5.2. Considering the cells further removed from the center of the collision, hot cells with low densities dominate the spectrum and produce a visible remnant of the ρ-meson-peak in contrast to the UrQMD spectrum, which is clearly seen in the right panel of Fig. 5.12. This is absolutely comprehensible as the chiral condensate decreases stronger with density than with

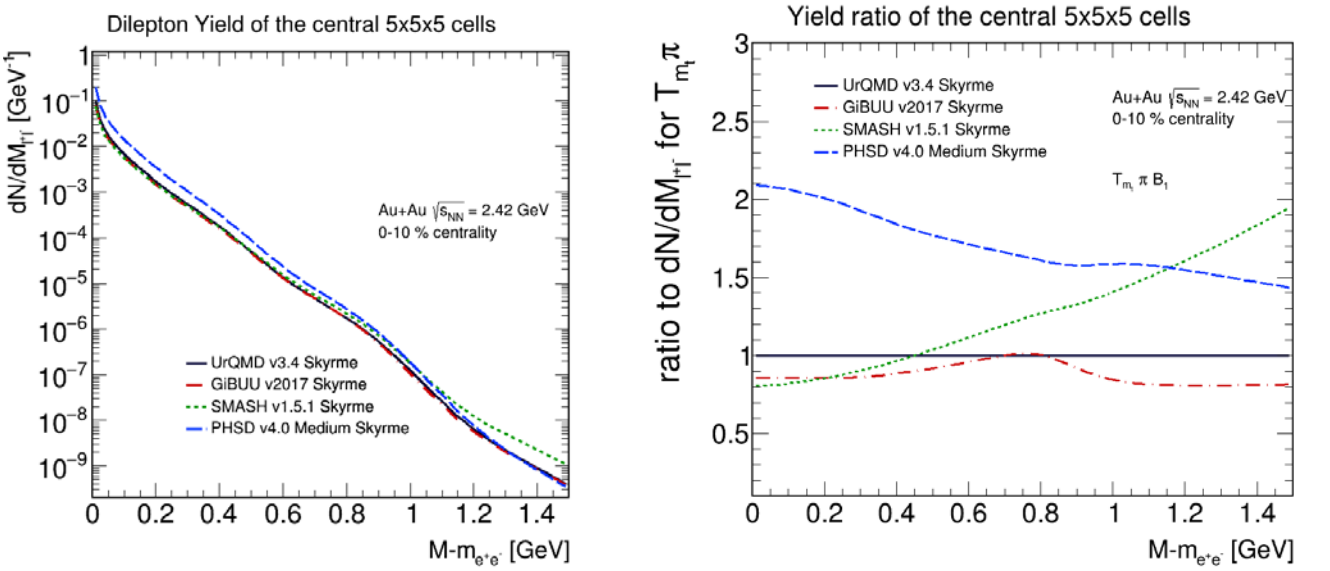

Figure 5.11: Left panel: Invariant mass spectra for the different models calculated with coarse graining. Right panel: Ratios of the dilepton spectra.

model	HADES	UrQMD	GiBUU	SMASH	PHSD
e^+e^- yield 5x5x5	–	4.69×10^{-5}	4.14×10^{-5}	4.48×10^{-5}	8.74×10^{-5}
e^+e^- yield full volume	$(2.3\pm0.5)\times10^{-4}$	2.9×10^{-4}	3.7×10^{-4}	3×10^{-4}	4.7×10^{-4}
τ [fm/c]	19.3 ± 4.3	26.1	22	22.1	26.7

Table 5.2: Dilepton yields for different models and the HADES experiment for Au+Au at $\sqrt{s_{NN}} = 2.42$ GeV at 0-10 % centrality in the central 5x5x5 cells and the full yield. The full HADES yield from [89] scales according to $A_{\text{part}}^{1.33}$ [101]. The fireball duration τ is the ratio of the dilepton yield and the pion yield introduced in Tab. 5.1, multiplied by 1.25×10^6 [102].

temperature at low energies. The left panel of Fig. 5.12 shows the dilepton yield produced in each time step. One clearly sees a similar evolution as for the pion densities, with PHSD having a large dilepton production corresponding to the large pion production, while UrQMD, also reaching a higher maximum in the dilepton production as well as the pion production than GiBUU and SMASH, experiences a steeper drop than the latter two, which run almost in parallel.
Consider the McLerran-Toimela formula (2.28). The ratio $\text{Im}\Pi_{\text{EM}}/M^2$ of electromagnetic spectral function and squared invariant mass is constant in the low mass region from 0.2-0.7 GeV/c^2. This means that the Bose factor $f^{BE}(q_0, T) = (\exp(q_0/T) - 1)^{-1}$ is the dominating part of the dilepton spectrum in this region, describing an almost exponential decrease. Fitting a function of the form

$$\frac{dN}{dM_{ee}} \propto M_{ee}^{3/2} \exp(-M_{ee}/T), \tag{5.1}$$

a fireball temperature can be obtained. The fit is applied in the low mass region as seen in Fig. 5.13. The temperatures reproduced from the fireball in the low mass range by exponential fitting can be seen in Tab. 5.3. While the temperatures fit in the central region of the fireball as expected, the divergences are larger, if the full volume is considered. It seems as if GiBUU and SMASH reproduce the temperature obtained by the HADES collaboration best.

model	HADES	UrQMD	GiBUU	SMASH	PHSD
T 5x5x5 [MeV]	–	64.5 ± 0.1	66.1 ± 0.1	67.7 ± 0.1	62.9 ± 0.1
T Full Volume [MeV]	71.8 ± 2.1	66.7 ± 0.1	73.4 ± 0.1	71.3 ± 0.1	67.9 ± 0.1

Table 5.3: Temperatures obtained by an exponential fit to the low mass range of dilepton invariant mass spectra produced with different models and the HADES experiment for Au+Au at $\sqrt{s_{NN}} = 2.42$ GeV at 0-40 % centrality in the central 5x5x5 cells and the full yield [59]

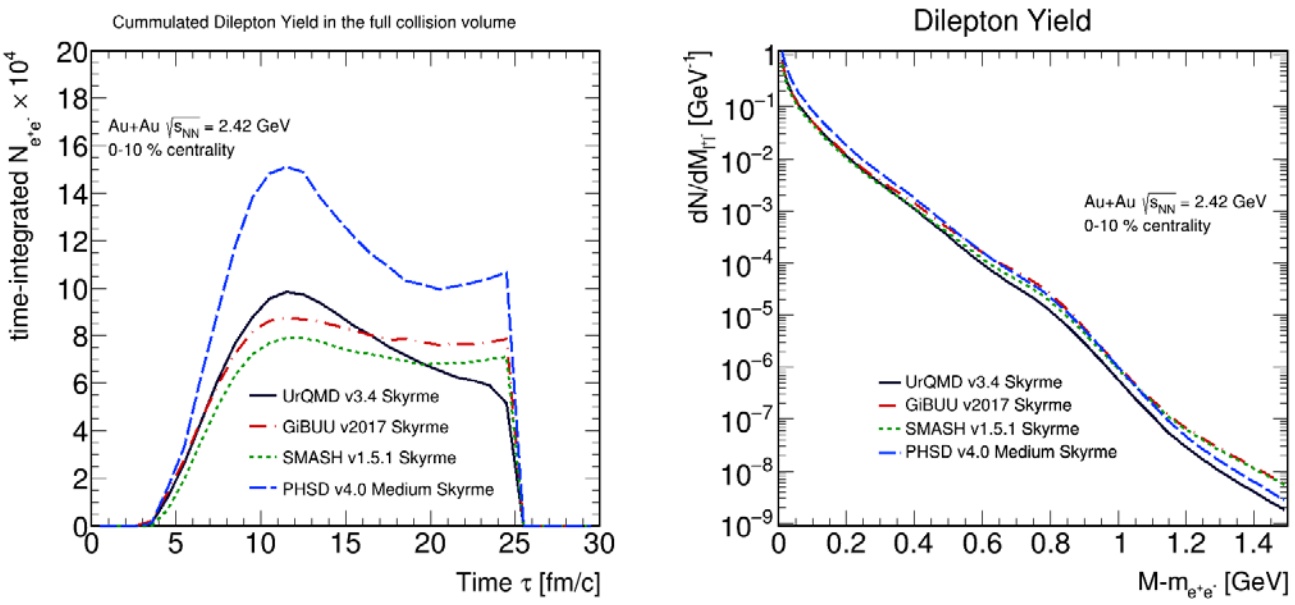

Figure 5.12: Left panel: Comparison of the dilepton Yield produced in each time step for the different models. Right panel: Invariant mass specturm obtained for the full thermalized collision volume for each model.

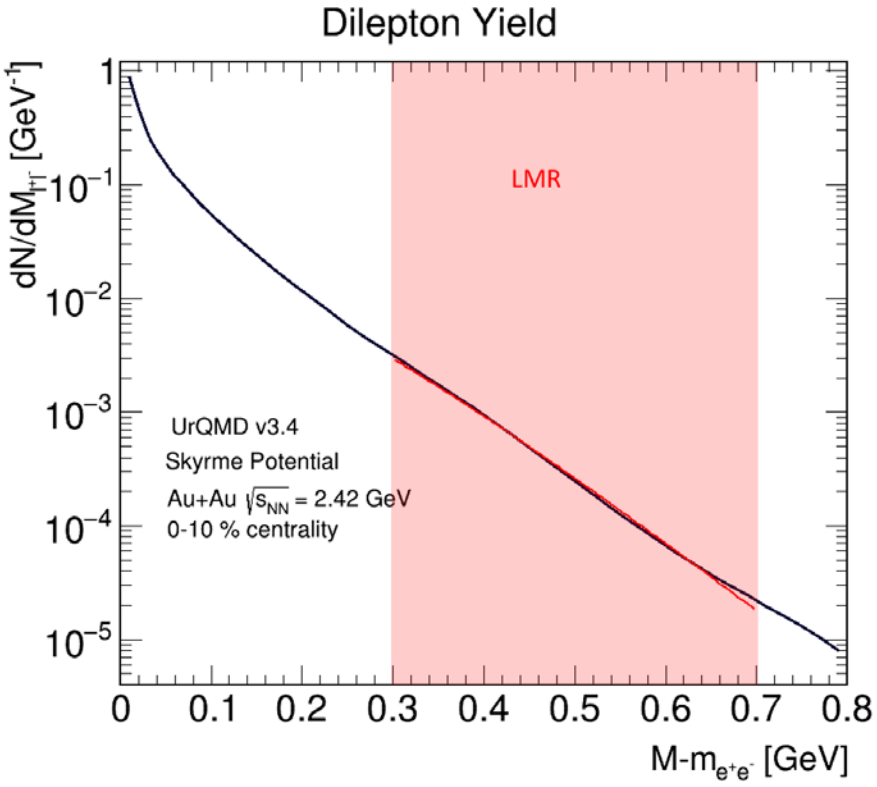

Figure 5.13: A spectrum for UrQMD Au+Au with the fit region and the fit as given in Eq. (5.1) in red.

5.4 Comparison of Skyrme and cascade potential

The cascade mode of UrQMD produces 39 particles, compared to the 38 particles produced by UrQMD Skyrme, as expected. The mean number of collisions in the cascade case is ∼11, while the number of collisions for the Skyrme mode is only ∼7, which is suprising at first considering the almost identical meson production. The Skyrme potential is repulsive, so the higher number of collisions for the cascade mode is expected, but it stands to reason that the number of inelastic collisions is not quenched significantly by the Skyrme potential as elastic collisions generally appear at lower energies, being quenched stronger by the Skyrme potential, which leaves the inelastic collisions mostly intact.

The densities can be seen in the panels of Fig. 5.14. They vary strongly for different potentials, since they are mainly determined by the incompressibility of the nuclear medium, which is directly linked to the EoS. This leads to a density in cascade mode twice as high as the density in Skyrme mode. The pion densities show large differences, in their time evolution, even though their maxima are similar. Comparing the pion (Fig. 5.14, right panel) and baryon densities (Fig. 5.14, left panel), it becomes clear that the profile of the pion density is linked to the baryon density, but the relation is not straightforward.

The higher pion densities in the later time step for the cascade mode also leads to a higher number of thermalized cells, which is an unexpected behaviour. Since the densities in the cascade case are higher, the obvious thought would be a smaller collision volume. This points to more work needed for the thermalization yet again.

Clearly visible in Fig. 5.16, the temperature continues to rise after thermalization for the cascade mode, while this is not the case for the Skyrme mode, which reflects the behaviour of the pion density, affirming a strong relation between the pion density and the temperature. The maximum temperature in cascade mode is around 90 MeV. In contrast to the project proposal for this thesis, which used the approximation in Eq. (4.12) for the temperature determination and the classical collision criterion to obtain very simi-

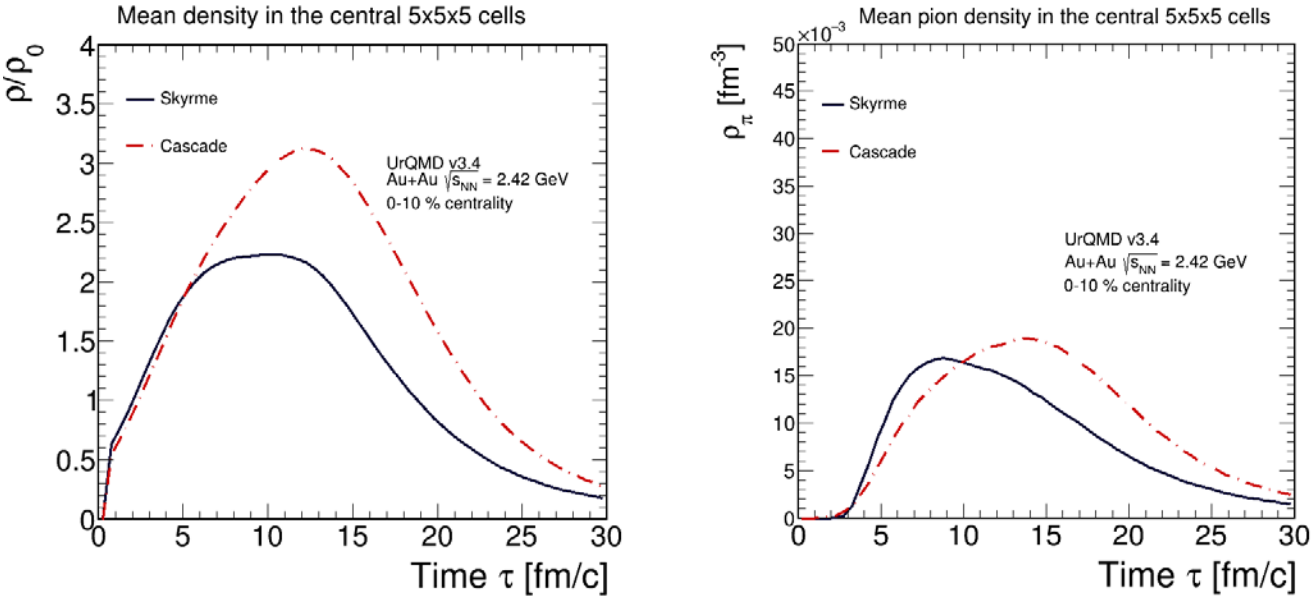

Figure 5.14: Left panel: Comparison of the effective baryon density evolution for cascade and Skyrme potential.Right panel: Comparison of the pion density evolution for cascade and Skyrme potential.

lar spectra for both potentials, there is a significant difference between the dilepton spectra calculated with cascade and Skyrme potentials. This is due to the very similar number of thermalized cells, which would differ using the classical UrQMD collision criterion for thermalization, as has been employed in the proposal [97]. This will be shown in the discussion of the approximation in Section 7.2. Regarding the dilepton yield and the pion production, the invariant mass spectrum produces an integrated yield of 3.4×10^{-4}, and a multiplicity of charged pions in the $|y|<0.5$ range of 13. Employing the formula for the fireball lifetime, this leads to a duration of 33 fm/c, which is clearly more than for the Skyrme potential. However, comparing the densities in Fig. 5.14, this does not seem completely unrealistic, because the highly compressed medium needs more time to reexpand in case of the cascade potential. The temperature obtained from the dilepton spectrum is at around 70 MeV, which is close to the temperature measured by the HADES collaboration.

5.5 Comparison of Ag+Ag and Au+Au at different centralities, system sizes and energies

The comparison of gold-gold and silver-silver collisions is important because there is a number of observables scaling with the number of participant nucleons in a collision system. To obtain clean data and understand these effects as good as possible, comparisons of different collision systems need to be made to sort out any effects that do not originate from general medium properties, but simply from specific dynamics associated with the colliding nuclei.
The similarities between the silver and gold systems are striking, even at different A_{part}. While the duration of a collision of silver nuclei is only half as long as the duration of a collision of gold nuclei at the same energy (see Fig. 5.18, black and red dotted-dashed curves), the maximum effective baryon and pion densities are equal and the forms of each profile match perfectly for the first 10 fm/c. The lower number of participants essentially just shortens the fireball life time.

The same is true for the temperatures (see Fig. 5.19, black and red dotted-dashed curves). However, since the number of participants is only 168 for Ag+Ag instead of 306 for the Au+Au system, the thermalized volume is smaller (see right and left panel of Fig. 5.19). This leads to dilepton spectra for the Ag+Ag case

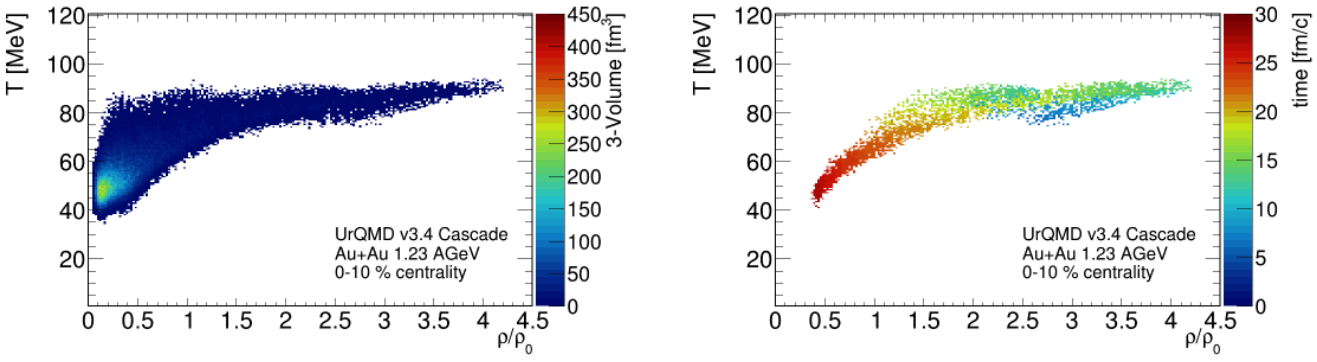

Figure 5.15: Left panel: Distribution of the thermalized volume in Au+Au collisions at 1.23A GeV with cascade potential.Right panel: Trajectory of the central 5x5x5 cells in the $\rho - T$-plane.

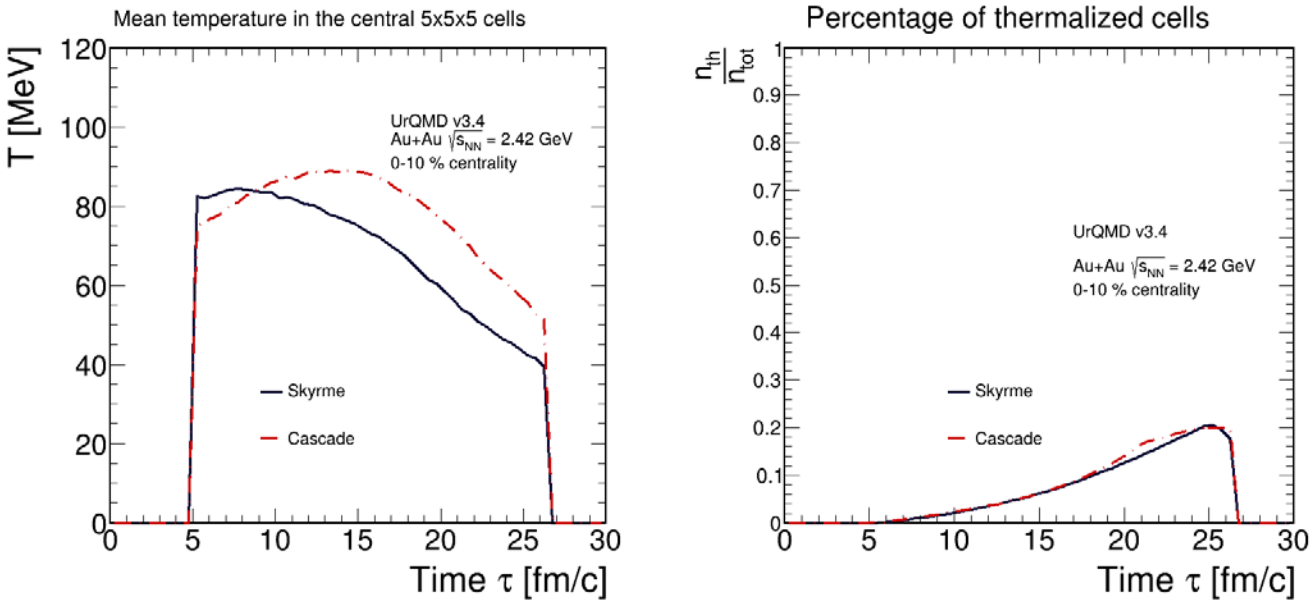

Figure 5.16: Left panel: Comparison of the temperature evolution for cascade and Skyrme potential. Right panel: Comparison of the evolution of thermalised volume for cascade and Skyrme potential.

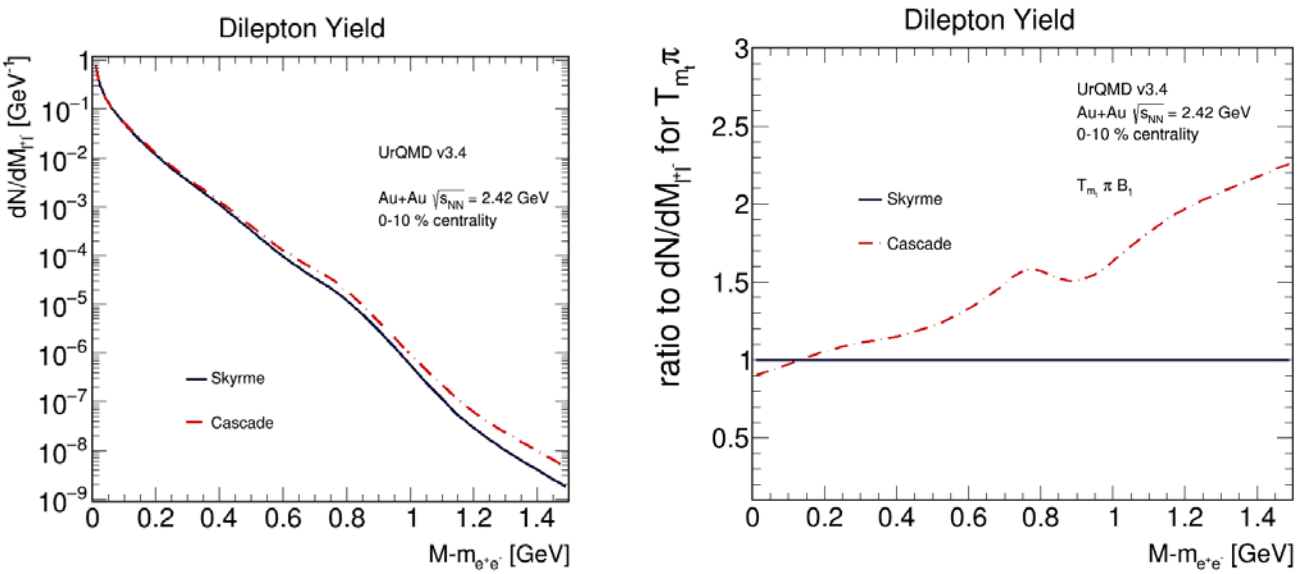

Figure 5.17: Left panel: Comparison of the invariant mass spectra for cascade and Skyrme potential. Right panel: Ratio of the cascade invariant mass spectrum to the spectrum obtained with a Skyrme potential.

which have almost exactly the same form as shown in Fig. 5.20 (left panel), but are lower by a factor of 2.5 compared to the Au+Au case. This factor is to be compared to the ratio of A_{part} in both systems:

$$\frac{A_{\text{Au+Au}}}{A_{\text{Ag+Ag}}} = 306/168 \approx 1.8, \tag{5.2}$$

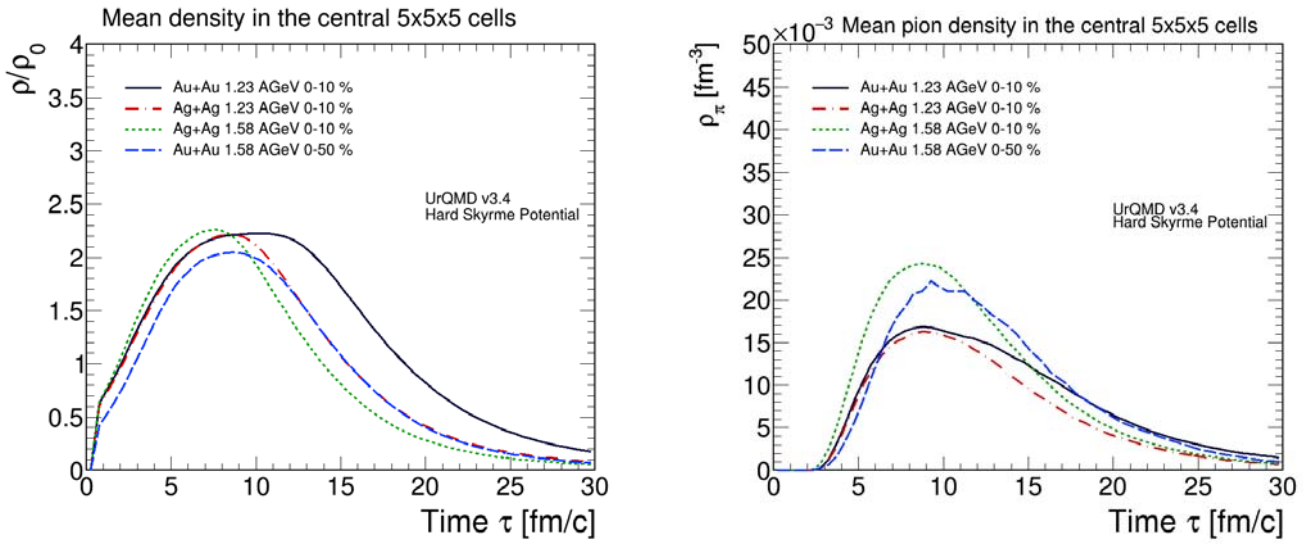

Figure 5.18: Left panel: Comparison of the effective baryon density evolution in gold and silver collisions at 1.23A GeV. Right panel: Comparison of the pion density evolution in gold and silver collisions at 1.23A GeV.

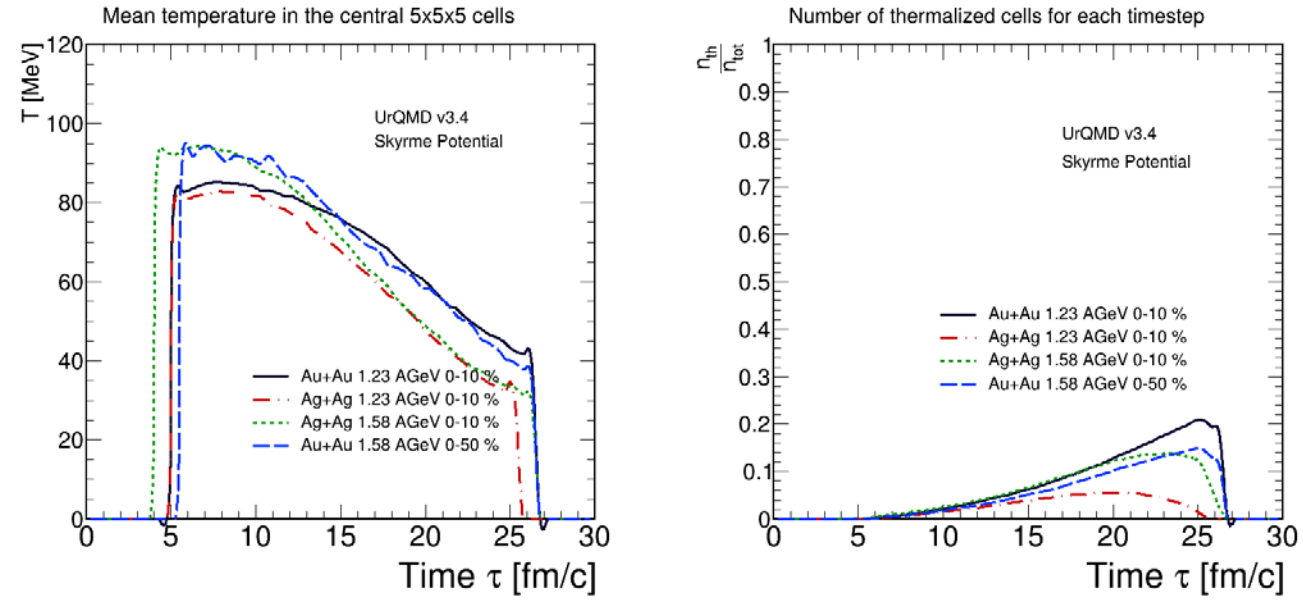

Figure 5.19: Left panel: Comparison of the temperature obtained for the different collision systems with UrQMD. Right panel: Comparison of the thermalized volume for the the different systems with UrQMD.

pointing to a dependence of the dilepton yield on A_{part}. Because of the lower baryon density in the intermediate stages of the fireball life time in the Ag+Ag case, the dilepton yield in the intermediate mass range is slightly higher than expected in a pure scaling scenario, due to the melting of the ρ-resonance being not as pronounced as in the Au+Au case. Moving from an Ag+Ag collision at 1.23A GeV to an Ag+Ag collision at 1.58A GeV, it can be recognized the baryon density only weakly depends on the collision

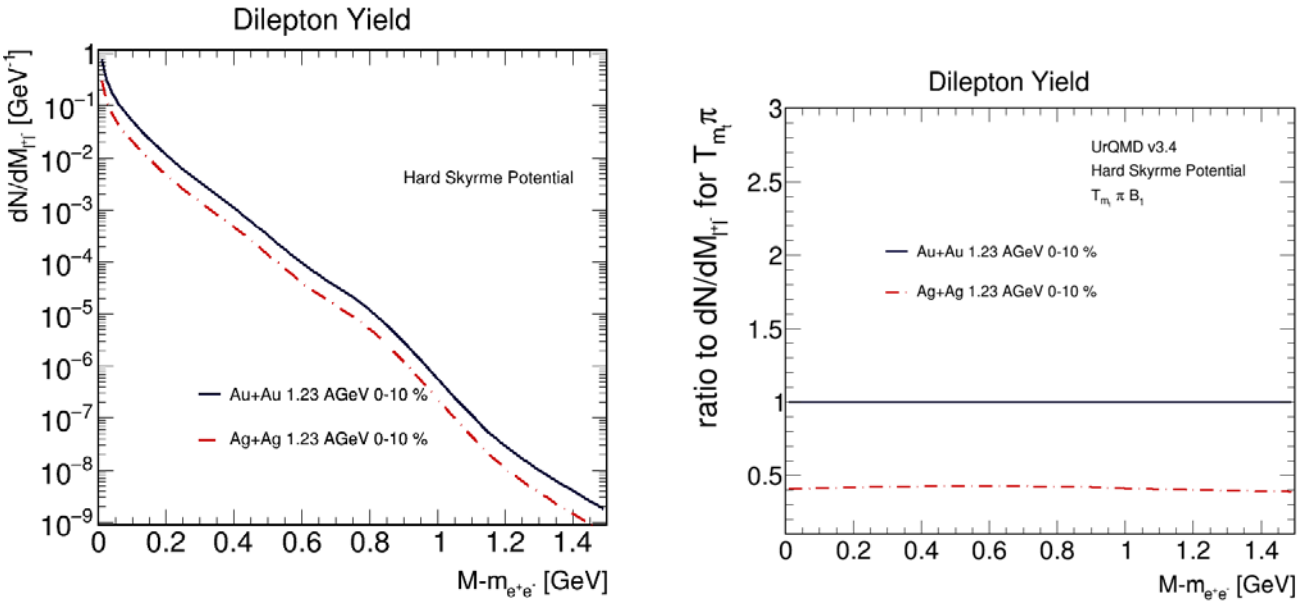

Figure 5.20: Left panel: Invariant Mass spectrum of gold and silver collisions at the same energy of 1.23A GeV and centrality of 0-10 %. Right panel: Ratio of the invariant mass spectra of gold and silver collisions at the same energy of 1.23A GeV and centrality of 0-10 %.

energy in the left panel of Fig. 5.21, however, there is a strong dependence of the pion production on the collision energy, becoming almost twice as large in the intermediate stages of the collision (see right panel of Fig. 5.18. The same is obviously also true for the temperatures and thermalized volume. However, the fireball cools down quicker than for the system at 1.23A GeV. This might be an effect of Lorentz contraction.

The comparison of Au+Au and Ag+Ag collisions at the same energy of 1.58A GeV and the same number of participants $A_{\text{part}} = 168$ yields slight differences in both systems. The Ag+Ag system reaches a maximum density 10 % higher than the corresponding Au+Au system, followed by a steep drop, which is less pronounced in the gold-gold system. The pion density evolution behaves similarly. A more detailed analysis of this behaviour is given in Section 5.6. Due to the faster evolution of the pion densities in silver collisions, thermalization sets in slightly sooner than in gold collisions. However, the lifetime is longer due to the less steep fall of the densities in the gold-case. Moreover, the fireball does not cool down as fast in the case of

System	Au+Au	Ag+Ag	Ag+Ag	Au+Au
Energy [A GeV]	1.23	1.23	1.58	1.58
Centrality	0-10 %	0-10 %	0-10 %	0-50 %
e^+e^- yield	2.9×10^{-4}	1.3×10^{-4}	2.7×10^{-4}	2.3×10^{-4}
$N^{\pm}_{\lvert y\rvert<0.5}$	13.92	8.11	11.9	10.4
τ [fm/c]	26.1	20.0	28.4	27.6
T Full Volume [MeV]	66.7±0.1	66.8±0.1	75.9±0.2	77.4±0.1

Table 5.4: Dilepton yields, pion multiplicities, lifetimes and temperatures obtained from the dilepton spectra of the corresponding systems.

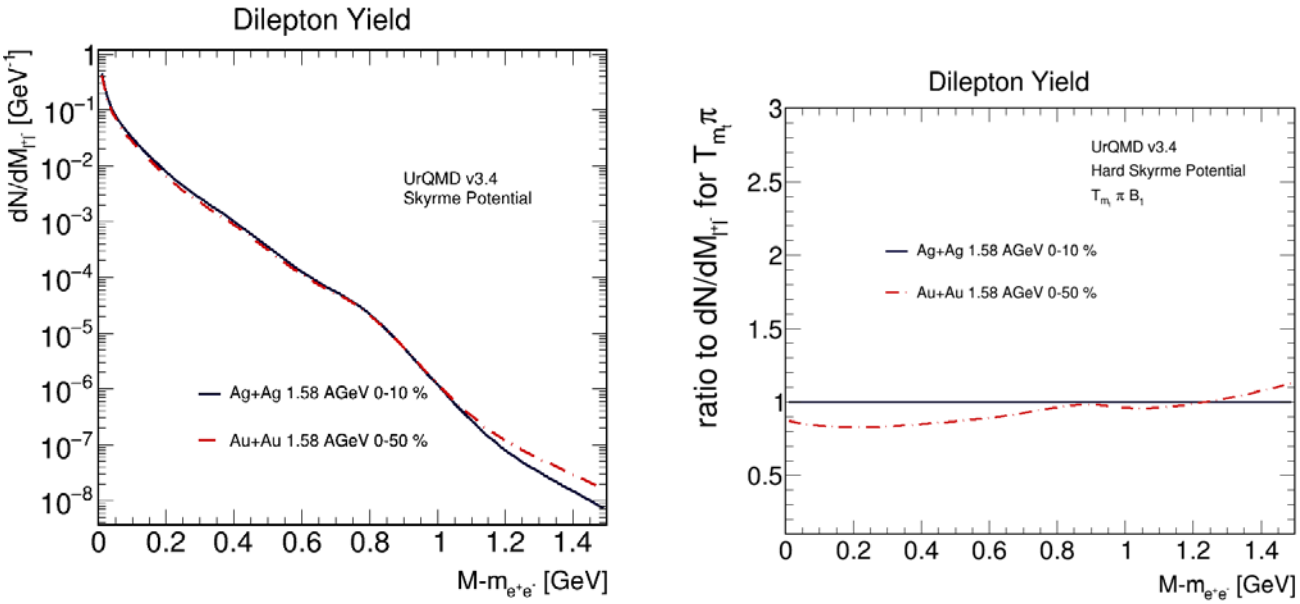

Figure 5.21: Left panel: Invariant Mass spectrum of gold and silver collisions at the same energy of 1.58A GeV and A_{part} of 168. Right panel: Ratio of the invariant mass spectra of gold and silver collisions at the same energy of 1.58A GeV and A_{part} of 168.

the gold-collisions.

Despite all the differences, the gold and silver collisions produce spectra which lie within a maximum difference of 20 % of each other in the low mass range. In the region $0.8 < M < 1.2\,\text{GeV/c}^2$ mass, they are equal. The dilepton yields and pion production are summarized in Tab. 5.4. The temperatures obtained by fits to the invariant mass spectra are plausible. For the lower energy systems, they are equal. For the higher energy systems, a slight difference is seen. This might be due to the slower cooling of the fireball in the gold-system at the higher energy. Just as seen in the calculation of the fireball life time for the different models, UrQMD seems to overestimate the fireball lifetimes. It is possible that the pion yield is too small or the number of thermalized cells is overestimated. However, at least qualitatively in relation to each other, the lifetimes reproduce the ones that can be read of from Fig. 5.18 and Fig. 5.20.

5.6 Comparison of pion densities in different collision systems

As seen in Section 5.5, Ag+Ag and Au+Au collisions produce different numbers of charged pions in the rapidity ranges from $-0.5 < y_{\text{cm}} < +0.5$, even if carried out at the same energy and A_{part}. This section will further explore this behaviour. There are two important points why this needs to be done: (i) the pion densities influence the dilepton yield through the fugacity factor $z = \exp(k\frac{\mu_\pi}{T})$, where μ_π is the density-dependent pion chemical potential; (ii) the dilepton yield in the low mass range is used as a chronometer of the collision in conjunction with the pion yield. The understanding of the pion production and its dependence on the number of spectator nucleons is therefore very important when comparing different collision systems.

For this purpose, 1000 events have been simulated additionally for three different nucleus-nucleus collisions at 1.58A GeV in UrQMD Skyrme mode. The centralities are chosen in such a way that the number of

participants is roughly equal for each system. They are given with their pion yield for different cuts in Tab. 5.5 for a time of τ=30 fm/c after the beginning of the heavy-ion collision. It can be immediately seen that at the same A_{part}, the number of pions produced decreases with the total number of nucleons. It seems that the particles that would be assumed to act only as spectators influence the number of pions produced. The pion yield for this class of systems is described by a polynomial of second order in the number of spectator nucleons A_{spec}, as can be seen in the right panel of Fig. 5.22. Moreover, it is clearly seen in the left panel that the duration of the collision increases slightly with A, but the maximum pion density decreases more dramatically with A_{part}. Furthermore, the number of Δ-baryons produced in each collision increases slightly with A. While Δ-baryons can be created by π-N-collisions, the sum of N_Δ and N_π is not constant for the collision systems, suggesting different mechanisms acting. A more thorough analysis needs to be done in the future regarding collision histories of pions as well as a detailed comparison of the yield of different hadrons. Experimental data would be needed to help constrain such effects.

nuclei	Ag+Ag	Xe+Xe	Sm+Sm	Er+Er	Au+Au
A	2×109	2×130	2×150	2×170	2×197
b_{max}[fm]	3.9	5.8	7.4	8.7	10.4
A_{part}	168	167.4	167.4	168.1	165.5
N_π	36.1	35.5	34.4	33.6	33
$N_{\|y\|<0.5}$	18.3	17.8	17.2	16.50	16.0
$N^\pm$	23.5	23.4	22.6	22.1	21.7
$N^\pm_{\|y\|<0.5}$	11.9	11.7	11.3	10.9	10.4
N_Δ	0.3	0.6	0.8	0.9	1.1

Table 5.5: Pion Yields for different collision systems with maximum impact parameter b_{max} chosen for similar A_{part} at 1.58A GeV, simulated with UrQMD. The values have been taken at τ=30 fm/c. N_π is the total number of pions, $N^\pm$ is the number of charged pions and $N_{|y|<0.5}$ is the number of pions in the $|y| < 0.5$ rapidity range, while N_Δ is the number of Δ-baryons.

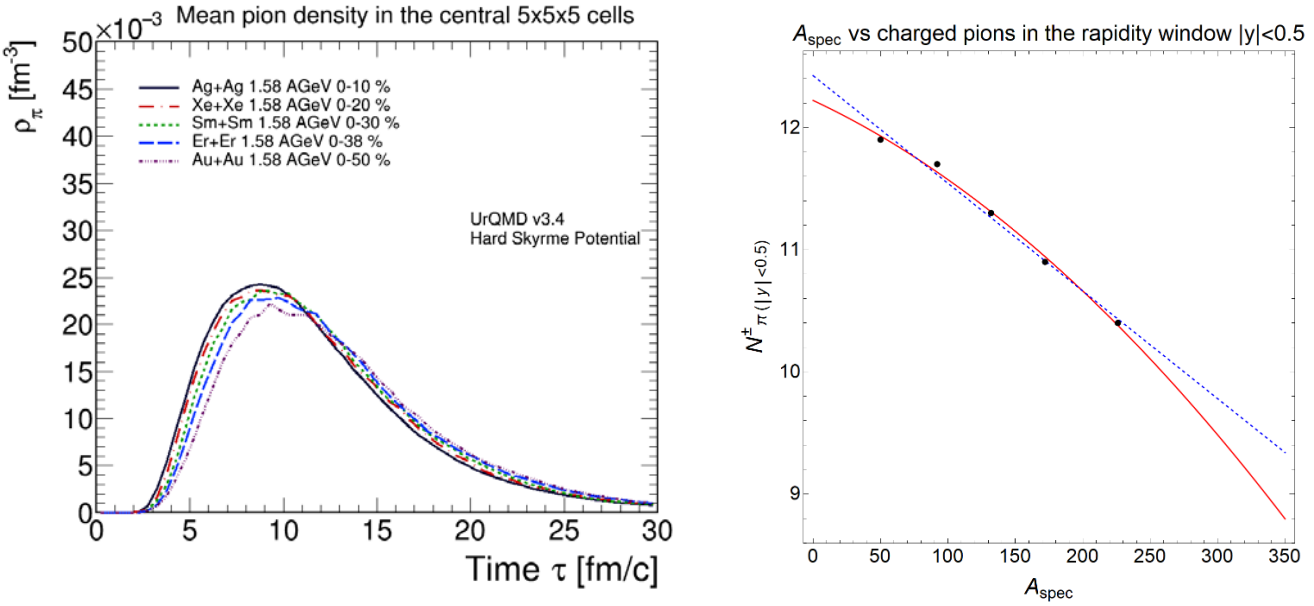

Figure 5.22: Left panel: Comparison of the pion density evolution for different collision systems at similar A_{part}.Right panel: Comparison of the yields in the |y|<0.5 rapidity range (black dots) with the quadratic fit $-1.3 \times 10^{-5}A^2 - 1.4 \times 10^{-2}A + 12.2$ (solid red line) and a linear fit $-8.8 \times 10^{-3}A + 12.4$ (dashed blue line). The x-axis denotes the number of spectators.

6 Conclusions and Outlook

In this work, a coarse graining approach has been used to compare four prominent models to simulate heavy-ion collisions employing the Rapp-Wambach spectral function to extract dilepton spectra. Further, comparisons of system size and energy dependence of dilepton spectra have been produced. Additionally, it has been shown that the pion yield is influenced by the number of spectators as well as the number of participants. Dilepton yields and temperatures have been extracted from the spectra and the duration of the fireball has been calculated from the yields. This has led to the prediction of the thermal dilepton spectra for Ag+Ag at 1.58A GeV and 1.23A GeV, which has been measured by the HADES collaboration.
Several points need to be addressed in the future. Determination of thermalization is still an ongoing problem, as the method employed in this work is not motivated by an underlying principle, but only by the need to produce a similar thermalized volume. A candidate might be the comparison of a wide range of thermal observables that would need to be reproduced analytically. Other relaxation functions derived for different transverse and longitudinal momentum distributions could be additionally employed.
The rejection of protons for temperature determination based on a defined fraction of the beam velocity is only superficially satisfying. It cannot bring the two temperatures of protons into unison for any model, which is an important indication that there is an issue that has been overlooked. Furthermore, adjustments in the pion production cross sections of the models to better fit the results of the HADES collaboration would be needed to precisely predict the pion densities. The pion production in different collision systems will need to be investigated further. Observables like ellipticity and flow coefficients could show the exact means of the pion quenching in larger systems.
The Ag+Ag predictions at 1.23A GeV and 1.58A GeV will be compared to HADES data already taken once the analysis is finished. This will show where improvements of the coarse graining method are necessary to further improve the understanding of thermal dilepton radiation as probes of the strongly interacting matter produced in heavy-ion collisions.

7 Appendix

7.1 Derivation of mean transverse mass

Starting from the Boltzmann approximation

$$< m_t >= \frac{\int_{-\infty}^{\infty}\int_{-\infty}^{\infty}\int_{-\infty}^{\infty} dp_x dp_y dp_z \left(\sqrt{p_x^2+p_y^2+m^2}\right) e^{-\frac{\sqrt{p_x^2+p_y^2+p_z^2+m^2}}{T}}}{\int_{-\infty}^{\infty}\int_{-\infty}^{\infty}\int_{-\infty}^{\infty} dp_x dp_y dp_z e^{-\frac{\sqrt{p_x^2+p_y^2+p_z^2+m^2}}{T}}}, \tag{7.1}$$

the analytical expression of Eq. (4.17) will now be derived.
In polar coordinates, $(p_x, p_y, p_z) = p(\sin(\theta)\cos(\phi), \sin(\theta)\sin(\phi), \cos(\theta))$. The introduction of polar coordinates into Eq. (7.1) yields

$$< m_t >= \frac{\int_0^{\pi}\int_0^{2\pi}\int_0^{\infty} d\theta d\phi dp p^2 \sin(\theta) \left(\sqrt{p^2\sin(\theta)^2+m^2}\right) e^{-\frac{\sqrt{p^2+m^2}}{T}}}{\int_0^{\pi}\int_0^{2\pi}\int_0^{\infty} d\theta d\phi dp p^2 \sin(\theta) e^{-\frac{\sqrt{p^2+m^2}}{T}}}, \tag{7.2}$$

where the angular dependence in ϕ-direction obviously cancels out, yielding

$$\frac{\int_0^{\pi}\int_0^{\infty} d\theta dp p^2 \sin(\theta) \left(\sqrt{p^2\sin(\theta)^2+m^2}\right) e^{-\frac{\sqrt{p^2+m^2}}{T}}}{\int_0^{\pi}\int_0^{\infty} d\theta dp p^2 \sin(\theta)^2 e^{-\frac{\sqrt{p^2+m^2}}{T}}}. \tag{7.3}$$

The denominator has been solved in Appendix 6.8 in [54], yielding

$$\int_0^{\infty} dp p^2 e^{-\frac{-\sqrt{p^2+m^2}}{T}} = \frac{m^3}{2}\left(K_3\left(\frac{m}{T}\right) - K_1\left(\frac{m}{T}\right)\right). \tag{7.4}$$

The numerator is solved in a similar manner, beginning with the solution of the integral over θ. Using a change of variables and writing $E = \sqrt{p^2+m^2}$ for better visibility,

$$\int_0^{\pi} d\theta \sin(\theta)\sqrt{p^2\sin(\theta)^2+m^2} = \int_1^{-1} d\cos(\theta)\sqrt{p^2(1-\cos(\theta)^2)+m^2} \tag{7.5}$$

$$= p\int_1^{-1} du \sqrt{\frac{E^2}{p^2}-u^2} \tag{7.6}$$

$$= \frac{p}{2}\left[u\sqrt{\frac{E^2}{p^2}-u^2} + \frac{E^2}{p^2}\tan^{-1}\left(\frac{u}{\sqrt{\frac{E^2}{p^2}-u^2}}\right)\right]_1^{-1} \tag{7.7}$$

$$= \left(m + \frac{E^2}{p}\tan^{-1}\left(\frac{p}{m}\right)\right) \tag{7.8}$$

Merging the last line with the omitted momentum integral gives

$$\int_0^\infty dpp^2 e^{-\frac{E}{T}} \left(m + \frac{E^2}{p} \tan^{-1}\left(\frac{p}{m}\right)\right) = \int_0^\infty dpp^2 e^{-\frac{E}{T}} m + \int_0^\infty dppe^{-\frac{E}{T}} E^2 \tan^{-1}\left(\frac{p}{m}\right). \tag{7.9}$$

The first term reproduces the momentum integral of the denominator multiplied by a factor of m. For the second term, with $1/T = \beta$,

$$\int_0^\infty dppe^{-\beta E} E^2 \tan^{-1}\left(\frac{p}{m}\right) = \frac{\partial^2}{\partial \beta^2} \int_0^\infty dppe^{-\beta E} \tan^{-1}\left(\frac{p}{m}\right). \tag{7.10}$$

A partial integration needs to be performed. $pe^{-\beta E}$ is chosen to be integrated via a transformation of variables from p to E with $dp = dEE/p$,

$$\int dppe^{-\beta E} = \int dEEe^{-\beta E}, \tag{7.11}$$

$$= \frac{\partial}{\partial \beta} \int dEe^{-\beta E}, \tag{7.12}$$

$$= -\frac{\partial}{\partial \beta} \frac{1}{\beta} e^{-\beta E}, \tag{7.13}$$

$$= \frac{e^{-\beta E}(1+\beta E)}{\beta^2}. \tag{7.14}$$

For the partial integration, this means

$$\int_0^\infty dppe^{-\beta E} \tan^{-1}\left(\frac{p}{m}\right) = \left[\frac{e^{-\beta E}(1+\beta E)}{\beta^2} \tan^{-1}\left(\frac{p}{m}\right)\right]_0^\infty - \int_0^\infty dp \frac{e^{\beta E}(1+\beta E)}{\beta^2} \frac{m}{E^2}, \tag{7.15}$$

$$= 0 - \frac{m}{\beta^2} \int_0^\infty dpe^{-\beta E}(1+\beta E) \frac{1}{E^2}, \tag{7.16}$$

$$= -\frac{m}{\beta^2} \int_0^\infty dp \frac{e^{-\beta E}}{E^2} + \frac{\beta e^{-\beta E}}{E}. \tag{7.17}$$

Noting that $e^{-\beta E}/E = -\int_\infty^\beta d\kappa e^{-\kappa E}$ and using this recursively, Eq. (7.17) can be written as

$$-\frac{m}{\beta^2} \int_0^\infty dp \frac{e^{-\beta E}}{E^2} + \frac{\beta e^{-\beta E}}{E} = -\frac{m}{\beta^2} \left(-\beta \int_0^\infty dp \int_\infty^\beta d\kappa e^{-\kappa E} + \int_0^\infty dp \int_\infty^\beta d\kappa \int_\infty^\kappa d\tau e^{-\tau E} \right), \tag{7.18}$$

$$= -\frac{m}{\beta^2} \left(-\beta \int_\infty^\beta d\kappa \int_0^\infty dpe^{-\kappa E} + \int_\infty^\beta d\kappa \int_\infty^\kappa d\tau \int_0^\infty dpe^{-\tau E} \right). \tag{7.19}$$

The last line is obtained by swapping the integrals. Following the approach of Appendix 6.8 in [54], the substitution $p = m\sinh(y)$, giving $dp = m\cosh(y)dy$ and $E = m\cosh(y)$, yielding

$$\int_0^\infty dpe^{-\tau E} = m \int_0^\infty dy \cosh(y) e^{-\tau m \cosh(y)}, \tag{7.20}$$

$$= mK_1(m\tau), \tag{7.21}$$

$$\tag{7.22}$$

where the last equality follows from the definition of the modified Bessel functions of second order which can be looked up in [103], transforming Eq. (7.19) into

$$-\frac{m}{\beta^2} \left(-\beta \int_\infty^\beta d\kappa m K_1(m\kappa) + \int_\infty^\beta d\kappa \int_\infty^\kappa d\tau m K_1(m\tau) \right) = \frac{m}{\beta^2} \left(-\beta K_0(m\beta) + \int_\infty^\beta d\kappa K_0(m\kappa) \right). \tag{7.23}$$

The integral in the second term of the right side of Eq. (7.23) can be looked up or performed by Computer Algebra Systems (CAS), and evaluates to

$$\int_{\infty}^{\beta} d\kappa K_0(m\kappa) = \frac{1}{2}\pi\beta(\boldsymbol{L}_{-1}(m\beta)K_0(m\beta) + \boldsymbol{L}_0(m\beta)K_1(m\beta)), \tag{7.24}$$

where $\boldsymbol{L}_\nu$ are the modified Struve functions. Reimposing the derivatives of Eq. (7.10), the solution to the momentum integral is

$$\int_0^{\infty} dppe^{-\beta E}E^2 \tan^{-1}\left(\frac{p}{m}\right) = \frac{\partial^2}{\partial\beta^2}\frac{m}{\beta^2}\left(-\beta K_0(m\beta) + \frac{1}{2}\pi\beta(\boldsymbol{L}_{-1}(m\beta)K_0(m\beta) + \boldsymbol{L}_0(m\beta)K_1(m\beta))\right). \tag{7.25}$$

Taking the derivatives is straight forward but lengthy. After taking the derivatives, in another lengthy but straight forward step, the remaining Struve functions are boiled down via their recursion relations to fit the two orders defined in CERN Root, $\boldsymbol{L}_0$ and $\boldsymbol{L}_1$. This process finally gives the formula for the numerator. Dividing by the denominator, the thermal mean of the transverse mass in a classical ideal gas $\langle m_t\rangle_T$ is obtained

$$\langle m_t\rangle_T = \frac{T}{\mathcal{N}(m,T)}\left[-\pi m\boldsymbol{L}_1\left(\frac{m}{T}\right)\Phi(m,T) + \pi mT\boldsymbol{L}_0\left(\frac{m}{T}\right)\Omega(m,T) + \Sigma(m,T))\right] + \frac{m}{2}, \tag{7.26}$$

where: (7.27)

$$\mathcal{N}(m,T) = m^3\left[K_1\left(\frac{m}{T}\right) - K_3\left(\frac{m}{T}\right)\right], \tag{7.28}$$

$$\Phi(m,T) = \left(m^2 + 6T^2\right)K_0\left(\frac{m}{T}\right) + m\left[2TK_1\left(\frac{m}{T}\right) - mK_2\left(\frac{m}{T}\right)\right], \tag{7.29}$$

$$\Omega(m,T) = mK_0\left(\frac{m}{T}\right) - 4TK_1\left(\frac{m}{T}\right) - mK_2\left(\frac{m}{T}\right), \tag{7.30}$$

$$\Sigma(m,T) = 2m^3K_2\left(\frac{m}{T}\right) + 4m^2TK_1\left(\frac{m}{T}\right) + 6\pi T^3. \tag{7.31}$$

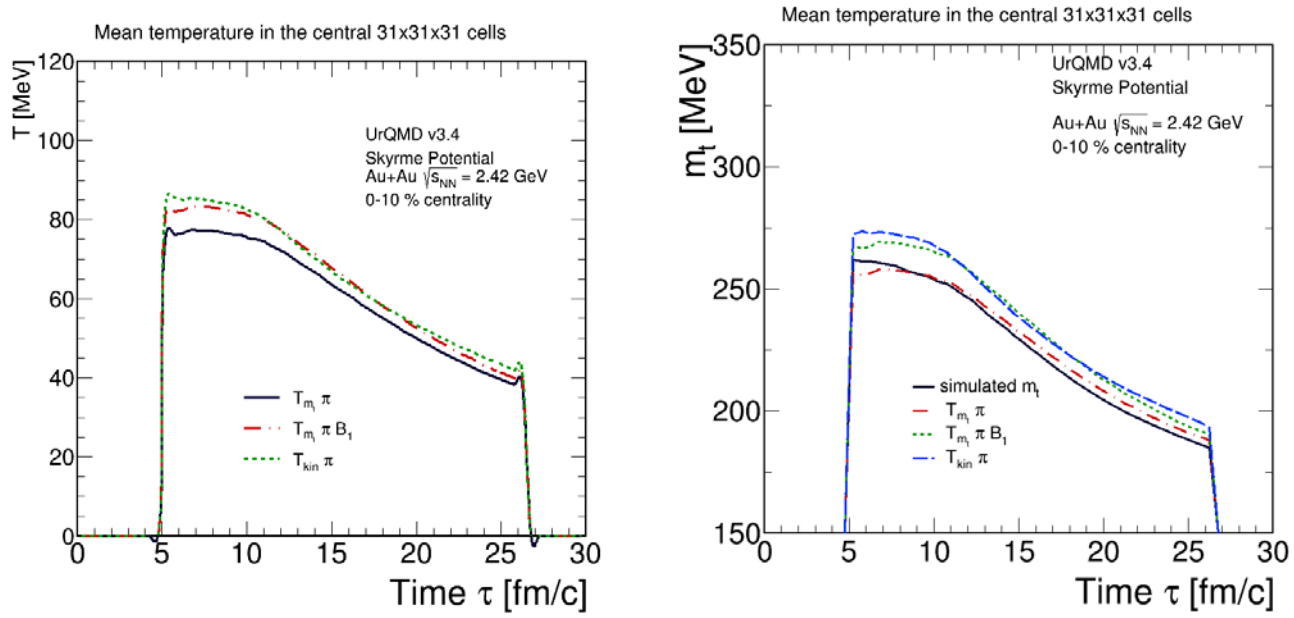

Figure 7.1: Left Panel: Comparison of Bessel fit temperature, exponential fit temperature and kinetic energy temperature of pions. Right Panel: Comparison of simulated m_t to the values obtained by the analytic solution with the temperatures.

7.2 Comparison of exponential and Bessel Function in fits for temperature determination

This section will deal with the similarities and differences between the approximate and the exact fit to pion transverse mass spectra to obtain temperatures as discussed in Section 4.2.4. As can be seen in Fig. 7.1, the temperature of the fit with a Bessel function better reproduces the kinetic energies at high temperatures in early stages of the collision. However, comparing the simulated transverse mass to the analytic transverse masses, the simulated transverse pion mass is perfectly reproduced by the exponential fit. Why this is the case is unclear. However, the Bessel fit being in line with the momentum-direction independent kinetic energy would point to a more isotropic momentum distribution, while the exponential fit matching the simulated transverse mass would point to a more anisotropic momentum distribution.

7.3 Input files for models and collision systems

7.3.1 UrQMD Au+Au 1.23A GeV 0-10 %

```
pro 197 79
tar 197 79
nev 1000
IMP 0.0 4.7
elb 1.23
tim 30 0.5
eos 1
cdt 0.25
f13
#f14
#f15
f16
f19
f20

xxx
```

7.3.2 UrQMD Ag+Ag 1.23A GeV 0-10 %

```
pro 109 47
tar 109 47
nev 1000
IMP 0.0 3.9
elb 1.23
tim 30 0.5
eos 1
cdt 0.25
f13
#f14
f15
f16
f19
f20

xxx
```

7.3.3 UrQMD Ag+Ag 1.58A GeV 0-10 %

```
pro 109 47
tar 109 47
nev 1000
IMP 0.0 3.9
elb 1.58
tim 30 0.5
eos 1
cdt 0.25
f13
#f14
f15
f16
f19
f20

xxx
```

7.3.4 UrQMD Au+Au 1.58A GeV 0-50 %

```
pro 197 79
tar 197 79
nev 1000
IMP 0.0 10.4
elb 1.58
tim 30 0.5
eos 1
cdt 0.25
f13
#f14
f15
f16
f19
f20

xxx
```

7.3.5 SMASH Au+Au 1.23A GeV 0-10 %

```
Version: 1.5 # minimal SMASH version to use with this config file
Logging:
    default: INFO
General:
    Modus:         Collider
    Time_Step_Mode: Fixed
    Delta_Time:    0.25
    End_Time:      30.0
    Randomseed:    -1
    Nevents:       250
    Testparticles: 20
Output:
    Output_Interval: 0.5
    Particles:
        Format:          ["Oscar2013"]
        Extended: True
        Only_Final: False
Modi:
    Collider:
        Projectile:
            Particles: {2212: 79, 2112: 118} #Gold197
            Saturation_Density: 0.16
            Diffusiveness: 0.01
            Radius: 6.65
        Target:
            Particles: {2212: 79, 2112: 118} #Gold197
            Saturation_Density: 0.16
            Radius: 6.65
            Diffusiveness: 0.01
        E_Kin: 1.23
        Fermi_Motion: "on"
        Impact:
            Max: 4.7
        Calculation_Frame: "center of mass"
Collision_Term:
    Pauli_Blocking:
        Spatial_Averaging_Radius: 1.86
        Momentum_Averaging_Radius: 0.08
        Gaussian_Cutoff: 2.2
Potentials:
    Skyrme:
        Skyrme_A: -124.0
        Skyrme_B: 71.0
        Skyrme_Tau: 2.00
```

7.3.6 GiBUU Au+Au 1.23A GeV 0-10 %

```
!***********************************************************************
! General Input
!***********************************************************************
&input
numEnsembles = 100  ! number of ensembles
eventtype    = 1     ! HeavyIon collision
numTimeSteps = 60   ! number of time steps
delta_T      = 0.5   ! time step size
num_runs_SameEnergy = 5
num_Energies = 1
path_To_Input = '/u/fseck/gibuu/buuinput'
checkGridSize_Flag = .true. ! check grid dimensions
length_real = 3000
length_perturbative = 0
printParticleVectorTime =  .true.
timeForOutput = 0.5
timeSequence  = 0.5
/
!***********************************************************************
! Heavy-Ion
!***********************************************************************
&projectile
projectile_Z=79, projectile_A=197 ! Au
/
&target
target_Z=79, target_A=197 ! Au
/
&heavyIon ! Eventype=1
impact_Parameter = 2.5
distance = 7.5
ekin_lab_Projectile = 1.23 ! kinetic Energy/nucleon of projectile
ekin_lab_Target = 0. ! kinetic Energy/nucleon of target
cmsFlag = .true.
adjustGridFlag = .true.
/
&HICanalysis_Input
flag_outputReal = .false.
flag_outputPert = .false.
flag_outputDetailed = .false.
pionAnalysis = .false.
/
!***********************************************************************
! Misc
!***********************************************************************
&initDensity
```

```
densitySwitch   = 1 ! 1 = dynamic, 2 = analytic
gridSize(1:3)   = 20., 20., 40. ! Size of density grid in x/y/z direction [fm]
gridPoints(1:3) = 40, 40, 80  ! Number of grid points in x/y/z direction
/
&initPauli
pauliSwitch = 1 ! 1=dynamic, 2=analytic
/
!**********************************************************************
! Potentials
!**********************************************************************
&Coulomb
CoulombFlag = .true.
/
&baryonPotential
symmetryPotFlag = 0
EQS_Type = 4 ! equation of state for nucleon resonances spin=1/2
DeltaPot = 3 ! potential of spin=3/2 resonances
HypPot=2
/
!**********************************************************************
! Collision term
!**********************************************************************
```

7.3.7 PHSD Au+Au 1.23A GeV 0-10 %

```
197,      MASSTA: target mass
79,       MSTAPR: protons in target
197,        MASSPR: projectile mass
79,        MSPRPR: protons in projectile
1.23,       ELAB:  (=4060000. Lab energy per nucleon LHC)
0.0,      BMIN:   minimal impact parameter in fm ! no effect for p+A
4.6,       BMAX:   maximal impact parameter in fm ! no effect for p+A
0.2,      DBIMP: impact parameter step in fm (used only if IBweight_MC=0)
150,       NUM:    optimized number of parallel ensambles ("events")
1,        ISUBS:  number of subsequent runs
12586,    ISEED:  ANY uneven INTEGER number
0,        IGLUE: =1 with partonic QGP phase (PHSD mode); =0 - HSD mode
106.,      FINALT: final time of calculation in fm/c
10,       ILOW: output level (default=10)
0,        Idilept: =0 no dileptons; =1 electron pair; =2  muon pair
0,        ICQ: =0 free rho's, =1 dropping mass, =2 broadening, =3
0,        IHARD: =1 with charm and bottom; =0 - without
0,     iCSDQPM ! =1 old; =2 Pierre x-section; =3 full
0,     iDQPM =0 old, =1 DQPM2014, =2 DQPM2015, =3 DQPM* for parton masses
0,        ievalmuB =0 Evaluation of T + muB=0 ; =1 Evaluation of T + muB
```

```
0,        IBweight_MC: =0 constant step in B =DBIMP; =1 choose B by Monte-Carlo
1,        IUSER: =1 for general users : use default /optimized settings;
```

Note: These are example files. The impact parameter was varied in the calculations in this thesis!

Bibliography

[1] A. Einstein. “Über die von der molekularkinetischen Theorie der Wärme geforderte Bewegung von in ruhenden Flüssigkeiten suspendierten Teilchen”. In: *Annalen der Physik* 322.8 (1905), pp. 549–560. DOI: 10.1002/andp.19053220806.

[2] J.J. Thomson. “On the Scattering of rapidly moving Electrified Particles.” In: *Camb. Lit. and Phil. Soc. xv.* pt. 5 (1910), pp. 459–465.

[3] J.J. Thomson. “Cathode rays”. In: *Phil. Mag. Ser. 5* 44 (1897), pp. 293–316. DOI: 10.1080/14786449708621070.

[4] E. Rutherford. “The scattering of alpha and beta particles by matter and the structure of the atom”. In: *Phil. Mag. Ser. 6* 21 (1911), pp. 669–688. DOI: 10.1080/14786440508637080.

[5] “Notes”. In: *Early Quantum Electrodynamics: A Sourcebook*. Cambridge University Press, 1994, pp. 101–110. DOI: 10.1017/CBO9780511608223.009.

[6] J. Chadwick. “The Existence of a Neutron”. In: *Proc. Roy. Soc. Lond. A* A136.830 (1932), pp. 692–708. DOI: 10.1098/rspa.1932.0112.

[7] Hideki Yukawa. “On the Interaction of Elementary Particles I”. In: *Proc. Phys. Math. Soc. Jap.* 17 (1935), pp. 48–57. DOI: 10.1143/PTPS.1.1.

[8] Murray Gell-Mann. “A Schematic Model of Baryons and Mesons”. In: *Phys. Lett.* 8 (1964), pp. 214–215. DOI: 10.1016/S0031-9163(64)92001-3.

[9] G. Zweig. “An SU(3) model for strong interaction symmetry and its breaking. Version 2”. In: *DEVELOPMENTS IN THE QUARK THEORY OF HADRONS. VOL. 1. 1964 - 1978*. Ed. by D.B. Lichtenberg and Simon Peter Rosen. Feb. 1964, pp. 22–101.

[10] D. Decamp et al. “Determination of the Number of Light Neutrino Species”. In: *Phys. Lett. B* 231 (1989), pp. 519–529. DOI: 10.1016/0370-2693(89)90704-1.

[11] Francis Halzen and Alan D. Martin. *Quarks and Leptons*. Wiley, 1984.

[12] Peter W. Higgs. “Broken Symmetries and the Masses of Gauge Bosons”. In: *Phys. Rev. Lett.* 13 (1964). Ed. by J.C. Taylor, pp. 508–509. DOI: 10.1103/PhysRevLett.13.508.

[13] Walter Greiner and Berndt Müller. *Gauge Theory of Weak Interactions*. Springer, Berlin, Heidelberg, 2009.

[14] Universität Zuerich Arbeitsgruppe Serra. *Standard Model*. http://www.physik.uzh.ch/groups/serra/images/SM1.png. abgerufen am 17.08.2018, 23:18.

[15] A. Gando et al. “Search for Majorana Neutrinos Near the Inverted Mass Hierarchy Region with KamLAND-Zen”. In: *Phys. Rev. Lett.* 117 (8 Aug. 2016), p. 082503. DOI: 10.1103/PhysRevLett.117.082503. URL: https://link.aps.org/doi/10.1103/PhysRevLett.117.082503.

[16] Y. Fukuda et al. “Evidence for oscillation of atmospheric neutrinos”. In: *Phys. Rev. Lett.* 81 (1998), pp. 1562–1567. DOI: 10.1103/PhysRevLett.81.1562. arXiv: hep-ex/9807003.

[17] Michael E. Peskin and Daniel V. Schroeder. *An Introduction to Quantum Field Theory*. The Advanced Book Program. PERSEUS BOOKS, 1995.

[18] Frank E. Close and Philip R. Page. https://www.spektrum.de/magazin/gluonenbaelle-gebilde-aus-reiner-kernkraft/825055. abgerufen am 16.09.2020, 12:19. 1999.

[19] Tom Lancaster and Stephen Blundell. *Quantum field theory for the gifted amateur*. Oxford, 2014. DOI: DOI:10.1093/acprof:oso/9780199699322.001.0001.

[20] David J. Gross and Frank Wilczek. "Ultraviolet Behavior of Nonabelian Gauge Theories". In: *Phys. Rev. Lett.* 30 (1973). Ed. by J.C. Taylor, pp. 1343–1346. DOI: 10.1103/PhysRevLett.30.1343.

[21] H.David Politzer. "Reliable Perturbative Results for Strong Interactions?" In: *Phys. Rev. Lett.* 30 (1973). Ed. by J.C. Taylor, pp. 1346–1349. DOI: 10.1103/PhysRevLett.30.1346.

[22] David J. Gross. "The discovery of asymptotic freedom and the emergence of QCD". In: *Proceedings of the National Academy of Sciences* 102.26 (2005), pp. 9099–9108. ISSN: 0027-8424. DOI: 10.1073/pnas.0503831102. eprint: https://www.pnas.org/content/102/26/9099.full.pdf. URL: https://www.pnas.org/content/102/26/9099.

[23] M. Tanabashi et al. "Review of Particle Physics". In: *Phys. Rev. D* 98 (3 Aug. 2018), p. 030001. DOI: 10.1103/PhysRevD.98.030001. URL: https://link.aps.org/doi/10.1103/PhysRevD.98.030001.

[24] Rajan Gupta. *Introduction to lattice QCD: Course*. July 1997. arXiv: hep-lat/9807028.

[25] Simon Resch. *Massenabhängigkeit des QCD-Phasendiagramms*. Aug. 2016.

[26] Shang-Keng Ma. *Modern theory of critical phenomena*. Vol. 46. Frontiers in physics. London [u.a.], 1976.

[27] Juergen Berges, Nikolaos Tetradis, and Christof Wetterich. "Nonperturbative renormalization flow in quantum field theory and statistical physics". In: *Phys. Rept.* 363 (2002), pp. 223–386. DOI: 10.1016/S0370-1573(01)00098-9. arXiv: hep-ph/0005122.

[28] Andreas Wipf. *The Functional Renormalization Group Method - An Introduction*. https://www.tpi.uni-jena.de/qfphysics/homepage/wipf/lectures/reviews/LaPlata_14.pdf. 2014.

[29] Joshua Ellis. "TikZ-Feynman: Feynman diagrams with TikZ". In: *Comput. Phys. Commun.* 210 (2017), pp. 103–123. DOI: 10.1016/j.cpc.2016.08.019. arXiv: 1601.05437 [hep-ph].

[30] Ralf Rapp. "Theory of Soft Electromagnetic Emission in Heavy-Ion Collisions". In: *Acta Phys. Polon. B* 42 (2011). Ed. by Michal Praszalowicz, pp. 2823–2852. DOI: 10.5506/APhysPolB.42.2823. arXiv: 1110.4345 [nucl-th].

[31] J. Goldstone. "Field Theories with Superconductor Solutions". In: *Nuovo Cim.* 19 (1961), pp. 154–164. DOI: 10.1007/BF02812722.

[32] Leon N. Cooper. "Bound Electron Pairs in a Degenerate Fermi Gas". In: *Phys. Rev.* 104 (4 Nov. 1956), pp. 1189–1190. DOI: 10.1103/PhysRev.104.1189. URL: https://link.aps.org/doi/10.1103/PhysRev.104.1189.

[33] Murray Gell-Mann, R.J. Oakes, and B. Renner. "Behavior of current divergences under SU(3) x SU(3)". In: *Phys. Rev.* 175 (1968), pp. 2195–2199. DOI: 10.1103/PhysRev.175.2195.

[34] R. Rapp, J. Wambach, and H. van Hees. "The Chiral Restoration Transition of QCD and Low Mass Dileptons". In: *Relativistic Heavy Ion Physics*. Ed. by R. Stock. Vol. 23. 2010, p. 134. DOI: 10.1007/978-3-642-01539-7_6. arXiv: 0901.3289 [hep-ph].

[35] S. Damjanovic. “Thermal dileptons at SPS energies”. In: *J. Phys. G* 35 (2008). Ed. by Jan-e Alam et al., p. 104036. DOI: 10.1088/0954-3899/35/10/104036. arXiv: 0805.4153 [nucl-ex].

[36] Steven Weinberg. “Precise relations between the spectra of vector and axial vector mesons”. In: *Phys. Rev. Lett.* 18 (1967), pp. 507–509. DOI: 10.1103/PhysRevLett.18.507.

[37] Volker Koch. “Aspects of chiral symmetry”. In: *Int. J. Mod. Phys. E* 6 (1997), pp. 203–250. DOI: 10.1142/S0218301397000147. arXiv: nucl-th/9706075.

[38] R. Rapp and J. Wambach. “Chiral symmetry restoration and dileptons in relativistic heavy ion collisions”. In: *Adv. Nucl. Phys.* 25 (2000), p. 1. DOI: 10.1007/0-306-47101-9_1. arXiv: hep-ph/9909229.

[39] G.E. Brown and Mannque Rho. “Matching the QCD and hadron sectors and medium dependent meson masses: Hadronization in relativistic heavy ion collisions”. In: *Phys. Rept.* 398 (2004), pp. 301–325. DOI: 10.1016/j.physrep.2004.05.006. arXiv: nucl-th/0206021.

[40] Guy Chanfray. *Medium modifications of hadrons in dense nuclear and hadronic matter*. https://www.ip2i.in2p3.fr/IMG/pdf/LectureQGP.pdf. abgerufen 04.09.2020, 10:15. 2007.

[41] M. Dey, V.L. Eletsky, and B.L. Ioffe. “Mixing of vector and axial mesons at finite temperature: an Indication towards chiral symmetry restoration”. In: *Phys. Lett. B* 252 (1990), pp. 620–624. DOI: 10.1016/0370-2693(90)90495-R.

[42] Kenji Fukushima and Chihiro Sasaki. “The phase diagram of nuclear and quark matter at high baryon density”. In: *Prog. Part. Nucl. Phys.* 72 (2013), pp. 99–154. DOI: 10.1016/j.ppnp.2013.05.003. arXiv: 1301.6377 [hep-ph].

[43] Matthias Hanauske et al. “Neutron Star Mergers: Probing the EoS of Hot, Dense Matter by Gravitational Waves”. In: *Particles* 2.1 (2019). Ed. by Armen Sedrakian, pp. 44–56. DOI: 10.3390/particles2010004.

[44] Veronica Dexheimer et al. “Neutron-Star-Merger Equation of State”. In: *Universe* 5.5 (2019), p. 129. DOI: 10.3390/universe5050129. arXiv: 1905.12658 [nucl-th].

[45] W. Dieterich. *Auszuege aus den Vorlesungen Theorie der Phasenuebergaenge*. http://theorie.physik.uni-konstanz.de/dieterich/skripte/Theorie-der-Phasenuebergaenge_Skript.pdf. 1995.

[46] *LATTICE QCD, THE NUMERICAL APPROACH TO THE STRONG FORCE*. https://webific.ific.uv.es/web/en/content/lattice-qcd-numerical-approach-strong-force. abgerufen 05.09.2020, 20:52.

[47] Roel Aaij et al. “Observation of $J/\psi p$ Resonances Consistent with Pentaquark States in $\Lambda_b^0 \to J/\psi K^- p$ Decays”. In: *Phys. Rev. Lett.* 115 (2015), p. 072001. DOI: 10.1103/PhysRevLett.115.072001. arXiv: 1507.03414 [hep-ex].

[48] Roel Aaij et al. “Observation of $J/\psi\phi$ structures consistent with exotic states from amplitude analysis of $B^+ \to J/\psi\phi K^+$ decays”. In: *Phys. Rev. Lett.* 118.2 (2017), p. 022003. DOI: 10.1103/PhysRevLett.118.022003. arXiv: 1606.07895 [hep-ex].

[49] George Gamow. “Mass defect curve and nuclear constitution”. In: *Proc. R. Soc. Lond. A* 126 (1930), pp. 632–644. DOI: http://doi.org/10.1098/rspa.1930.0032.

[50] Henning Heiselberg and Morten Hjorth-Jensen. “Phases of dense matter in neutron stars”. In: *Phys. Rept.* 328 (2000), pp. 237–327. DOI: 10.1016/S0370-1573(99)00110-6. arXiv: nucl-th/9902033.

[51] Ulrich W. Heinz and Maurice Jacob. “Evidence for a new state of matter: An Assessment of the results from the CERN lead beam program”. In: (Jan. 2000). arXiv: nucl-th/0002042.

[52] Bjoern Schenke. *The smallest fluid on earth*. http://shovkovy.faculty.asu.edu/colloquium/slides/Colloquium_Slides_Schenke.pdf. Physical Colloqium of Gießen University. Feb. 2020.

[53] MADAI.us. *Model and Data Analysis Initiative*. accessed September 18, 2015. 2015.

[54] Florian Seck. *Development of a Realistic Event Generator for In-Medium and QGP Dileptons*. Oct. 2015.

[55] Christine Nattrass. *Measuring the energy density of the QGP*. http://nattrass.utk.edu/Talks/3KKJanuary2016/Nattrass3KK2016.pdf. 2016.

[56] Ulrich W. Heinz and Kang Seog Lee. “The rho peak in the dimuon spectrum as a clock for fireball lifetimes in relativistic nuclear collisions”. In: *Phys. Lett. B* 259 (1991), pp. 162–168. DOI: 10.1016/0370-2693(91)90152-G.

[57] Larry D. McLerran and T. Toimela. “Photon and Dilepton Emission from the Quark - Gluon Plasma: Some General Considerations”. In: *Phys. Rev. D* 31 (1985), p. 545. DOI: 10.1103/PhysRevD.31.545.

[58] Paul M. Hohler and Ralf Rapp. “Is ρ-Meson Melting Compatible with Chiral Restoration?” In: *Phys. Lett. B* 731 (2014), pp. 103–109. DOI: 10.1016/j.physletb.2014.02.021. arXiv: 1311.2921 [hep-ph].

[59] J. Adamczewski-Musch et al. “Probing dense baryon-rich matter with virtual photons”. In: *Nature Phys.* 15.10 (2019), pp. 1040–1045. DOI: 10.1038/s41567-019-0583-8.

[60] The HADES Collaboration. *Proposal for experiments at SIS18 during FAIR Phase-0*. 2017.

[61] Hendrik van Hees. *Introduction to Relativistic Transport Theory*. https://itp.uni-frankfurt.de/ hees/publ/kolkat Lecture notes on Transport theory for CNT Lectures on Hot/Dense Matter 2015 at Variable Energy Cyclogron Center, Kolkata, India. 2020.

[62] Bjoern Schenke, Sangyong Jeon, and Charles Gale. “(3+1)D hydrodynamic simulation of relativistic heavy-ion collisions”. In: *Phys. Rev. C* 82 (2010), p. 014903. DOI: 10.1103/PhysRevC.82.014903. arXiv: 1004.1408 [hep-ph].

[63] Bjoern Schenke, Chun Shen, and Prithwish Tribedy. “Running the gamut of high energy nuclear collisions”. In: (May 2020). arXiv: 2005.14682 [nucl-th].

[64] Barbara Drossel. *Statistische Physik*. Lecture notes of theoretical Physics IV at TU Darmstadt, winter term 2017/18. 2017.

[65] J. Weil et al. “Particle production and equilibrium properties within a new hadron transport approach for heavy-ion collisions”. In: *Phys. Rev. C* 94.5 (2016), p. 054905. DOI: 10.1103/PhysRevC.94.054905. arXiv: 1606.06642 [nucl-th].

[66] Elena Bratkovskaya. *Introduction to the dynamical models of heavy-ion collisions*. Lecture notes for The CRC-TR211 Lecture Week *Lattice QCD and Dynamical models for Heavy Ion Physics* Limburg, Germany, 10-13 December, 2019. Dec. 2019.

[67] O. Buss et al. “Transport-theoretical Description of Nuclear Reactions”. In: *Phys. Rept.* 512 (2012), pp. 1–124. DOI: 10.1016/j.physrep.2011.12.001. arXiv: 1106.1344 [hep-ph].

[68] Andreas Lang et al. “A new treatment of Boltzmann-like collision integrals in nuclear kinetic equations”. In: *Journal of Computational Physics* 106.2 (1993), pp. 391–396. ISSN: 0021-9991. DOI: https://doi.org/10.1016/S0021-9991(83)71116-2. URL: http://www.sciencedirect.com/science/article/pii/S0021999183711162.

[69] T. Skyrme. “The effective nuclear potential”. In: *Nucl. Phys.* 9 (1959), pp. 615–634. DOI: 10.1016/0029-5582(58)90345-6.

[70] Paula Hillmann, Jan Steinheimer, and Marcus Bleicher. “Directed, elliptic and triangular flow of protons in Au+Au reactions at 1.23 A GeV: A theoretical analysis of the recent HADES data”. In: (2018). DOI: 10.1088/1361-6471/aac96f. arXiv: 1802.01951v2 [nucl-th].

[71] Stefan Teis. “Transporttheoretische Beschreibung von relativistischen Schwerionenkollisionen bei SIS-Energien”. PhD thesis. Giessen U., 1996.

[72] Christian Fuchs. “Kaon production in heavy ion reactions at intermediate energies”. In: *Prog. Part. Nucl. Phys.* 56 (2006), pp. 1–103. DOI: 10.1016/j.ppnp.2005.07.004. arXiv: nucl-th/0507017.

[73] Behruz Kardan. “Collective flow and correlations measurements with HADES in Au+Au collisions at 1.23 AGeV”. In: *Nucl. Phys. A* 982 (2019). Ed. by Federico Antinori et al., pp. 431–434. DOI: 10.1016/j.nuclphysa.2018.09.061. arXiv: 1809.07821 [nucl-ex].

[74] J. Adamczewski-Musch et al. “Directed, elliptic and higher order flow harmonics of protons, deuterons and tritons in Au+Au collisions at $\sqrt{s_{NN}} = 2.4$ GeV”. In: (May 2020). arXiv: 2005.12217 [nucl-ex].

[75] J. Adamczewski-Musch et al. “Sub-threshold production of K^0_s mesons and Λ hyperons in Au+Au collisions at $\sqrt{s_{NN}} = 2.4$ GeV”. In: *Phys. Lett. B* 793 (2019), pp. 457–463. DOI: 10.1016/j.physletb.2019.03.065. arXiv: 1812.07304 [nucl-ex].

[76] Wilfried Kuhn and Gerhard Rudolf. *Lehrbuch der Physik IIIC: Felder und Ladungen*. Georg Westermann Verlag, 1974.

[77] S.A. Bass et al. “Microscopic models for ultrarelativistic heavy ion collisions”. In: *Prog. Part. Nucl. Phys.* 41 (1998), pp. 255–369. DOI: 10.1016/S0146-6410(98)00058-1. arXiv: nucl-th/9803035.

[78] Stephan Endres. *Dilepton Production with UrQMD*. http://theory.gsi.de/~ebratkov/Conferences/NeD-TURIC-2012/talks/29/Endres.pdf. talk at NeD/TURIC - June 29th, 2012, abgerufen 09.10.2020, 20:00. 2012.

[79] M. Bleicher et al. “Relativistic hadron hadron collisions in the ultrarelativistic quantum molecular dynamics model”. In: *J. Phys. G* 25 (1999), pp. 1859–1896. DOI: 10.1088/0954-3899/25/9/308. arXiv: hep-ph/9909407.

[80] Janus Weil and Ulrich Mosel. “Dilepton production at SIS energies with the GiBUU transport model”. In: *J. Phys. Conf. Ser.* 426 (2013). Ed. by Almudena Arcones et al., p. 012035. DOI: 10.1088/1742-6596/426/1/012035. arXiv: 1211.3761 [nucl-th].

[81] Torbjorn Sjostrand, Stephen Mrenna, and Peter Z. Skands. “PYTHIA 6.4 Physics and Manual”. In: *JHEP* 05 (2006), p. 026. DOI: 10.1088/1126-6708/2006/05/026. arXiv: hep-ph/0603175.

[82] W. Cassing and E.L. Bratkovskaya. “Parton transport and hadronization from the dynamical quasiparticle point of view”. In: *Phys. Rev. C* 78 (2008), p. 034919. DOI: 10.1103/PhysRevC.78.034919. arXiv: 0808.0022 [hep-ph].

[83] W. Cassing and E.L. Bratkovskaya. “Parton-Hadron-String Dynamics: an off-shell transport approach for relativistic energies”. In: *Nucl. Phys. A* 831 (2009), pp. 215–242. DOI: 10.1016/j.nuclphysa.2009.09.007. arXiv: 0907.5331 [nucl-th].

[84] Jan Staudenmaier et al. “Dilepton production and resonance properties within a new hadronic transport approach in the context of the GSI-HADES experimental data”. In: *Phys. Rev. C* 98.5 (2018), p. 054908. DOI: 10.1103/PhysRevC.98.054908. arXiv: 1711.10297 [nucl-th].

[85] E.L. Bratkovskaya et al. “System size and energy dependence of dilepton production in heavy-ion collisions at 1-2 GeV/nucleon energies”. In: *Phys. Rev. C* 87 (2013), p. 064907. DOI: 10.1103/PhysRevC.87.064907. arXiv: 1301.0786 [nucl-th].

[86] Janus Weil and Ulrich Mosel. “The GiBUU transport model”. In: *EPJ Web Conf.* 52 (2013). Ed. by U. Gensch and M. Walter, p. 06007. DOI: 10.1051/epjconf/20125206007.

[87] Stephan Endres and Marcus Bleicher. “Dilepton production at SIS energies with the UrQMD model”. In: *J. Phys. Conf. Ser.* 426 (2013). Ed. by Almudena Arcones et al., p. 012033. DOI: 10.1088/1742-6596/426/1/012033.

[88] Heidi Schuldes. “Charged Kaon and ϕ-reconstruction in Au+Au Collisions at 1.23 AGeV”. PhD thesis. Goethe-Universitaet Frankfurt a. M., 2016.

[89] J. Adamczewski-Musch et al. “Charged pion production in $\mathbf{Au} + \mathbf{Au}$ collisions at $\sqrt{\mathbf{s_{NN}}} = 2.4\mathbf{GeV}$”. In: (May 2020). arXiv: 2005.08774 [nucl-ex].

[90] P. Huovinen et al. “Dileptons and photons from coarse grained microscopic dynamics and hydrodynamics compared to experimental data”. In: *Phys. Rev. C* 66 (2002), p. 014903. DOI: 10.1103/PhysRevC.66.014903. arXiv: nucl-th/0203023.

[91] Stephan Endres et al. “Coarse-graining approach for dilepton production at energies available at the CERN Super Proton Synchrotron”. In: *Phys. Rev. C* 91.5 (2015), p. 054911. DOI: 10.1103/PhysRevC.91.054911. arXiv: 1412.1965 [nucl-th].

[92] Rene Brun and Fons Rademakers. “ROOT - An Object Oriented Data Analysis Framework”. In: *Proceedings AIHENP’96 Workshop*. Lausanne, 1996.

[93] Dmytro Oliinychenko and Hannah Petersen. “Deviations of the Energy-Momentum Tensor from Equilibrium in the Initial State for Hydrodynamics from Transport Approaches”. In: *Phys. Rev. C* 93.3 (2016), p. 034905. DOI: 10.1103/PhysRevC.93.034905. arXiv: 1508.04378 [nucl-th].

[94] Tetyana Galatyuk et al. “Thermal Dileptons from Coarse-Grained Transport as Fireball Probes at SIS Energies”. In: *Eur. Phys. J. A* 52.5 (2016), p. 131. DOI: 10.1140/epja/i2016-16131-1. arXiv: 1512.08688 [nucl-th].

[95] W. Florkowski and R. Ryblewski. “Dynamics of anisotropic plasma at the early stages of relativistic heavy-ion collisions”. In: *Acta Phys. Polon. B* 40 (2009), pp. 2843–2863. arXiv: 0901.4653 [nucl-th].

[96] Radoslaw Ryblewski and Wojciech Florkowski. “Highly-anisotropic and strongly-dissipative hydrodynamics with transverse expansion”. In: *Eur. Phys. J. C* 71 (2011), p. 1761. DOI: 10.1140/epjc/s10052-011-1761-8. arXiv: 1103.1260 [nucl-th].

[97] Maximilian Wiest. *Project Proposal - Dileptons as probes of strongly interacting matter*. Project Proposal zum Modul *Praktikum zur Einführung in das Wissenschaftliche Arbeiten*. 2020.

[98] K.J. Eskola, K. Kajantie, and J. Lindfors. “Quark and Gluon Production in High-Energy Nucleus-Nucleus Collisions”. In: *Nucl. Phys. B* 323 (1989), pp. 37–52. DOI: 10.1016/0550-3213(89)90586-5.

[99] Dariusz Miskowiec and Jens Elgeti. *Nuclear Overlap Calculation*. http://web-docs.gsi.de/~misko/overlap/. 2001.

[100] A. Bialas, M. Bleszynski, and W. Czyz. "Multiplicity Distributions in Nucleus-Nucleus Collisions at High-Energies". In: *Nucl. Phys. B* 111 (1976), pp. 461–476. DOI: 10.1016/0550-3213(76)90329-1.

[101] J. Adamczewski-Musch et al. "Properties of thermal electromagnetic radiation from QCD matter at high μ_B". In: (2020).

[102] Ralf Rapp and Hendrik van Hees. "Thermal Dileptons as Fireball Thermometer and Chronometer". In: *Phys. Lett. B* 753 (2016), pp. 586–590. DOI: 10.1016/j.physletb.2015.12.065. arXiv: 1411.4612 [hep-ph].

[103] George Neville Watson. *A Treatise on the Theory of Bessel Functions*. 2nd ed. Cambridge University Press, 1922.

List of Figures

List of Tables

Acknowledgements

First and foremost I want to thank Prof. Tetyana Galatyuk for her full support in writing this thesis in her group. Her energy is inspiring and her considerable experience and knowledge helped me sort out a wide range of problems. I want to thank Florian Seck for providing his coarse graining Macros to me, for clarifications and his patience when bugs made my work take longer. I want to thank the whole ViP-QM group, Dr. Szymon Harabasz, Dr. Adrian Rost, Dominique Dittert, Wilhelm Krueger, Vadym Kedych, Frederic Kornas, Niklas Schild and Patrick Lehnung for enlightening and funny discussions. The next ECAL session is coming.
I want to emphasize my thanks to Prof. Joachim Stroth for interesting discussions on nuclear potentials among many other subjects and valuable insights on experimental data analysis. My thanks include everyone in his group and the group of Prof. Christoph Blume. I want to acknowledge the help of the whole HADES collaboration, especially Dr. Malgorzata Gumberidze for providing the data on the HADES pion yields, Dr. Jochen Markert for helping out with computer problems and reminding me of lunchtime everyday and Erwin Schwab for interesting discussions on astronomy.
Furthermore, I want to thank Dr. Pierre Moreau and Prof. Elena Bratkovskaya for providing me with information and help with the PHSD model. Especially Pierre's patch of the PHSD code for coarse graining has been extraordinarily helpful and should under no circumstances stay unaccounted for.
I want to thank Dr. Jan Steinheimer-Froschauer and Prof. Hannah Elfner for clarifying aspects of their respective models, UrQMD and SMASH.
I want to thank Tim Gehrunger for an educated outsiders view on physical matters, even though I was not able to give this back as much in his field of algebraic geometry.
I want to thank my mother Gaby Wiest and my girlfriend Laura Quellmalz for their ongoing support and patience.